

---

# Advanced characterization and control of laser wakefield acceleration

Alexander Buck

---



München 2011



---

# **Advanced characterization and control of laser wakefield acceleration**

**Alexander Buck**

---

Dissertation  
an der Fakultät für Physik  
der Ludwig–Maximilians–Universität  
München

vorgelegt von  
Alexander Buck  
aus Stuttgart

München, den 22. Juli 2011

Erstgutachter: Prof. Dr. Ferenc Krausz

Zweitgutachter: Prof. Dr. Toshiki Tajima

Tag der mündlichen Prüfung: 12. September 2011

# Contents

<b>Contents</b>	<b>v</b>
<b>List of Figures</b>	<b>ix</b>
<b>List of Tables</b>	<b>xi</b>
<b>Abstract</b>	<b>xiii</b>
<b>Introduction</b>	<b>1</b>
List of publications by the author incorporated in this thesis . . . . .	5
<b>1 Theoretical foundations of high-intensity laser-plasma interaction</b>	<b>7</b>
1.1 Attributes of light . . . . .	7
1.2 Laser pulse interaction with single electrons . . . . .	9
1.3 Laser pulse interaction with single atoms and ionization mechanisms . . . . .	11
1.4 Non-relativistic, cold, collisionless plasmas . . . . .	13
1.5 Laser propagation in underdense plasmas . . . . .	14
1.6 Excitation of large-amplitude Langmuir waves . . . . .	20
1.7 Maximum attainable field and longitudinal wave breaking . . . . .	24
1.8 Limiting factors for the acceleration of electrons . . . . .	28
1.9 Optimum acceleration conditions and scaling laws . . . . .	31
1.10 Injection of electrons into wakefields . . . . .	33
1.10.1 Self-injection via transverse wave breaking . . . . .	34
1.10.2 Injection at plasma density transitions . . . . .	36
1.10.3 Colliding pulse injection . . . . .	37
1.10.4 Ionization injection . . . . .	38
1.11 Particle-in-cell simulations (PIC) . . . . .	39

<b>2</b>	<b>Basic experimental setup</b>	<b>43</b>
2.1	Laser systems . . . . .	43
2.1.1	Light Wave Synthesizer 20 (LWS-20) . . . . .	43
2.1.2	Advanced Titanium-Sapphire Laser (ATLAS) . . . . .	48
2.2	Gas targets . . . . .	48
2.2.1	Subsonic and supersonic nozzles . . . . .	48
2.2.2	Gas flow characterization . . . . .	49
2.2.3	Shocks in supersonic flows . . . . .	51
2.3	Electron detection . . . . .	53
2.3.1	Energy-independent charge measurements . . . . .	53
2.3.2	Electron energy spectrometer . . . . .	55
2.3.3	Absolute charge calibration of scintillating screens . . . . .	57
2.3.4	Pointing monitor . . . . .	63
2.3.5	Advanced diagnostics . . . . .	63
<b>3</b>	<b>Controlled injection of electrons into wakefields</b>	<b>65</b>
3.1	LWFA with LWS-20 in the self-injection regime . . . . .	65
3.2	Controlled injection at sharp density transitions with LWS-20 . . . . .	69
3.2.1	Stable electron runs with tunable energy . . . . .	69
3.2.2	Measuring the longitudinal field and dephasing effects . . . . .	73
3.2.3	Observation of beamloading . . . . .	74
3.2.4	Scaling with the background electron density . . . . .	76
3.3	Controlled injection with ATLAS . . . . .	77
3.3.1	Stable injection . . . . .	77
3.3.2	Tunability over a wide range . . . . .	80
<b>4</b>	<b>Real-time observation of laser-driven electron acceleration</b>	<b>83</b>
4.1	Motivation . . . . .	83
4.2	Experimental setup and simulation results . . . . .	85
4.2.1	Basic setup . . . . .	85
4.2.2	Simulation of the signal via ray-tracing . . . . .	85
4.3	Electron bunch measurements via Faraday rotation . . . . .	89
4.4	Plasma wave measurements via shadowgraphy . . . . .	92
4.5	Snapshots of LWFA via the combination of polarimetry and shadowgraphy . . . . .	95
<b>5</b>	<b>Conclusions</b>	<b>99</b>
<b>6</b>	<b>Outlook</b>	<b>103</b>

<b>A Cross-Polarized Wave Generation (XPW)</b>	<b>107</b>
<b>Bibliography</b>	<b>113</b>
<b>Publications by the Author</b>	<b>129</b>
<b>Data archiving</b>	<b>131</b>
<b>Curriculum Vitae</b>	<b>139</b>
<b>Acknowledgements</b>	<b>143</b>





# List of Figures

1.1	Comparison of different ionization mechanisms . . . . .	12
1.2	Refraction of a probe beam at the plasma . . . . .	17
1.3	Snell's law . . . . .	17
1.4	Nonlinear, one-dimensional wakefield . . . . .	23
1.5	Optimum wakefield driving conditions . . . . .	25
1.6	Longitudinal phase-space in the one-dimensional model . . . . .	27
1.7	Comparison of dephasing and depletion length . . . . .	29
1.8	Illustration of the beamloading effect . . . . .	31
1.9	Transverse wave breaking in the "bubble" regime . . . . .	35
1.10	Injection of electrons at a sharp density transition. . . . .	38
1.11	Particle-in-cell simulation . . . . .	41
2.1	Basic experimental setup for LWFA experiments . . . . .	44
2.2	Layout of Light Wave Synthesizer 20 . . . . .	45
2.3	Output parameters of LWS-20 . . . . .	46
2.4	Layout of the ATLAS laser system . . . . .	47
2.5	Gas jet interferometry . . . . .	49
2.6	Gaussian and trapezoidal fit functions . . . . .	50
2.7	Comparison of fitting routine and Abel inversion . . . . .	52
2.8	Generation of a shockfront in a supersonic flow . . . . .	54
2.9	Electron energy spectrometer . . . . .	56
2.10	Setup for the calibration of the scintillating screens . . . . .	58
2.11	Emission spectrum, quantum efficiency, and modulation transfer function . . . . .	59
2.12	Absolute calibration of scintillating screens . . . . .	61
2.13	Saturation of scintillating screens . . . . .	62
3.1	High energy series of self-injected electrons with LWS-20 . . . . .	66
3.2	Stable series of self-injected electrons with LWS-20 . . . . .	67
3.3	Two stable electron series injected at the density transition with LWS-20 . . . . .	70

3.4	Comparison of self-injection and density transition injection with LWS-20	72
3.5	Accelerating field and dephasing of the electron bunch . . . . .	75
3.6	Observation of beamloading . . . . .	76
3.7	Scaling of the electron energy with the electron density . . . . .	78
3.8	Comparison of self-injection and density transition injection with ATLAS	79
3.9	Tunability of LWFA with ATLAS and density transition injection . . . . .	80
3.10	Energy dependence of beam parameters and accelerating field . . . . .	82
4.1	Illustration of laser wakefield acceleration . . . . .	84
4.2	Setup for Faraday rotation and shadowgraphy experiments. . . . .	86
4.3	Simulation of the polarimetry and shadowgraphy signal. . . . .	88
4.4	Raw images and evaluated polarization rotation angle . . . . .	90
4.5	Scaled polarization rotation angle vs. charge . . . . .	92
4.6	Plasma wave observation via shadowgraphy. . . . .	93
4.7	Shadowgram of the shockfront . . . . .	94
4.8	Snapshots of the trapped electrons and the plasma wave. . . . .	96
4.9	Evolution of the electron bunch duration and the plasma wave during the acceleration process. . . . .	97
6.1	Overview over the main beam parameters of all stable runs with ATLAS .	104
6.2	Evolution of the electron bunch parameters during the acceleration process with controlled injection. . . . .	106
A.1	Cross-polarized wave generation setup . . . . .	109
A.2	Contrast enhancement of LWS-20 with XPW . . . . .	110
A.3	Spectral broadening by cross-polarized wave generation . . . . .	112

# List of Tables

- 1.1 Ionization potential and intensity threshold for barrier-suppression ionization of relevant elements . . . . . 13
- 2.1 Absolute calibration of scintillating screens and onset of saturation . . . . . 59
- 3.1 Parameters of the two electron runs with controlled injection and LWS-20 69
- 3.2 Parameters of the selected shots of two electron runs with self-injection and controlled injection with LWS-20 . . . . . 71
- 3.3 Parameters of the two electron runs with self-injection and controlled injection at the density transition with ATLAS . . . . . 78
- 3.4 Parameters of the six electron runs with controlled injection and ATLAS to show the tunability . . . . . 81



# Zusammenfassung

Diese Doktorarbeit befasst sich mit der Beschleunigung von Elektronen auf relativistische Energien mithilfe von ultrakurzen Hochintensitätslaserpuls. Bei der sogenannten *Laser Wakefield Acceleration* (LWFA) werden Elektronen durch die Plasmawelle beschleunigt, die dem Laserpuls bei seiner Propagation durch das von ihm ionisierte Gas folgt. Dabei wird ein Beschleunigungsfeld um 100 GV/m erzeugt, das somit drei bis vier Größenordnungen stärker als das Feld in derzeitigen Radiofrequenzbeschleunigern ist. Auf Laserplasmen basierende Elektronenbeschleuniger könnten daher durch ihre reduzierte Größe und dadurch verringerte Kosten im Vergleich zu existierenden Anlagen die Möglichkeit bieten, viele relativ kleine Labore und Kliniken mit derartigen kompakten Beschleunigern für Anwendungen mit diesen Teilchenstrahlen auszustatten. Darüber hinaus haben die mit diesem Ansatz beschleunigten Teilchen zwei Vorteile, nämlich zum einen die intrinsisch kurze Pulsdauer von wenigen Femtosekunden, und zum anderen die automatische Synchronisation mit dem Laserpuls. Die so erzeugten Elektronenpulse sind daher hervorragend für zeitaufgelöste Pump-Probe-Experimente oder die Erzeugung von Röntgenstrahlung, z.B. mithilfe von Undulatoren oder Thomson-Rückstreuung, geeignet. Bis es jedoch soweit ist und diese Beschleuniger routinemäßig eingesetzt werden können, müssen noch diverse Parameter signifikant verbessert werden, so z.B. die Reproduzierbarkeit, Stabilität und Abstimmbarkeit.

Für die Instabilitäten der beschleunigten Teilchen war bis jetzt vor allem die Injektion der Elektronen in die Plasmawelle verantwortlich. Der erste Teil dieser Doktorarbeit beschreibt die erste erfolgreiche Demonstration dieser Injektion nach einem neuen Prinzip, nämlich die Injektion an einem Dichtesprung im Plasma, der in einem Überschallfluß erzeugt wird. Es wird in Experimenten mit zwei verschiedenen Lasersystemen mit unterschiedlichen Pulsdauern und -energien gezeigt, daß die Eigenschaften der erzeugten Elektronenstrahlen mithilfe dieser Methode wesentlich verbessert wurden. So wurden mit dem Light Wave Synthesizer 20 (8 fs) stabile Elektronen zwischen 20 und 30 MeV erzeugt, mit denen wichtige Aspekte wie Dephasing oder Beamloading untersucht werden konnten. Mit ATLAS (26 fs) wurde eine stark verbesserte Kontrolle über die Elektronenenergie, die im Bereich 15-150 MeV eingestellt werden konnte, gezeigt. Durch die Verbesserungen der Strahleigenschaften sind nun erste Thomson-Rückstreuungsexperimente in Reichweite. Die Beschleunigung auf noch höhere Elektronenenergien (> 150-200 MeV) wird für Experimente mit leicht modifiziertem Aufbau erwartet.

Der zweite Teil der Arbeit dreht sich um die detaillierte Charakterisierung des Beschleunigungsprozesses. Bis vor kurzem war der experimentelle Zugang zu den relevanten dynamischen Vorgängen im Plasma stark limitiert, so daß die Charakterisierungsmethoden sich fast ausschließlich auf den erzeugten Elektronenpuls beschränkten. Wir haben eine Methode entwickelt, um sowohl den Elektronenpuls als auch die ihn beschleunigende Plasmawelle gleichzeitig mithilfe von zwei Techniken, nämlich Polarimetry und Shadowgraphy, bereits im Plasma während der Beschleunigung sichtbar zu machen. Aufgrund der einzigartig kurzen Pulsdauer des Light Wave Synthesizer 20 war es uns möglich, Schnappschüsse des Beschleunigungsprozesses aufzunehmen um die relevanten Vorgänge auf den fs-Zeit- und  $\mu\text{m}$ -Längenskalen zu untersuchen. Unter anderem konnte dabei die Elektronenpulsdauer von  $5.8_{-2.1}^{+1.9}$  fs gemessen werden; eine Größe, die bisher nur über indirekte Messungen zugänglich war. Die verbesserte Untersuchungsmöglichkeit der Vorgänge mit unserer Methode ermöglicht es daher, Experiment und Theorie bzw. Simulation besser zu vergleichen, aktuelle Messergebnisse zu verstehen und im Besonderen die Entwicklung zukünftiger Beschleuniger auf der Basis von Laserplasmen voranzutreiben.

# Abstract

This thesis deals with the acceleration of electrons to relativistic energies by ultra-short, high intensity laser pulses. In the so-called *Laser Wakefield Acceleration* (LWFA) scheme, electrons are accelerated in a plasma wave trailing the laser pulse during the propagation through an ionized gas. The associated accelerating field is on the order of 100 GV/m and thus three to four orders of magnitude higher compared to state-of-the-art, radio-frequency accelerators. Thus, laser-plasma-based acceleration offers the great potential to build accelerators that are much smaller than existing large-scale accelerator facilities. In addition, these accelerators are also potentially much cheaper, opening up the possibility to provide many smaller laboratories or hospitals with compact particle sources for applications. Further advantages of the new accelerators compared to their traditional counterparts are the intrinsic few-fs electron bunch duration and the synchronization to a short laser pulse. Thus, they are an ideal tool for time-resolved pump-probe experiments or the generation of x-rays, e.g. via undulator radiation or Thomson backscattering of a near-infrared laser pulse. However, despite their great potential, laser-driven electron accelerators still lag behind radio-frequency accelerators in several important aspects such as reproducibility, stability, and tunability. These issues have to be faced before the accelerators are ready for stable operation and before they can be regarded as a reliable source of high quality, monoenergetic electron bunches.

To date, the injection and trapping of electrons in the plasma wave has been a major source for instabilities in the accelerator output. The first part of this thesis is the first successful demonstration of a new scheme of injecting electrons into the plasma wave at a sharp, downward density transition, which originates from a shockfront in a supersonic gas flow. It is shown that with this controlled injection method the accelerator output is stabilized significantly and the beam properties such as the electron energy spread are improved. The scheme is verified with two different laser systems. Stable generation of 20-30 MeV electron bunches is demonstrated with Light Wave Synthesizer 20 (8 fs) enabling the study of important aspects of LWFA such as dephasing or beamloading. For ATLAS (26 fs), tunability over a wide range (15-150 MeV) is shown. Due to the major improvement in beam quality and stability, electron acceleration via trapping at the density transition is suitable for first Thomson backscattering experiments. Electron energies exceeding 150-200 MeV are likely to be produced in the same scheme with a slightly modified setup.

The second part of this thesis covers the in-depth characterization of the acceleration process. Until recently, experimental access into the relevant dynamics inside of the plasma was very limited and most characterization techniques measured only properties of the final output electron beam. We have developed a method to visualize both the electron bunch and the accelerating plasma wave simultaneously via the combination of two techniques, namely polarimetry and shadowgraphy. Due to the unique few-cycle laser pulse duration of Light Wave Synthesizer 20, snapshots of the acceleration process can be taken to study the dynamics happening on a few-fs temporal and a few- $\mu\text{m}$  spatial scale. Additionally, the ultra-short electron bunch duration of  $5.8^{+1.9}_{-2.1}$  fs is measured with the same technique, confirming the values that have been obtained via indirect measurements before. The new insights into the acceleration process enable a thorough investigation and particularly a better comparison between experiments and theoretical or computational predictions. Thus, this real-time observation is expected to be a major diagnostic tool for the study of current LWFA experiments and will strongly support the design of future laser-plasma accelerators.

# Introduction

## Motivation

Particle accelerators have become an integral part of today's basic science. Since the development of the Cockroft-Walton generator in the 1930s [1] that accelerated ions to energies of several MeV, charged particle accelerators have seen a constant improvement and now reach the GeV or even TeV energy range. The recently commissioned Large Hadron Collider (LHC) [2] near Geneva, Switzerland will be able to collide protons with a center-of-mass energy of 14 TeV once it is completely finished. However, as particle accelerators have been able to deliver higher and higher particle energies, also their size has grown accordingly. This is due to material breakdown [3] which limits the accelerating electric fields that can be sustained without damage in state-of-the-art, radio-frequency (rf) accelerators to  $E_{\max} = 10 - 100$  MV/m. Thus, an acceleration length in the km range is necessary to reach these particle energies.

To reduce costs, the accelerated charged particles are often forced onto a circular path by superconducting coils, passing many times through each acceleration stage. However, the transverse acceleration of the circular path leads to the emission of synchrotron radiation and thus an energy loss per turn of  $E_{\text{loss}} \propto \frac{E^4}{m^4 R}$ , where  $E$  and  $m$  are particle energy and mass, and  $R$  the radius of the accelerator. For the LHC, this loss is on the order of a few keV per proton and thus about a factor of 100 smaller than the energy gain per roundtrip due to its large circumference of 27 km. The LHC is currently the biggest ion acceleration machine worldwide and the total costs of the project are estimated to be several billion Euros, which is shared by many countries in an international consortium. In 1993, a similar project in the US, the Superconducting Super Collider (SSC), was cancelled due to the exploding costs. They had already spent two billion dollars and the final costs were estimated to be around nine billion dollars [4, 5].

Using electrons instead of protons offers the advantage of greatly simplifying the collision analysis because of the absence of any complicated substructure. However, the radiation loss in circular electron accelerators is many orders of magnitude greater due to

the lower particle mass. Thus, plans are currently made for the next electron accelerator in a linear geometry, which in turn increases the costs per particle energy. The International Linear Collider (ILC) is planned to have a total acceleration length of around 30 km and to collide electrons and positrons with a center-of-mass energy of 500 GeV. Here, the total costs are estimated to be between 10 and 20 billion dollars [6] and the ILC might well be the largest accelerator ever built with the current technology due to the high costs (if constructed at all).

While the driving force for the construction of large scale accelerators is the desire to test particle physics theory, e.g. the search for the Higgs boson at the LHC [7], also other important applications with high energy charged particles have been developed. Synchrotrons are electron accelerators that are deliberately built in a ring geometry to use the broadband x-ray emission by synchrotron radiation for further studies. Coherent x-ray radiation with a narrow bandwidth is generated in Free Electron Lasers (FEL) [8]. Other applications include cancer therapy by irradiation with protons and carbon ions instead of conventional x-ray therapy [9] or electron diffraction for basic and materials research.

Today, alternatives to the current accelerator technology are required out of two main reasons. Firstly, the largest accelerators have reached size and cost requirements that are so huge that it is unlikely that an even bigger machine will be built. Secondly, due to the other possible applications such as x-ray generation or proton therapy, many laboratories and hospitals could benefit from having their own smaller-scale particle accelerator.

## **Plasma-based acceleration**

It has already been recognized early on that plasma waves, i.e., the excitation of propagating charge density fluctuations in ionized gases, can sustain large amplitude electrostatic fields [10]. Only about 30 years ago, the potential for the acceleration of electrons to relativistic energies was recognized by Tajima and Dawson [11]. Generally, electric fields with  $E_{\max} \approx 100$  GV/m can be present in plasma waves, which is up to three or four orders of magnitude larger than in conventional rf accelerators.

In the so-called *Plasma Wakefield Accelerator* (PWFA), the plasma waves are driven by one or more electron bunches propagating through a pre-ionized plasma (see for example Chen et al. [12], Rosenzweig [13] for a theoretical treatment). In this scheme, the initial, "drive" electron bunch has to be accelerated by conventional technology. In 1988, it was shown for the first time that a second, "witness" electron bunch can be accelerated in the wakefield generated by the drive bunch to relativistic energies [14]. Recently, researchers at the Stanford Linear Accelerator (SLAC) demonstrated that also a single electron bunch can be used both as driver and witness pulse [15]. Here, some electrons of



---

an initial 42 GeV pulse were energy doubled to 84 GeV in a plasma of about 1 m length, while the initial bunch was accelerated on several km length. While this proves the great potential of plasma-based acceleration, it also has to be mentioned that the electron energy spectra obtained in PWFA showed a very broad energy spread.

Plasma-based acceleration mechanisms can also be driven by high-intensity laser pulses, taking away the need for a large scale particle accelerator. In the *Laser wakefield acceleration* scheme (LWFA), the plasma wave is driven by a high-intensity laser pulse instead of a pre-accelerated particle bunch. At the time of their initial proposal of the "Laser Electron Accelerator" in 1979 by Tajima and Dawson [11], the laser technology had not yet been ready to reach the required intensities to drive the acceleration with a single laser pulse. Thus, they also described the *Plasma Beatwave Accelerator* scheme (PBWA), where two lasers that have a frequency difference of the plasma frequency are propagating through the plasma generating a beat wave with the necessary gradients to accelerate relativistic electrons, as shown for example by Everett et al. [16] in 1994.

Around the same time, chirped-pulse amplification (CPA) technology, which was invented by Strickland and Mourou [17] in 1985, had matured and high-intensity laser pulses with ultra-short duration ( $\tau < 1$  ps) could now be produced, releasing the need for a second laser pulse to drive the acceleration. In 1993, Hamster et al. [18] measured the first direct excitation of a plasma wave and soon after Nakajima et al. [19] showed the acceleration of electrons to 18 MeV that had been externally injected into the plasma wave by a second laser pulse. In 1995, even up to 44 MeV energy were achieved with a single laser pulse by Modena et al. [20]. However, it was shown in 1999 theoretically and experimentally that a different acceleration mechanism, the so-called direct laser acceleration (DLA) [21, 22] can co-exist with or even dominate over LWFA, especially for laser pulse durations much longer than the plasma period. The plasma electrons perform transverse oscillations at the betatron frequency  $\omega_\beta$  in the self-generated fields. When  $\omega_\beta$  is in resonance with the laser frequency as observed by the relativistic electrons, laser energy can be directly transferred from the laser to a forward motion of the electrons via the  $\mathbf{v} \times \mathbf{B}$ -force. However, DLA accelerated electrons usually exhibit thermal energy spectra and have no monoenergetic features.

Facilitated by a significant reduction in laser pulse duration due to the usage of a Titanium-Sapphire laser system, Malka et al. were able to generate electron energy spectra with a non-thermal high energy tail above 200 MeV [23]. Although monoenergetic features had not been observed yet, they were able to show that the electrons were accelerated by the wakefield of the laser pulse. At the same time, also the progress in computing power enabled the theoretical side to perform three-dimensional (3D) simulations of LWFA. Pukhov and Meyer-ter-Vehn found the so-called "bubble regime", where electrons could not only be accelerated to energies in the 100 MeV-range, but also showed peaks

in the energy spectrum for the first time in the self-injection scheme (see sec. 1.10 for details about the acceleration mechanism) [24]. This scheme led to a big experimental breakthrough, when three independent research groups managed to generate monoenergetic spectra in the 100 MeV-range in 2004 [25–27].

## Recent developments in laser wakefield acceleration

The first proof-of-principle experiments with quasi-monoenergetic spectra triggered many further investigations of laser wakefield acceleration. Only two years later, another step forward was achieved by reaching the 1 GeV barrier [28, 29]. To date, the highest reported value from a single LWFA-stage has been around 1.5 GeV, although in this case the energy spectrum has been very broad [30]. The current energy frontier in a stage is mainly limited by dephasing of the electrons in the plasma wave (see sec. 1.8) and ultimately the available laser power, thus several acceleration stages, each driven by an individual laser, are currently a hot topic (see for example Leemans and Esarey [31]).

Although a lot of progress has been made over the past years, many LWFA experiments still suffer a lot from instabilities. This is mainly due to the highly nonlinear process of electron injection into the plasma wave, which strongly affects the electron energy spectrum or the overall probability for electron injection and acceleration, making it difficult to perform experiments with the accelerated electron beam such as the undulator radiation measured by Fuchs et al. [32]. Several efforts have been undertaken to control this injection, either by a specific shape of the longitudinal plasma density profile [33–36], one or more additional "injection" laser pulses [37–41], or the usage of gas mixtures [42, 43]. The controlled injection of electrons at a sharp plasma density transition is one of the key results of this thesis and is presented in chapter 3.

Another important part of LWFA research are the electron diagnostics and the visualization of the acceleration process. Most of the output parameters such as electron energy spectrum, charge, and recently also transverse emittance [44, 45] are measured with methods adapted from conventional accelerator technology (see sec. 2.3). However, the ultra-short bunch duration, one of the main advantages of LWFA compared to rf accelerators, has so far eluded precise measurements and has been determined indirectly, yielding only upper limits [46–49] until the recent work of Lundh et al. [50].

Visualization of the acceleration process itself, not only the output parameters, is even more difficult due to the compact size of the accelerator and the timescale on which the relevant processes are happening. In 2006, Matlis et al. [51] succeeded for the first time in recording a time-integrated footprint of the linear plasma wave via frequency-domain shadowgraphy. It was also tried to extend this method to nonlinear plasma waves and

their temporal evolution, however here the correct analysis is more difficult [52, 53]. The electron bunch inside of the plasma was observed directly for the first time via Faraday rotation [54]. Although giving some insights into the acceleration process, measurements so far have only been able to measure either the accelerating plasma wave or the electron bunch with insufficient resolution, but not both simultaneously. The results shown in chapter 4 of this thesis represent the first combination of the two: the observation of the electron bunch via Faraday rotation due to its magnetic field and the visualization of the plasma wave via shadowgraphy, both measurements performed at the same time and with unprecedented spatio-temporal resolution [55].

## List of publications by the author incorporated in this thesis

This thesis is supported by the following journal papers with contributions from the author:

### Chapter 2

[56] A. Buck, K. Zeil, A. Popp, K. Schmid, A. Jochmann, S. D. Kraft, B. Hidding, T. Kudyakov, C. M. S. Sears, L. Veisz, S. Karsch, J. Pawelke, R. Sauerbrey, T. Cowan, F. Krausz, and U. Schramm. Absolute charge calibration of scintillating screens for relativistic electron detection. *Rev. Sci. Instrum.* 81:033301, 2010.

► For this paper I performed the target preparations together with the MPQ team, conducted the measurements together with the other authors at the ELBE accelerator, did the main data analysis, and prepared the manuscript with the support of the other authors.

[44] C. M. S. Sears, S. Benavides Cuevas, U. Schramm, K. Schmid, A. Buck, D. Habs, F. Krausz, and L. Veisz. A high resolution, broad energy acceptance spectrometer for laser wakefield acceleration experiments. *Rev. Sci. Instrum.* 81:073304, 2010.

► For this paper I took part in the discussions and helped in the preparation of the figures and the manuscript.

### Chapter 3

[57] K. Schmid, L. Veisz, F. Tavella, S. Benavides, R. Tautz, D. Herrmann, A. Buck, B. Hidding, A. Marcinkevicius, U. Schramm, M. Geissler, J. Meyer-ter-Vehn, D. Habs, and F. Krausz. Few-cycle laser-driven electron acceleration. *Phys. Rev. Lett.*, 102(12):124801, 2009.

► I took part in the experimental campaign and helped to prepare the manuscript.

[58] L. Veisz, K. Schmid, F. Tavella, S. Benavides, R. Tautz, D. Herrmann, A. Buck, B. Hidding, A. Marcinkevicius, U. Schramm, M. Geissler, J. Meyer-ter-Vehn, D. Habs, and F. Krausz. Laser-driven electron acceleration in plasmas with few-cycle pulses. *Compt. Rend. Phys.*, 10(2-3):140–147, 2009.

► I took part in the experimental campaign and helped to prepare the manuscript.

[35] K. Schmid, A. Buck, C. M. S. Sears, J. M. Mikhailova, R. Tautz, D. Herrmann, M. Geissler, F. Krausz, and L. Veisz. Density-transition based electron injector for laser driven wakefield accelerators. *Phys. Rev. ST Accel. Beams* 13:091301, 2010.

► I prepared the shockfront targets together with K. Schmid, performed the experiments with K. Schmid, C. M. S. Sears and the rest of the LWS-20 team, and assisted K. Schmid in the data evaluation and the preparation of the manuscript.

A. Buck, J. Wenz, J. Xu, J. M. Mikhailova, F. Krausz, S. Karsch, and L. Veisz. Stabilization and control of laser-driven electron acceleration via a sharp density transition. In preparation.

► The experiments have been prepared, conducted, and evaluated by J. Wenz and myself.

## Chapter 4

[55] A. Buck, M. Nicolai, K. Schmid, C. M. S. Sears, A. Sävert, J. M. Mikhailova, F. Krausz, M. C. Kaluza, and L. Veisz. Real-time observation of laser-driven electron acceleration. *Nat Phys.* 7:543, 2011.

► For this paper, I did the main preparation of the experiment, performed the measurements together with the teams from MPQ and Jena, did the main data evaluation together with M. Nicolai, and wrote the paper with the help of all other authors. I developed the ray-tracing code and used it with the simulations performed by J. M. Mikhailova.

## Appendix

[59] J. M. Mikhailova, A. Buck, A. Borot, K. Schmid, C. M. S. Sears, G. D. Tsakiris, F. Krausz, and L. Veisz. Ultrahigh-contrast few-cycle pulses for petawatt-class laser technology. *Opt. Lett.*, 36:3145, 2011.

► I have designed, constructed, and characterized the XPW setup. The experiments in combination with the plasma mirror have been performed by J. M. Mikhailova and myself. I also contributed to the evaluation and the preparation of the manuscript.

# Chapter 1

## Theoretical foundations of high-intensity laser-plasma interaction

Various interesting phenomena are observed in the interaction of high-intensity laser pulses with plasmas, such as the acceleration of charged particles to relativistic energies or the conversion of the incident laser light to different frequencies. This chapter covers the theoretical foundations needed to understand and interpret the experiments on the electron acceleration with laser-driven plasma waves. After discussing the basics of the theoretical description of electro-magnetic waves (sec. 1.1) and the interaction of laser light with single electrons (sec. 1.2) and single atoms (sec. 1.3), laser-produced plasmas (sec. 1.4 and 1.5), and a nonlinear 1D-model for the generation of large-amplitude plasma waves will be treated (sec. 1.6). Finally, specifics to the laser wakefield acceleration process such as wave breaking (sec. 1.7), limits to the acceleration (sec. 1.8), electron injection (sec. 1.10), and particle-in-cell simulations (sec. 1.11) are discussed.

### 1.1 Attributes of light

The propagation of light as an electromagnetic wave is described by Maxwell's equations [60]:

$$\begin{aligned}
\nabla \mathbf{E} &= \frac{\rho}{\epsilon_0} \\
\nabla \mathbf{B} &= 0 \\
\nabla \times \mathbf{E} &= -\frac{\partial \mathbf{B}}{\partial t} \\
\nabla \times \mathbf{B} &= \frac{1}{c^2} \frac{\partial \mathbf{E}}{\partial t} + \mu_0 \mathbf{j}.
\end{aligned} \tag{1.1}$$

Here,  $\epsilon_0$ ,  $\mu_0$ , and  $c$  are the vacuum permittivity, the vacuum permeability and the speed of light that are related to each other through  $c = (\epsilon_0 \mu_0)^{-1/2}$ .  $\rho$  is the charge density and  $\mathbf{j}$  the current density. The electric and magnetic fields  $\mathbf{E}$  and  $\mathbf{B}$  can be expressed by a vector potential  $\mathbf{A}$  and a scalar potential  $\Phi$ . After applying the Lorenz gauge the fields are

$$\begin{aligned}
\mathbf{E} &= -\frac{\partial \mathbf{A}}{\partial t} - \nabla \Phi \\
\mathbf{B} &= \nabla \times \mathbf{A}.
\end{aligned} \tag{1.2}$$

For electro-magnetic plane waves these fields can be expressed in the form

$$\begin{aligned}
\mathbf{E} &= \mathbf{E}_0 \sin(\omega_L t - \mathbf{k}\mathbf{x} + \phi) \\
\mathbf{B} &= \mathbf{B}_0 \sin(\omega_L t - \mathbf{k}\mathbf{x} + \phi).
\end{aligned} \tag{1.3}$$

Here,  $\omega_L$  is the angular frequency,  $\mathbf{k}$  the wave vector with  $|\mathbf{k}| = \omega_L/c$ , and  $\phi$  an arbitrary phase offset. The Poynting vector  $\mathbf{S}$  is defined as the energy flux transported by the electromagnetic wave [60]. In vacuum, it is calculated as

$$\mathbf{S} = \epsilon_0 c^2 (\mathbf{E} \times \mathbf{B}). \tag{1.4}$$

The intensity  $I_L$  of a focused laser pulse in vacuum is calculated by averaging the norm of the Poynting vector (1.4) over one field cycle.

$$I_L = \langle |\mathbf{S}| \rangle_{\text{cycle}} = \epsilon_0 c \langle |\mathbf{E}|^2 \rangle = \frac{1}{2} \frac{E_0^2}{Z_0} \tag{1.5}$$

Here,  $E_0$  is the maximum of the electric field and  $Z_0 = 377 \Omega$  is the so-called impedance of free space. Currently, the highest reported intensity by ultra-short high-power laser systems is  $I = 2 \cdot 10^{22} \text{ W/cm}^2$  [61]. Thus, state-of-the-art laser systems reach electric fields that are significantly larger than the electric field at the Bohr radius inside a hydrogen atom and easily ionize atoms with small atomic numbers completely (see also section 1.3).

## 1.2 Laser pulse interaction with single electrons

The relativistic equation of motion for an electron with mass  $m_e$  and charge  $e$  under the influence of an electro-magnetic field is described by the Lorentz equation

$$m_e \frac{d}{dt}(\gamma \mathbf{v}) = -e(\mathbf{E} + \mathbf{v} \times \mathbf{B}). \quad (1.6)$$

Here,  $\gamma$  is the relativistic factor related to the particle velocity by  $\gamma = 1/\sqrt{1-\beta^2}$  with  $\beta = |\mathbf{v}|/c$ . The following estimation of an electron in a light field will be limited to the sub-relativistic case, i.e.,  $|\mathbf{v}| \ll c$ . Thus, we can neglect the second part of the Lorentz force in eq. (1.6) because of  $|\mathbf{B}| = |\mathbf{E}|/c$ . Using the electric field of a plane wave from eq. (1.3) the equation is simplified to

$$m_e \frac{d}{dt} \mathbf{v} = -e \mathbf{E}_0 \sin(\omega_L t - \mathbf{k} \mathbf{x} + \phi) \quad (1.7)$$

The so-called *quiver velocity* of the electron can be found via a simple integration over time.

$$\mathbf{v}(\mathbf{x}, t) = -\frac{e}{m_e} \int \mathbf{E}_0 \sin(\omega_L t - \mathbf{k} \mathbf{x} + \phi) dt + \mathbf{v}_0 \quad (1.8)$$

Here,  $\mathbf{v}_0$  is the initial velocity which will be set to zero for now. From equation (1.8), it follows that the maximum quiver velocity of the electron is

$$v_{\max} = \frac{e|\mathbf{E}_0|}{m_e \omega_L} = \frac{e|\mathbf{A}_0|}{m_e}. \quad (1.9)$$

Clearly, for a vector potential approaching  $|\mathbf{A}_0| \approx \frac{m_e c}{e}$  the maximum quiver velocity is approaching the speed of light,  $c$ . Thus, the electron reaches relativistic energies, our initial assumption of  $|\mathbf{v}| \ll c$  breaks down, and the  $\mathbf{v} \times \mathbf{B}$ -term has to be taken into account in the Lorentz equation (1.6). A *normalized vector potential*  $a_0$  is defined as

$$a_0 = \frac{|e\mathbf{A}_0|}{m_e c} = \frac{|e\mathbf{E}_0|}{m_e c \omega_L} = 0.854 \sqrt{I_L [10^{18} \text{ W/cm}^2]} \cdot \lambda_L [\mu\text{m}], \quad (1.10)$$

where  $\lambda_L$  is the laser wavelength.  $a_0$  approaches unity at the threshold of the vector potential defined above, thus  $a_0 = 1$  is called the *relativistic threshold*. For typical Ti:sapphire-based (TiSa) laser systems ( $\lambda_L = 800 \text{ nm}$ ) this is reached at laser intensities of  $I_L \approx 2 \cdot 10^{18} \text{ W/cm}^2$ .<sup>1</sup>

<sup>1</sup>The same estimation can also be done for protons. However, due to the large difference in mass, intensities on the order of  $I_L = 10^{24} - 10^{25} \text{ W/cm}^2$  have to be reached to accelerate protons directly to relativistic

The quiver energy of the electron is defined as  $E_q = \frac{1}{2}m_e|v|^2$ . By averaging  $E_q$  over one laser cycle an effective potential  $U_p$  is derived, the so-called *ponderomotive potential*.

$$U_p = \langle E_q \rangle_{\text{cycle}} = \frac{e^2}{4m_e\omega_L^2} |E_0|^2 \propto I_L \lambda^2 \quad (1.11)$$

Since  $U_p$  is proportional to the laser intensity, it will be larger in the center than outside of the focal region. This will exert a net force on the electrons in the focus, the *ponderomotive force*  $F_p$ , which is defined as the spatial derivative of the ponderomotive potential.

$$F_p = -\nabla U_p \quad (1.12)$$

Thus, electrons will be pushed out of the laser focus in all directions depending on the focal spot size and the laser intensity. Solving the electron motion via eq. (1.12) can only be done numerically due to the nonlinearity and complexity of the problem. While the electron motion is purely transverse for small laser intensities, the  $v \times B$ -term can bend the electron motion forward at higher intensities. The ejection angle  $\theta$  from the focus is determined by calculating the electron's transverse ( $p_\perp$ ) and longitudinal momentum ( $p_\parallel$ ).

We start the derivation by looking at the parallel motion of the electron. The momentum of the absorbed photons is conserved by the electron momentum.

$$p_\parallel = \frac{E_{\text{kin}}}{c} = (\gamma - 1)m_e c, \quad (1.13)$$

where  $E_{\text{kin}}$  is the kinetic energy of the electron. A relationship between  $p_\perp$  and  $p_\parallel$  is found with the help of eqns. (1.2) and (1.6).

$$p_\parallel = \frac{1}{2} \frac{p_\perp^2}{m_e c} \quad (1.14)$$

Equations (1.13) and (1.14) can be combined to get the ejection angle  $\theta$ :

$$\tan \theta = \frac{p_\perp}{p_\parallel} = \sqrt{\frac{2}{\gamma - 1}}. \quad (1.15)$$

Experimental verifications of this scheme were performed by Moore et al. [62] and Meyerhofer [63]. By including the normalized vector potential  $a_0$  (1.10) it follows for linear polarization that electrons are accelerated to

---

velocities, which is out of reach for state-of-the-art high power lasers. Even higher laser intensities would be necessary for heavier ions.



$$\gamma \approx \sqrt{1 + \frac{a_0^2}{2}}, \quad (1.16)$$

if the electrons were initially at rest. However, this electron motion is only an instantaneous response to the electric field. Under normal circumstances, the net energy gain of the electrons in the laser focus is zero and the electrons have the same kinetic energy before and after their interaction with the laser pulse. The problem of vacuum acceleration of electrons was treated by Woodward and Lawson [64, 65], who state that electrons cannot experience a net energy gain when the following conditions are fulfilled:

- The interaction region is infinite.
- No boundaries are present.
- The electron is highly relativistic along the acceleration path.
- No static electric or magnetic fields are present.
- Nonlinear effects can be neglected.

The validity of the Lawson-Woodward-theorem is confirmed by the fact that, even though these conditions are never completely fulfilled, experiments on vacuum acceleration have seen only very limited energy gain despite the huge electric fields present in the interaction. For example, Plettner et al. have tried to limit the acceleration region by a foil, still they have only seen an energy gain of 30 keV [66].

Thus, many different schemes to accelerate electrons to relativistic energies in plasmas instead of vacuum have been proposed and experimentally verified over the past decades. Currently, the most successful one in terms of accelerated charge and final output energy is the acceleration via the excitation of large amplitude Langmuir waves in plasmas, commonly referred to as *laser wakefield acceleration* (LWFA) [11], which will be discussed in the next sections.

### 1.3 Laser pulse interaction with single atoms and ionization mechanisms

As discussed in section 1.1 current high-power lasers have the potential to ionize matter completely and create a plasma with freely moving electrons and ions. The ionization mechanism can be either dominated by multi-photon effects or strong laser fields. The

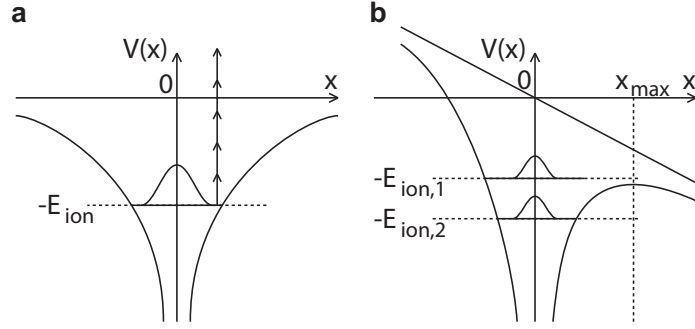


Figure 1.1: **Comparison of different ionization mechanisms.** **a**, Multiphoton ionization, or above-threshold ionization if the energy of the absorbed photons exceeds  $E_{\text{ion}}$  by more than  $\hbar\omega_L$ . **b**, Tunnel ionization ( $E_{\text{ion},2}$ ) and barrier-suppression ionization ( $E_{\text{ion},1}$ ).

limit between the two regimes can be estimated by the Keldysh parameter  $\gamma_k$  [67, 68]. It is derived by calculating the laser field that is necessary to equal the electric field of a proton at the Bohr radius, i.e., the binding potential  $E_{\text{ion}}$  of a hydrogen atom. The Keldysh parameter is therefore derived to

$$\gamma_k = \sqrt{\frac{E_{\text{ion}}}{2U_p}} = \omega_L \sqrt{\frac{m_e c \epsilon_0}{e^2}} \sqrt{\frac{E_{\text{ion}}}{I_L}}. \quad (1.17)$$

For  $\gamma_k > 1$  and thus smaller laser intensities the process is dominated by *multi-photon ionization* (MPI). Here the binding potential is assumed to remain undisturbed and the ionization is treated by perturbation theory (see fig. 1.1a). The special case of *above-threshold ionization* is reached when the energy of the absorbed photons  $E_{\text{phot}} = (N - 1) \hbar\omega_L > eE_{\text{ion}}$  with  $N$  absorbed photons.

Clearly, for  $\gamma_k < 1$ , where the electric field of the laser exceeds the binding potential of the electron, the process cannot be treated with a perturbative approach any more and it is dominated by *tunnel ionization* (TI). TI can be understood by looking at the simple classical picture, in which a Coulomb potential is modified by a stationary, homogeneous field. The combined potential  $V(x)$  is depicted in fig. 1.1b. In the case of  $E_{\text{ion},2}$ , the electron can tunnel through the barrier with finite width. If the electric field is strong enough, so that  $V(x_{\text{max}}) \leq -E_{\text{ion}}$ , the electron can be freed spontaneously. This is the process of *barrier-suppression ionization* (BSI), a special case of TI. The threshold laser intensity  $I_L$  for BSI is estimated by setting  $V_{\text{max}}$  equal to the ionization potential.

$$I_L \left[ \text{W/cm}^2 \right] = \frac{E_{\text{ion}}^4 \pi^2 \epsilon_0^3 c}{2 Z^2 e^6} \approx 4.0 \cdot 10^9 \frac{(E_{\text{ion}}[\text{eV}])^4}{Z^2} \quad (1.18)$$

Here,  $Z$  is the atomic number. Typical values for the BSI-threshold are plotted in tab. 1.1. In fact, this simple model for BSI holds up remarkably well for more complicated electron systems. The calculation of the exact ionization rate itself is more complex. A theoretical treatment can be found for hydrogen-like ions in [67] and for many-electron systems in [69].

Ion	$E_{\text{ion}} (eV)$	$I_L (W/cm^2)$
He <sup>+</sup>	24.59	$1.4 \times 10^{15}$
He <sup>2+</sup>	54.42	$8.8 \times 10^{15}$
N <sup>4+</sup>	77.47	$9.0 \times 10^{15}$
N <sup>7+</sup>	667.0	$1.6 \times 10^{19}$
Ne <sup>5+</sup>	126.1	$4.0 \times 10^{16}$
Ne <sup>10+</sup>	1362	$1.4 \times 10^{20}$
Ar <sup>8+</sup>	143.5	$2.6 \times 10^{16}$
Ar <sup>18+</sup>	4426	$4.7 \times 10^{21}$

Table 1.1: **Ionization potential and intensity threshold for barrier-suppression ionization of relevant elements.**

All the experiments presented in this thesis were performed in Helium targets. Since the intensities were typically on the order of  $10^{18} - 10^{19} W/cm^2$ , the gas is immediately ionized by the laser pulse. In fact, the threshold intensity is already reached about 200 fs before the arrival of the main pulse (fig. 2.3). Therefore, the assumption that a laser pulse is hitting a plasma from a completely ionized gas is valid to treat the following problems.

## 1.4 Non-relativistic, cold, collisionless plasmas

It was shown in sec. 1.3 that the He gas used in the experiments presented in this thesis is completely ionized. Thus, the focused laser pulse interacts with freely moving He ions and electrons, i.e., a plasma. One of the essential properties of a plasma is the complete shielding of an electric field. The characteristic distance over which this takes place is called the *Debye length*  $\lambda_D$  [70].

$$\lambda_D = \sqrt{\frac{\epsilon_0}{e^2} \left( \frac{n_e}{T_e} + \frac{n_0 Z}{T_{\text{ion}}} \right)^{-1}} \quad (1.19)$$

Here,  $T_e$  and  $T_{\text{ion}}$  are the temperatures of the electrons and the ions respectively,  $n_e$  is the electron density, and  $n_0$  the background ion density.  $T_{\text{ion}}$  can be neglected here, because

the ions are immobile on the typical timescales of the experiments (see next paragraphs).

Thus, the Debye length reduces to  $\lambda_D = \sqrt{\frac{\epsilon_0 T_e}{e^2 n_e}}$ .

To simplify all further calculations we will treat a hydrogen plasma, i.e., the electron density  $n_e$  of the unperturbed plasma equals the background ion density  $n_0$ . If the number of particles within the volume of a sphere with a radius  $\lambda_D$  is large, collective interactions become more important than individual scattering events between the charged particles. The plasma is then called collisionless and it can be described as two fluids of electrons and ions with the densities  $n_e$  and  $n_0$  [71]. As we have seen in sec. 1.3, the electron velocities can get close to the speed of light during the interaction. As it is a reasonable assumption to neglect the initial particle velocity, we will therefore assume a *cold* plasma for the following derivations unless stated otherwise.

If an electron is displaced by a small distance  $\Delta x$  from its equilibrium position and  $\Delta x < \lambda_D$ , the originating field pulling back the electron will not be screened by the plasma and net restoring force  $\mathbf{F} = -e\mathbf{E}$  will act on the particle. After being pulled back to its initial position the electron will overshoot due to the acquired kinetic energy. Thus, the electron will perform a harmonic oscillation. By solving the equation of motion one can calculate a characteristic frequency for this oscillation, the *plasma frequency*.

$$\omega_p = \sqrt{\frac{n_e e^2}{\epsilon_0 m_e}} \quad (1.20)$$

Analogously, the characteristic frequency for ions can be derived by replacing the electron charge and mass with the corresponding values. Due to the increased mass, the ions are moving much slower than the electrons. The ions are therefore regarded as a stationary, immobile background on the timescales relevant for the presented experiments.

## 1.5 Laser propagation in underdense plasmas

### Dispersion relation in plasmas

To understand laser propagation through plasmas we go back to Maxwell's equations (1.1) and the plane wave ansatz (1.3). The combination of Faraday's and Maxwell's law leads to the well-known wave equation:

$$(c^2 |\mathbf{k}|^2 - \omega_L^2) \mathbf{E} = -\frac{n_e e^2}{\epsilon_0 m_e} \mathbf{E}. \quad (1.21)$$

The pre-factor on the right hand side of the equation is recognized as the plasma frequency from eq. (1.20). Thus, we can write the dispersion relation for electromagnetic waves in

plasmas:

$$\omega_L^2 = c^2 k^2 + \omega_p^2. \quad (1.22)$$

The dispersion relation shows that light with  $\omega_L < \omega_p$  cannot propagate in a plasma. In this case, the plasma is called *overdense* and the laser pulse is reflected from the vacuum-plasma boundary, an effect which is exploited for example in the generation of higher harmonics of the initial laser pulse from solid targets (see for example von der Linde et al. [72], Gibbon [73], Lichters et al. [74] for first experimental and theoretical observations). The threshold density above which the laser is reflected is called the *critical density*  $n_c = m_e \epsilon_0 \omega_L^2 / e^2$ . For TiSa-lasers with a central wavelength of  $\lambda = 800$  nm the critical density is  $n_c = 1.74 \cdot 10^{21} \text{ cm}^{-3}$ . The typical electron densities for laser wakefield generation are on the order of  $n_e = 10^{18} - 10^{19} \text{ cm}^{-3}$ , thus  $n_e/n_c \approx 0.01$  and the plasma is called *underdense*.

### Index of refraction

Now we can calculate the phase and group velocity  $v_{\text{ph}}$  and  $v_g$  with eq. (1.22) for the laser propagation in the plasma with the index of refraction  $\eta$ .

$$\begin{aligned} v_{\text{ph}} &= \frac{\omega_L}{k} = \frac{c}{\eta} \\ v_g &= \frac{d\omega_L}{dk} = \eta c \\ \text{with } \eta &= \sqrt{1 - \frac{\omega_p^2}{\omega_L^2}} \end{aligned} \quad (1.23)$$

Thus, we see that although the refractive index of an underdense plasma is always smaller than unity, the group velocity  $v_g$  of the laser pulse is still smaller than the vacuum speed of light  $c$ .

### Faraday effect in plasmas

The polarization of a laser pulse is rotated via the Faraday effect if the light is propagating through a dispersive medium with a collinear magnetic field. This effect is used in the experiments described in chapter 4 to visualize the magnetic field of the accelerated electrons in the plasma. The polarization rotation angle  $\varphi_{\text{rot}}$  depends on the magnetic field strength  $\mathbf{B}$ , the propagation length  $s$ , and the Verdet constant  $V$  of the material [75].

$$\varphi_{\text{rot}} = V s \cdot \mathbf{B} \quad (1.24)$$

The Verdet constant is defined as

$$V(\lambda) = V_0 \lambda \frac{d\eta}{d\lambda} \quad (1.25)$$

with  $V_0 = -e/2cm_e$ . Rewriting the index of refraction from eq. (1.23) as a function of  $\lambda$ , we obtain

$$\begin{aligned} \eta(\lambda) &= \sqrt{1 - \frac{n_e}{n_c(\lambda)}} \\ &= \sqrt{1 - \frac{n_e e^2}{4\pi^2 \epsilon_0 m_e c^2} \lambda^2}. \end{aligned} \quad (1.26)$$

Taking the derivate, we get for typical underdense plasmas with  $n_e \ll n_c(\lambda)$ :

$$\frac{d\eta(\lambda)}{d\lambda} \lambda \approx -\frac{n_e}{n_c(\lambda)}. \quad (1.27)$$

Substituting eq. (1.27) into eq. (1.24) we get for the integrated rotation angle along a path  $l$  through the plasma:

$$\varphi_{\text{rot}} = \frac{e}{2m_e c n_c(\lambda)} \int_l n_e \mathbf{B} \cdot d\mathbf{s}. \quad (1.28)$$

### Refraction at the plasma and ray-tracing

We have seen that the index of refraction inside of underdense plasmas is always smaller than unity. In the experiment, the plasma will be surrounded by non-ionized Helium gas, which has a refractive index close to unity. Thus, a probe laser propagating through the gas target is refracted at the plasma surface as depicted in fig. 1.2. In contrast to normal glass lenses, convex plasma regions defocus and concave regions focus the laser pulse.

However, in reality there are not two distinct regions with different index of refraction, but a continuous variation of  $\eta$  along the light propagation path instead. This path of a test ray can be calculated by ray-tracing. We recall Snell's law for the refraction at the boundary between region 1 and 2.

$$\frac{\sin \theta_1}{\sin \theta_2} = \frac{\eta_2}{\eta_1} \quad (1.29)$$

By defining  $\Delta\eta = \eta_2 - \eta_1$  and  $\Delta\varphi = \varphi_2 - \varphi_1$  we can write

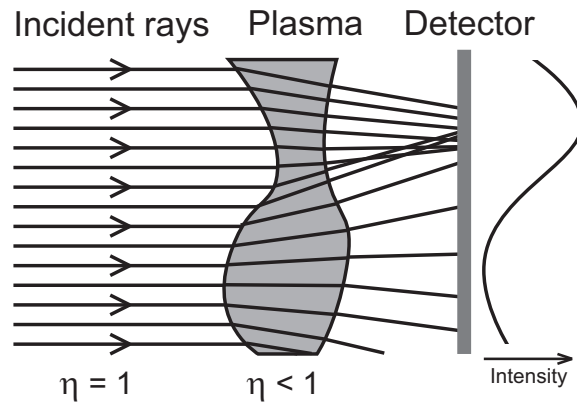


Figure 1.2: **Refraction of a probe beam at the plasma.** The incident rays are refracted upon entering and exiting the ionized region due to the change in refractive index. When sending a probe beam through the plasma, a detector on the other side will thus see bright and dark patches.

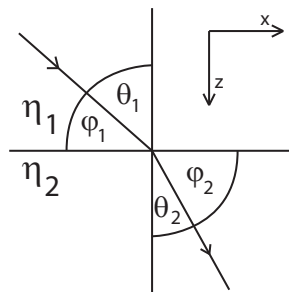


Figure 1.3: **Snell's law.** Definition of angles.

$$\eta_1 \cos \varphi_1 = \cos(\varphi_1 + \Delta\varphi) \cdot (\eta_1 + \Delta\eta). \quad (1.30)$$

With the assumption of  $\Delta\varphi \ll 1$  and  $\Delta\eta \ll \eta_1$ , which will be justified below, we get

$$\begin{aligned} \eta_1 \Delta\varphi \sin \varphi_1 &= \Delta\eta \cos \varphi_1 \\ \Delta\varphi &= \frac{1}{\eta_1} \frac{\Delta\eta}{\tan \varphi_1} \\ &= \frac{1}{\eta_1} \frac{\Delta\eta}{\Delta z} \Delta x. \end{aligned} \quad (1.31)$$

If the steps  $\Delta x$  are infinitely small, the refraction angle  $\Delta\varphi$  and the local change in refractive index  $\Delta\eta$  will also be small since no sharp boundaries are crossed, so that the assumption from above is valid. We will then arrive at the differential form

$$d\varphi = \frac{1}{\eta_1} \frac{d\eta}{dz} dx. \quad (1.32)$$

This effect can be used to visualize plasma waves via shadowgraphy [76]. Strongly nonlinear plasma waves have large electron density fluctuations as described in the next section, which leads to large gradients of the refractive index.

Light rays propagating into a plasma with increasing density are reflected at a certain depth depending on the angle  $\theta$ , which is the angle between the propagation direction  $\mathbf{k}$  and the refractive index gradient  $\nabla\eta$  [71]:

$$n_r = n_c \cos^2 \theta \quad (1.33)$$

Here,  $n_r$  is the density where the laser will be reflected. Thus, we see that for normal incidence the laser is reflected at the critical density, as described at the beginning of the section, while it is reflected already at lower densities for larger angles.

### Relativistic induced transparency

For relativistic plasma waves the plasma frequency  $\omega_p$  has to be corrected by the relativistic factor of the electrons constituting the plasma wave  $\gamma$ .

$$\omega_{p,rel} = \frac{\omega_p}{\sqrt{\gamma}} \quad (1.34)$$

The combination with the dispersion relation (1.22) shows that an initially overdense plasma can become underdense and transparent if the laser intensity and thus the relativistic factor  $\gamma$  is large enough. This effect is called *relativistic induced transparency*.



### Relativistic self-focusing and guiding

Additionally, a high intensity laser pulse propagating through a plasma also experiences self-focusing, which is dominated by two different mechanisms depending on the laser pulse length. We consider an intensity profile  $I(r, z)$

$$I(r, z) = I_0 \left( \frac{w_0}{w(z)} \right)^2 e^{-r^2/w(z)^2}$$

$$\text{with } w(z) = w_0 \sqrt{1 + \left( \frac{z}{z_R} \right)^2} \quad (1.35)$$

$$\text{and } z_R = \frac{\pi w_0^2}{\lambda}.$$

Now, the index of refraction will have a maximum on axis due to two different effects. Firstly, the electron density is lower due to the ponderomotive expulsion of electrons, and secondly, the electron inertia will be higher due to a higher  $\gamma$ . The index of refraction (1.23) can be rewritten as

$$\eta(r, z) = \sqrt{1 - \left( \frac{\omega_p}{\omega_L} \right)^2 \frac{n'_e(r, z)}{n_e \gamma(r, z)}} \approx 1 - \frac{1}{2} \left( \frac{\omega_p}{\omega_L} \right)^2 \left( 1 + \frac{\delta n_e}{n_e} - \frac{a_0^2(r, z)}{4} \right). \quad (1.36)$$

Here,  $n'_e$  is the local electron density and  $\delta n_e = n'_e - n_e$ . This change in refractive index leads to a smaller phase velocity in the laser focus and thus to self-focusing. We will now focus on *relativistic self-focusing* ( $\langle a_0^2 \rangle$ -term) since the contribution of *ponderomotive self-focusing* (caused by the  $\delta n_e/n_e$ -term) is only important for laser pulses that are significantly longer than the plasma wavelength, which is typically not the case for laser wakefield acceleration experiments. The laser power necessary for relativistic self-focusing is estimated via geometrical considerations. A focused laser beam will diffract according to eq. (1.35) as

$$\theta = \frac{\lambda}{\pi w_0}. \quad (1.37)$$

The critical power for self-focusing is reached, when the diffraction is balanced by self-focusing. The phase velocity difference between the center and a position  $r$  off-axis can be written as

$$\frac{\Delta v_p(r)}{c} = \frac{\omega_p^2}{8\omega_L^2} (a_0^2(0) - a_0^2(r)). \quad (1.38)$$

The maximum phase velocity difference is thus

$$\left| \frac{v_p(r)}{c} \right|_{\max} = \frac{\omega_p^2 a_0^2}{\omega_L^2 8}. \quad (1.39)$$

The difference in phase velocity leads to focusing of the laser pulse with the angle

$$\alpha = \sqrt{\frac{\omega_p^2 a_0^2}{\omega_L^2 4}}. \quad (1.40)$$

Via comparison of the two angles  $\theta$  and  $\alpha$  we arrive at the critical power for self-focusing of

$$P_{\text{crit}} [\text{GW}] \approx 17 \frac{\omega_L^2}{\omega_p^2}. \quad (1.41)$$

The typical experiments with Light Wave Synthesizer 20 (LWS-20) presented in this thesis have been performed at a plasma density of  $n_0 \approx 3.0 \cdot 10^{19} \text{ cm}^{-3}$  and a laser wavelength of  $\lambda = 800 \text{ nm}$ . Thus, we get  $\omega_L^2/\omega_p^2 \approx 0.02$  and the critical power is  $\approx 1 \text{ TW}$ , a value that is easily reached with LWS-20. However, as shown by Sprangle et al. [77, 78], when considering pulses that are shorter than the plasma wavelength ( $L = \tau_L c < \lambda_p$ ), also the longitudinal bunching of the plasma density has to be taken into account. This leads to an increase of the critical power for self-focusing up to infinity in the leading edge of the laser pulse [79]. Thus, it is not possible to self-guide pulses that are significantly shorter than the plasma wavelength over long distances. However, it has been shown that some extension of the Rayleigh range up to several  $z_r$ 's is possible because the hardly self-focusable leading edge of the pulse depletes faster than it diffracts. If guiding over longer distances is desired, external guiding mechanisms have to be used (see also sec. 1.8).

## 1.6 Excitation of large-amplitude Langmuir waves

As seen in sec. 1.5, laser pulses can easily propagate in underdense plasmas. Strongly focused high-power lasers displace a large amount of the plasma electrons due to the ponderomotive force [see eq. (1.12)] and therefore excite large-amplitude Langmuir waves in the plasma trailing the laser pulse. The evolution of these plasma waves has first been described by Akhiezer and Polovin [10], at that time (before the invention of the laser) of course not including the excitation of these waves by ultrashort laser pulses. Subsequently, the theoretical description has been refined by several groups [77, 80–82]. The derivation of the one-dimensional nonlinear wakefield in the next paragraphs is following

the description given in Gibbon [68]. We start our calculation by recalling the Lorentz equation (1.6).

$$\frac{d\mathbf{p}}{dt} = -e(\mathbf{E} + \mathbf{v} \times \mathbf{B}) \quad (1.42)$$

By assuming a plane wave pulse that is propagation into the positive x-direction and is linearly polarized along the y-axis, we can calculate the transverse momentum by replacing the fields with vector and scalar potentials (1.2):

$$\begin{aligned} \frac{dp_y}{dt} &= -eE_y + ev_x Bz = e \frac{dA_y}{dt} \\ p_y &= eA_y. \end{aligned} \quad (1.43)$$

This corresponds to

$$\gamma\beta_y = a_0 \quad (1.44)$$

in normalized variables. Writing down the equation for the longitudinal motion gives

$$\frac{d}{dt}(\gamma\beta_x) = c \left( \frac{\partial\phi_0}{\partial x} - \frac{1}{2\gamma} \frac{\partial a_0^2}{\partial x} \right). \quad (1.45)$$

Here, the normalized scalar potential  $\phi_0 = \frac{e\Phi}{mc^2}$  was used. For the following calculations we also need the continuity equation that can be derived from Maxwell's equations (1.1).

$$\frac{\partial n_e}{\partial t} + c \frac{\partial}{\partial x}(n_e \beta_x) = 0 \quad (1.46)$$

Also necessary is Poisson's equation:

$$\nabla^2 \phi_0 = \frac{\omega_p^2}{c^2}(n - 1). \quad (1.47)$$

Here,  $n = n_e/n_0$  is the normalized electron density. The transverse momentum equation (1.44) can be used to calculate the relativistic  $\gamma$ -factor of the electrons constituting the plasma wave

$$\gamma = (1 - |\boldsymbol{\beta}|^2)^{-1/2} = (1 - \beta_x^2 - \beta_y^2)^{-1/2} = \frac{\sqrt{1 + a_0^2}}{\sqrt{1 - \beta_x^2}} \quad (1.48)$$

It is common to split  $\gamma$  into an  $a_0$ -dependent transverse part and a longitudinal part:

$$\gamma = \gamma_{\perp}\gamma_{\parallel} \quad \text{with} \quad \begin{cases} \gamma_{\perp} = (1 + a_0^2)^{1/2} \\ \gamma_{\parallel} = (1 - \beta_x^2)^{-1/2} \end{cases}. \quad (1.49)$$

Equations (1.45) - (1.48) now present a closed set of equations for the coupled electromagnetic and plasma waves. The equations are then transformed into a frame that is co-moving with the laser pulse at the group velocity  $v_g$ . The new coordinates are  $\tau = t$  and  $\xi = x - v_g t$ . Another simplification is applied with introduction of the so-called *quasi-static approximation* (QSA). The typical timescale of the evolution of the laser pulse envelope is on the order of the Rayleigh diffraction time, which is the time it takes for the laser pulse to propagate one Rayleigh length. Since this is much longer than a laser period, we can effectively neglect  $\partial/\partial\tau$  relative to  $\partial/\partial\xi$ . Finally, we arrive at the following expressions (see Gibbon [68] for more details about the derivation).

$$\begin{aligned} \gamma &= \gamma_g^2(1 + \phi_0)(1 - \beta_g\Psi) \\ \beta_x &= \frac{\beta_g - \Psi}{1 - \beta_g\Psi} \\ n &= \beta_g\gamma_g^2\left(\frac{1}{\Psi} - \beta_g\right) \\ \text{with } \Psi &= \sqrt{1 - \frac{1 + a_0^2}{\gamma_g^2(1 + \phi_0)^2}}. \end{aligned} \quad (1.50)$$

Here,  $\beta_g = v_g/c$  is the normalized laser group velocity and  $\gamma_g$  is the corresponding  $\gamma$ -factor. Additionally, a second order, nonlinear, ordinary differential equation for the normalized scalar potential is derived

$$\frac{\partial^2}{\partial\xi^2}\phi_0 = \frac{\omega_p^2}{c^2}\gamma_g^2\left[\frac{\beta_g}{\Psi} - 1\right]. \quad (1.51)$$

This differential equation can no longer be solved analytically. However, numerical solutions are easily obtained. Once the potential  $\phi_0$  is determined numerically, the other parameters can be calculated. One solution for the typical experimental parameters is shown in fig. 1.4. Despite being just a rather simple picture, the one-dimensional nonlinear theory already shows the main characteristics of strongly-driven Langmuir waves in plasmas. For high laser intensities ( $a_0 \geq 1$ ) the plasma wave becomes strongly nonlinear. The electron density maxima become more and more peaked, leading to strong, linear electric fields between those maxima. These fields can now be exploited for the acceleration of relativistic electrons.

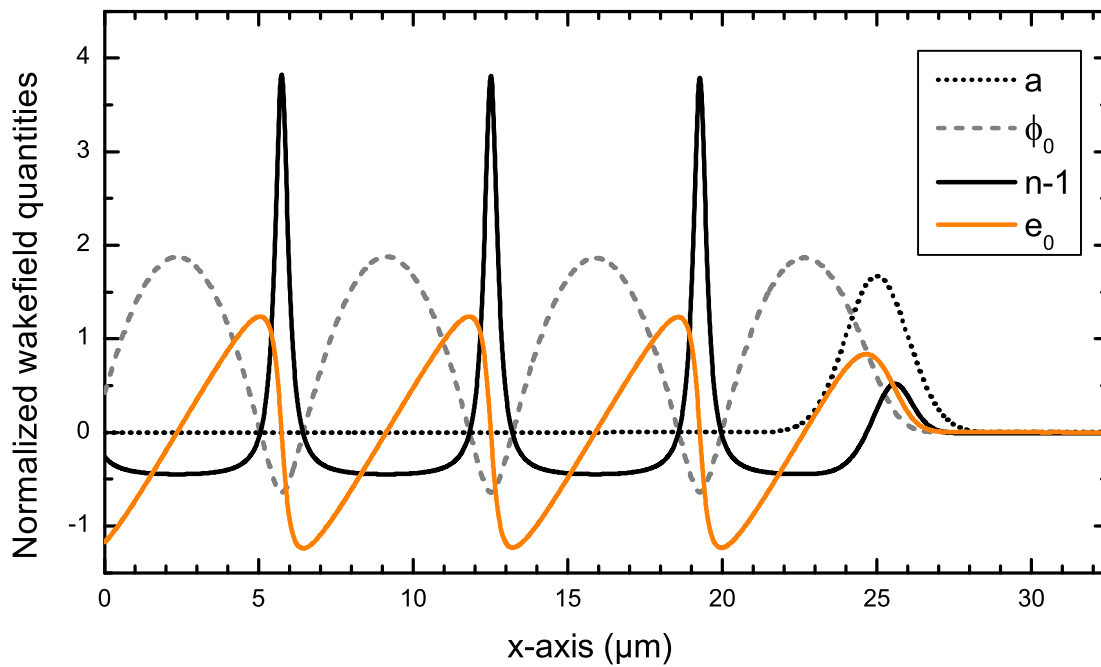


Figure 1.4: **Nonlinear, one-dimensional wakefield in the quasi-static-amplitude approximation.** Simulation parameters:  $a_0 = 1.67$ ,  $n_e = 3.5 \cdot 10^{19} \text{ cm}^{-3}$ ,  $\tau = 8 \text{ fs}$ .  $e_0 = -c\omega_p^{-1}\partial\phi_0/\partial\xi$  is the normalized longitudinal electric field.

Berezhiani and Murusidze have obtained an analytical solution for eq. (1.51) by assuming a square temporal profile and group velocity of  $\beta_g \rightarrow 1$  [83]. They found for the scaling of the scalar potential  $\phi_0$  and the peak electric field  $e_0$

$$\begin{aligned}\phi_{0,\max} &\sim a_0^2 \\ E_{0,\max} &\sim \frac{a_0^2}{\sqrt{1+a_0^2}}\end{aligned}\tag{1.52}$$

However, driving the wakefield efficiently not only depends on  $a_0$ , but also on the ratio between the plasma wavelength  $\lambda_p$  and the laser pulse duration  $\tau_{\text{FWHM}}$ . The normalized electric field divided by the scaling factor from eq. (1.52) is shown in fig. 1.5, where  $e_{\text{max, norm}}$  is calculated for Gaussian laser pulses with different  $a_0$  and pulse durations. It can be seen that the wakefield is driven most efficiently if the duration of the laser pulse has approximately half the length of the plasma period  $\lambda_p$  ( $\tau_{\text{FWHM}} \approx \lambda_p/2$ ). For higher laser intensities the best pulse duration is shifted to smaller values, while the electric field grows roughly linearly with  $a_0$  for  $a_0 > 3$  at the same time.

## 1.7 Maximum attainable field and longitudinal wave breaking

In the previous section we looked at the dynamics of the plasma wave excited by a high-intensity laser, where it was shown that linear electric fields with large amplitudes can be generated. However, electrons are typically not trapped and accelerated by the plasma wave. The injection of electrons into the accelerating phase of the plasma wave can be achieved by longitudinal wavebreaking. Thus, let us go back to eq. (1.46). Following the derivation in [84, 85] we assume solutions for  $n_e(x, t)$  and  $\beta_x(x, t)$  that only depend on  $\tau = t - x/v_g$ . Thus, the equation can be expressed as

$$\frac{n_e}{n_0} = \frac{1}{1 - \frac{\beta_x}{\beta_p}}.\tag{1.53}$$

Here,  $\beta_p$  is the phase velocity of the plasma wave, which equals the laser group velocity  $\beta_g$  for a laser-driven plasma wave. In the equation, an important feature of longitudinal plasma waves becomes apparent. For electron velocities  $\beta_x$  approaching  $\beta_p$  the electron density has a singularity and neighbouring charge sheets start to cross each other. This process is called *longitudinal wave breaking* and sets a limit to the maximum electric

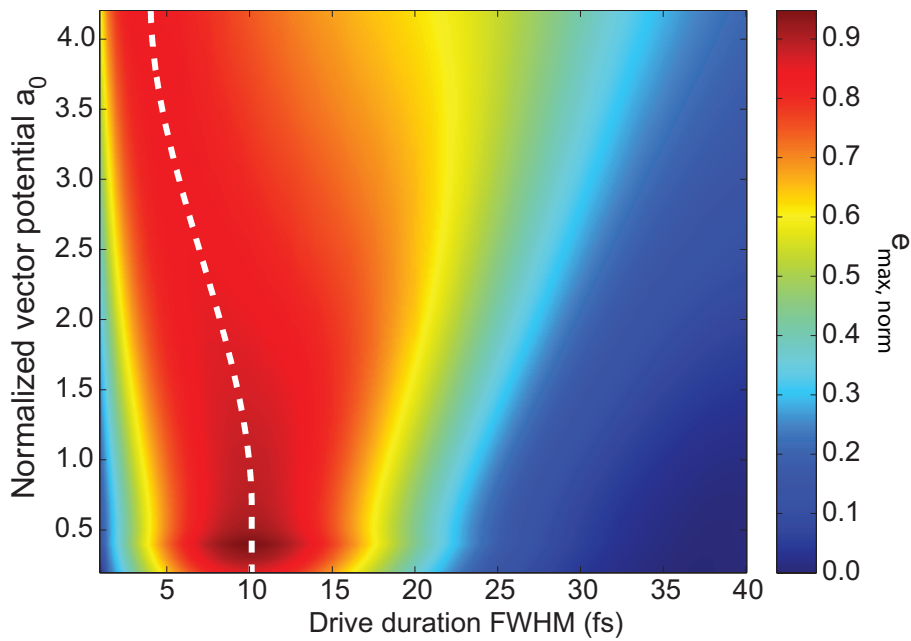


Figure 1.5: **Optimum wakefield driving conditions.** Plotted is the maximum of the normalized electric field  $e_0$  from fig. 1.4 divided by the scaling factor from eq. (1.52) for different drive laser durations and intensities. The plasma density is  $n_e = 3.5 \cdot 10^{19} \text{ cm}^{-3}$ , corresponding to  $\lambda_p = 5.6 \mu\text{m}$ .

field supported by the plasma wave. Obviously, here the fluid description of the plasma breaks down and numerical, particle-in-cell simulations have to be used to investigate the processes further (see also sec. 1.11). The *non-relativistic cold wave breaking limit* (see for example Esarey et al. [79]), is

$$E_{x,max} [\text{V/m}] \approx \frac{m\omega_p c}{e} = 96 \sqrt{n_0} [cm^{-3}]. \quad (1.54)$$

The situation changes for relativistic fluid velocities. The electric field as found in the literature [10, 84] is

$$E_x = \frac{m\omega_p c}{e} \sqrt{2(\gamma_m - \gamma(\tau))}. \quad (1.55)$$

Here,  $\gamma_m$  corresponds to the maximum of the fluid velocity  $\beta_x$ . We can see from the formula and in fig. 1.4 that the electric field is zero at the position with the highest fluid velocity, which cannot be larger than  $\beta_p$ . The electric field is maximized for  $\beta_x = 0$

$$E_{x,max} = \frac{m\omega_p c}{e} \sqrt{2(\gamma_p - 1)} \stackrel{\gamma_p \gg 1}{\approx} \frac{m\omega_p c}{e} \left(4 \frac{n_c}{n_e}\right)^{1/4}, \quad (1.56)$$

where  $\gamma_p = \sqrt{1 - (v_g/c)^2}^{-1} = \sqrt{n_c/n_e}$  is the relativistic  $\gamma$ -factor of the plasma wave. This limit drops for warm plasmas because electrons with higher initial velocity can travel out of the high density spike below the cold wave breaking threshold and be trapped in the plasma wave (see Sheng and Meyer-ter-Vehn [84] for a detailed analytical treatment).

So far, the necessary electric field for wave breaking has been described, however the specific condition for an electron to be trapped within the accelerating phase of the plasma wave has not been discussed yet. The Hamiltonian, i.e., the sum of potential and kinetic energy, for a single electron in the plasma wave structure (fig. 1.4) is derived for the co-moving frame by Esirkepov et al. [86].

$$h(\xi, p_x) = \sqrt{1 + p_x^2 + a(\xi)^2} - \beta_p p_x - \phi_0(\xi) = \text{const.} \quad (1.57)$$

Here,  $\xi = x - v_g t$  is the spatial coordinate in the co-moving frame as in the previous sections. We can now plot the longitudinal phase space with the above equation to explore the electron motion (fig. 1.6). Areas of constant Hamiltonian are plotted in the same colour. The electrons are moving in the phase space along trajectories of constant total energy. Looking at the figure, different types of trajectories can be identified. Electrons moving on trajectory 1 are the electrons constituting the plasma wave. The electrons are initially at rest and are pushed forward ( $p_0 > 0$ ) by the ponderomotive force upon the arrival of the laser pulse. Despite being accelerated forward, they are not fast enough and are overtaken



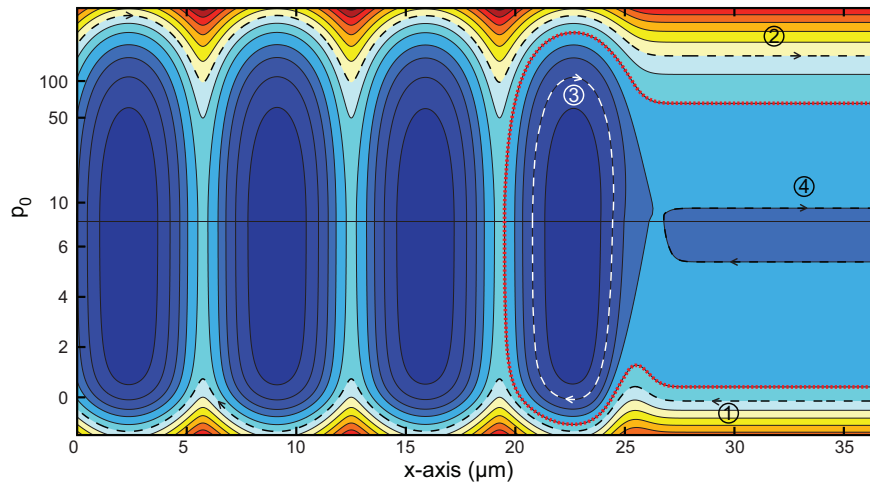


Figure 1.6: **Longitudinal phase-space in the one-dimensional model.** Test electrons with zero initial kinetic energy follow path 1, while electrons with high initial momentum (here:  $p_0 > 7$ ) can follow path 2 and overtake the plasma wave. These two paths are distinguished from path 3 (trapped electrons) by the separatrix (red dotted line). Path 4 is a special case of particles with a certain initial forward momentum that are accelerated forward by the ponderomotive force.

by the laser pulse and pushed backward again ( $p_0 < 0$ ) starting their oscillations as part of the plasma wave. The electrons effectively travel backwards in the plasma wave, i.e., they oscillate around their rest position in the non-comoving frame. Trajectory 2 symbolizes electrons with high initial momentum overtaking the plasma wave from behind. Electrons moving on trajectory 3, however, are trapped in the plasma wave. They are moving clockwise in the phase space while they are being accelerated and decelerated. The highest point in the trajectory, i.e., the position of maximum forward momentum is the point of dephasing (see sec. 1.8). The border between regions 1+2 and region 3 is called the separatrix [87]. Trajectory 4 represents a special trajectory of particles that have initially already a large forward momentum and get only a small extra kick to be faster than the laser pulse.

Under normal experimental conditions most plasma electrons are moving on trajectory 1. Thus they have a negligible initial velocity and are oscillating forward and backward after being hit by the laser pulse. For electron acceleration the particles would need to cross the separatrix to be trapped on trajectory 3. However, this is not included in this simple 1D model and no electron trapping can occur. Sec. 1.10 will elaborate more on how electrons can be injected into plasma waves and be trapped via wave breaking or other mechanisms.

## 1.8 Limiting factors for the acceleration of electrons

The maximum attainable field in a laser-driven plasma wave has been discussed in the previous chapter. Unfortunately, current laser-plasma accelerators cannot be extended infinitely, thus the final electron energy is determined by the interplay between the accelerating electric field and the distance over which this field can be sustained. The relevant physical effects limiting the acceleration distance are discussed in the next sections.

### Diffraction

Probably the most obvious effect is the diffraction of the laser pulse. The high electric fields in the plasma wave require a high laser intensity. Outside of the Rayleigh range  $z_R$  [eq. (1.35)] the laser spot grows quickly, which reduces the intensity. We have seen in sec. 1.5 that ultra-short laser pulses cannot be guided over more than a few  $z_R$ 's by the self-focusing mechanisms. Experimentally, external guiding can be achieved by a longitudinal discharge fired nanoseconds before the arrival of the main laser pulse [28, 29].

### Depletion

The laser pulse loses energy continuously during the propagation through the plasma, mainly to sustain the plasma wave. When the laser has lost a substantial amount of its energy the plasma wave amplitude will decrease and thus the acceleration is terminated. The *pump depletion length* is estimated by comparing the laser pulse energy to the energy left in its wake. For linearly polarized, square laser pulses the following expression is derived [79].

$$L_{\text{depl}} = \left( \frac{\omega_L}{\omega_p} \right)^2 \lambda_p \times \begin{cases} \frac{2}{a_0^2} & \text{for } a_0 \leq 1 \\ \frac{\sqrt{2}}{\pi} a_0 & \text{for } a_0 \gg 1. \end{cases} \quad (1.58)$$

### Dephasing

In section 1.5, the index of refraction  $\eta$  and the laser group velocity  $v_g$  have been derived. Relativistic electrons can reach velocities that can get infinitely close to the vacuum speed of light during the acceleration. The plasma wave, however, is bound to the group velocity of the laser, which is also close to the speed of light, but roughly by a factor of  $(10^{-4} - 10^{-5}) \cdot c$  smaller for typical laser and plasma parameters. Thus, after some acceleration distance the electrons are faster than the plasma wave and can propagate out-of-phase

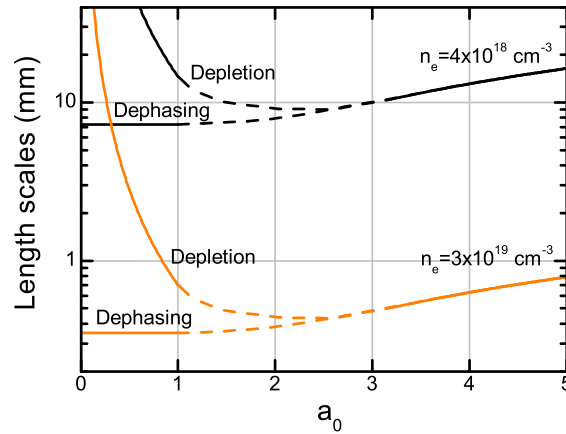


Figure 1.7: **Comparison of dephasing and depletion length.** Plotted are the dephasing and depletion lengths at two electron densities for the low intensity  $a_0 \leq 1$  and the high intensity  $a_0 \gg 1$  case. The dashed line shows interpolated values for the intermediate range.

and into the decelerating part of the plasma wave (see fig. 1.4). The dephasing for non-relativistic intensities can be calculated by estimating the distance it takes the electrons to advance  $\lambda_p/2$  with respect to the plasma wave.

$$L_{\text{deph}} = \frac{\pi}{\omega_p} \frac{c}{\frac{c}{v_p} - 1} \approx \frac{\lambda_p^3}{\lambda^2} \quad (1.59)$$

A more rigorous derivation for linearly polarized, square laser pulses with arbitrary intensities can be found in Esarey et al. [79]:

$$L_{\text{deph}} = \left( \frac{\omega_L}{\omega_p} \right)^2 \lambda_p \times \begin{cases} 1 & \text{for } a_0 \leq 1 \\ \frac{\sqrt{2}}{\pi} a_0 / N_p & \text{for } a_0 \gg 1. \end{cases} \quad (1.60)$$

Here,  $N_p$  is the number of plasma periods behind the drive laser pulse (typically  $N_p = 1$ )<sup>2</sup>. We can see from the formula that the dephasing length is longer for a smaller plasma density. Thus, rather low densities are necessary to reach the highest electron energies.

A comparison of depletion and dephasing effects is illustrated in fig. 1.7. As already seen from the formula, the depletion and dephasing lengths are matched for  $a_0 \geq 2$ . For smaller intensities the energy gain is limited by dephasing. In principal, dephasing can

<sup>2</sup>For linear wakefields the dephasing length is decreased by a factor of 2, since the part of the plasma wave where the electrons are both accelerated and focused is only  $\lambda_p/4$ . For the experiment eq. (1.60) should be regarded as an estimate.

reduce the energy spread of the accelerated electron bunch, which has been injected over a longer period. This can be understood by recalling the phase-space plot (fig. 1.6). The accelerated electrons form a line of certain length (depending on the time interval of electron injection) that is following path 3. If the electrons are dephased, i.e., they reach the maximum forward momentum in the trajectory, they have a similar momentum and thus a small energy spread. However, the electron energy will be limited and the laser to electron energy conversion  $\eta$  will be small in this case. Thus, it should be taken care that  $a_0$  is big enough to reach a certain amount of laser depletion and an efficiency of  $\eta > 1\%$ . It should also be mentioned that the Rayleigh range can be smaller than  $L_{\text{deph}}$  and  $L_{\text{depl}}$  for some experimental parameters. Especially when self-focusing in the plasma is involved, the distance over which the laser intensity is high enough for electron acceleration can be rather short. However, this effect has to be studied separately for each experimental situation since it depends strongly on the parameters such as peak intensity and plasma density.

### Maximum energy gain

The maximum energy gain  $\Delta W$  of the electrons is determined by the acceleration length and the electric field. Since  $L_{\text{deph}} < L_{\text{depl}}$  for typical experimental parameters ( $a_0 \approx 1 - 2$ ),  $\Delta W$  is given (if self-focusing is not the limiting factor) by Esarey et al. [79]:

$$\Delta W = eE_{\text{acc}}L_{\text{deph}} \approx \frac{630 I [\text{W}/\text{cm}^2]}{n_e [\text{cm}^{-3}]} \times \begin{cases} 1 & \text{for } a_0 \leq 1 \\ \frac{2}{\pi N_p} & \text{for } a_0 \gg 1 \end{cases} . \quad (1.61)$$

As it will be shown in the experimental part of the thesis, sometimes the acceleration length can also be shorter than  $L_{\text{deph}}$  because of the dimensions of the plasma. In most cases however, the acceleration is limited by one of the effects mentioned above.

### Beamloading

So far, the effect of the electrons loaded into the plasma wave has been neglected and only test electrons that have no influence on the fields have been treated. Thus, the maximum energy gain derived above is only true if a small number of electrons are injected into the plasma wave. However, if the loaded charge is significant, which is of course desired for the accelerator, the longitudinal electric field of the plasma wave is locally modified (see fig. 1.8). This effect has been studied in great detail in theory and in experiments [88–91].

Generally, electrons that are accelerated in the plasma wave will be out-of-phase with the electrons constituting the plasma wave. Thus, their electric field will counteract the

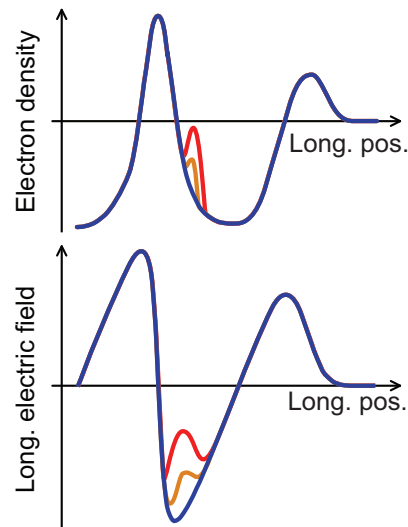


Figure 1.8: **Illustration of the beamloading effect.** The blue curves show the undisturbed electron density and electric field without injected electron bunch. For an injected electron bunch with low charge the accelerating field is reduced and can actually be flattened (orange). For higher charges the field is strongly reduced and distorted, leading to a low energy electron bunch with large energy spread (red).

fields of the plasma wave and damp the accelerating field. A general rule of thumb is therefore that for a given laser power, the more charge is accelerated the lower the electron energy will be. The number of electrons which can be accelerated without decreasing the accelerating field significantly was estimated with scaling theories (see next section).

## 1.9 Optimum acceleration conditions and scaling laws

It became apparent in the last sections that analytical expressions of the important quantities for laser wakefield acceleration can be derived in a one-dimensional theory. However, the situation can change significantly when considering the realistic three-dimensional case. Here, it is more difficult to make predictions and thus typically particle-in-cell simulations (see sec. 1.11) have to be used to understand experiments or predict the output for a given parameter set.

However, several groups have worked on the task to derive rather simple scaling laws to calculate the optimum acceleration conditions and the accelerator output for given parameters. Typically, the scaling laws are obtained by consideration of the basic quantities such as the acceleration length and the accelerating field combined with numerical prefac-

tors that are taken from PIC simulations.

Two scaling theories will be presented in the next sections. Both groups found that the acceleration is optimized, if the laser pulse duration  $\tau$  matches the radius of the focal spot  $w_0 \geq c\tau$  and the focus is matched to the plasma density via  $k_p w_0 \approx \sqrt{a_0}$ . The final scaling laws and conclusions, however, differ significantly.

### "Pukhov"-scaling

In 2005, a scaling theory was presented by Pukhov et al. based on similarity theory, which allows to scale experiments with similar parameters [92, 93]. They found the similarity parameter  $S = \frac{n_e}{a_0 n_c}$ , with the assumption of  $S \ll 1$  and  $a_0 \gg 1$ . In this extreme parameter regime, the first electron void of the plasma wave forms a perfect spherical bubble, and all subsequent plasma oscillations are destroyed. They found that the electron acceleration is limited by depletion of the laser pulse. Thus, they predict a high conversion efficiency of  $\eta_{\text{Pukhov}} = 20\%$ . Their predictions of the output parameters of LWFA such as electron energy  $E_{\text{mono}}$  and accelerated charge  $Q$  are

$$\begin{aligned} E_{\text{mono,Pukhov}} &\approx 0.65 m_e c^2 \sqrt{\frac{P}{P_{\text{Rel}}}} \frac{\tau c}{\lambda} \\ Q_{\text{Pukhov}} [nC] &\approx 1.4 \frac{\lambda [\mu\text{m}]}{0.8} \sqrt{\frac{P [\text{TW}]}{100}}. \end{aligned} \quad (1.62)$$

Here,  $P_{\text{Rel}} = 8.5$  GW. Assuming a regular Ti:Sa-system with  $\tau = 30$  fs,  $E_{\text{mono}} \approx 180$  MeV for 20 TW of laser power and  $E_{\text{mono}} \approx 400$  MeV for 100 TW are obtained. It should be noted that these laws are not meant to calculate the electron energy for arbitrary sets of laser and plasma parameters. They rather predict how parameters and output can be scaled once a stable regime for electron acceleration is found.

Current LWFA experiments are rather far away from the derived efficiency of 20%, typically around 1% conversion can be measured if the complete electron spectrum and not just the quasi-monoenergetic peak is taken into account. While simulations often overestimate the obtained charge of LWFA experiments, this discrepancy could also be due to the fact that the numerical prefactors in eqns. (1.62) were obtained from simulations with  $a_0 \geq 10$  and were only tested down to  $a_0 = 4$ , which is difficult to reach for state-of-the-art laser systems.

### "Lu"-scaling

A different scaling theory that is also applicable to lower laser intensities was presented by Lu et al. [94]. Here, a more phenomenological approach based on the basic underlying

processes, i.e., wake excitation, laser pulse evolution / depletion, dephasing, and beamloading is presented. Lu et al. found that  $L_{\text{deph}}$  and  $L_{\text{depl}}$  are matched in their theory, which can be beneficial for the final electron energy spread as already mentioned in sec. 1.8. The maximum energy gain and charge derived by this scaling theory are given as

$$E_{\text{mono,Lu}} \approx m_e c^2 \left( \frac{P}{P_{\text{Rel}}} \right)^{1/3} \left( \frac{n_c}{n_e} \right)^{2/3} \quad (1.63)$$

$$Q_{\text{Lu}} [\text{nC}] \approx 0.4 \frac{\lambda [\mu\text{m}]}{0.8} \sqrt{\frac{P [\text{TW}]}{100}}.$$

For this theory the assumption was that  $a_0 \geq 2$ , which can be reached in the experiment if the appropriate focusing geometry is chosen. Applying the scaling theory, we get about  $E_{\text{mono}} \approx 340$  MeV for 20 TW of laser power and  $E_{\text{mono}} \approx 580$  MeV for 100 TW ( $\lambda = 800$  nm,  $n_e = 5 \cdot 10^{18}$  cm<sup>-3</sup>). Thus, the energies from the two scaling laws are on the same order of magnitude for the parameter range. For higher laser powers which these scaling theories are made for, they will differ drastically. The two scaling laws for the charge in eqns. (1.62) and (1.63) are similar, only the prefactor differs by a factor of 3. In the theory of Pukhov et al. the plasma wave is loaded with more electrons, thus beamloading effects are stronger.

As it will also be shown in the experimental part of this thesis, these scalings have to be applied with great care, since they typically overestimate the output of LWFA, especially concerning the charge. Additionally, it should be mentioned that both scaling theories focus on the self-injection regime of laser wakefield acceleration (although eqns. (1.63) are also valid for externally injected electrons). Recent publications have shown that the often quite unstable output of LWFA experiments using self-injection can be stabilized by employing alternative, more controlled injection methods. This can also reduce the output energy or charge, a trade-off to increase stability or tunability of the accelerator. Also, it has been shown recently that high electron energies can be obtained by increasing the acceleration length via guiding of the laser pulses over several Rayleigh lengths along a discharge that is fired nanoseconds before the arrival of the main pulse [28, 29].

## 1.10 Injection of electrons into wakefields

So far, the considerations of laser wakefields have focused on the attainable fields and the various factors limiting the acceleration process. This section is dedicated to one of the most important aspects and hottest topics in the LWFA community, the process of injection of electrons into the accelerating phase of the plasma wave. The output parameters

are mainly determined by how the acceleration is started, thus a good understanding of the process is crucial. It was shown in sec. 1.7 that the background electrons have to cross the separatrix to be trapped in the plasma wave, which does not happen under normal conditions. Separatrix-crossing in the one-dimensional case can be overcome by longitudinal wave breaking, an effect which can be regarded in analogy to water waves that break if the wave amplitude becomes too large [95]. In the real three-dimensional scenario, this is replaced by transverse wave breaking [96]. However, the threshold for wave breaking is rather high. Several alternative methods were found recently to enable electron injection, which are discussed in the following sections. Up to now, special aspects of these schemes can only be studied in simulations, since current experiments have neither the spatial nor the temporal resolution to study the electron trajectories inside of the plasma.

### 1.10.1 Self-injection via transverse wave breaking

In 2002, it was first shown in simulations that monoenergetic electron bunches can be produced in a laser wakefield accelerator [24]. Initially, electrons were loaded into the wake in the so-called *self-injection scheme*, i.e., only a single laser pulse was used to drive the wakefield and take care of the particle injection in a gas target of uniform density along the laser propagation. This scheme was also used in the proof-of-principle experiments that followed in 2004 [25–27]. Here, transverse wave breaking leads to the self-injection. Different theories have evolved over the past years to describe this mechanism in more detail.

While being initially developed for very high laser intensities ( $a_0 \gg 1$ ) this scheme is now also used to describe experiments at  $a_0 \approx 1 - 2$  qualitatively. As mentioned in the sections before, if an ultra-intense laser pulse is propagating through a plasma, it pushes the electrons out of its path via the ponderomotive force, while the remaining ions are stationary on the relevant timescale of the process (see fig. 1.9). While the laser pulse is propagating forward, the electrons that were pushed to the side are now attracted back on axis due to the positively charged region behind the driving laser pulse. The trajectories of the electrons moving around that region cross after one plasma period enclosing a so-called *bubble* or *blow-out region* [97].

Figure 1.9 shows the electron dynamics. The bubble is enclosed by a dense layer of electrons flowing backwards. This region has a spherical shape for  $a_0 > 2$  with the normalized radius  $R = r_B/(c/\omega_p) = k_p r_B$ , where  $r_B$  is the bubble radius [94, 98–100]. Thus, the electric potential has a maximum in the bubble center and a minimum in the sheath, especially at the back of the bubble, where the electron density is high. Three different types of electron trajectories were identified by Kostyukov et al. depending on their initial distance  $r$  from the laser propagation axis [99]. Electrons close to the center



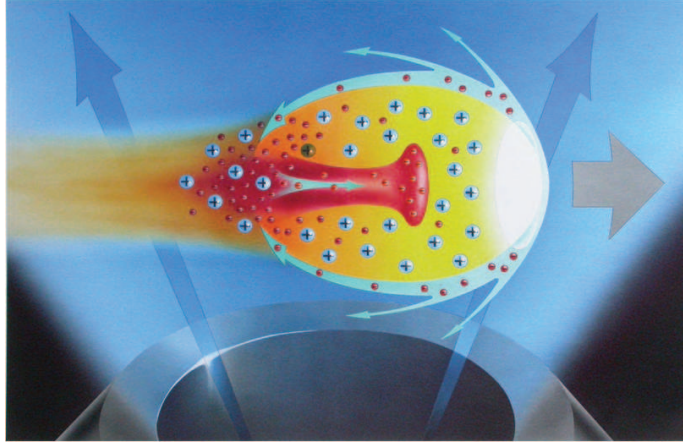


Figure 1.9: **Transverse wave breaking in the "bubble" regime.** The laser pulse (white) propagates (gray arrow) through the gas flowing out of the nozzle (blue arrows). The gas is immediately ionized and the laser expels most of the electrons (red) transversely, while the ions (light blue) stay at their position during the transit of the laser. The electrons move around the bubble (turquoise trajectories) to the point of trajectory crossing, where the electron density is high. Some electrons are injected into the bubble to be accelerated.

( $r < r_B$ ) are being pushed too far away by the laser to play a further role in the process, while electrons with  $r > r_B$  are being attracted by the electric potential of the bubble, but can also not be injected into the bubble. For  $r \approx r_B$  however the electrons flow to the mentioned back of the bubble, where they will also feel the strong electric field pulling them towards the bubble center. Yet, they usually are not injected since their velocity has to exceed the phase velocity of the bubble  $v_p$  to follow the laser. It was shown that some of the electrons can be scattered at the high electron density at the back of the bubble and thus gain enough initial velocity to catch up and stay in the accelerating phase [99]. Electron trapping can occur when the following condition is fulfilled:

$$\frac{\gamma_p}{R} \lesssim \frac{1}{\sqrt{2}}. \quad (1.64)$$

Here,  $\gamma_p \approx \frac{\omega_0}{\omega_p}$  is the phase velocity of the plasma wave. This condition is fulfilled for most current experiments. However, in experiments aiming for the highest electron energies with high intensity, petawatt-class lasers, this can pose a problem. As shown in sec. 1.8, for a large dephasing length, a small plasma density is required, increasing  $\gamma_p$  to a value, where condition (1.64) is no longer fulfilled.

Kalmykov et al. described that for these low densities electrons can still be self-injected [100, 101]. They found that the time  $T_{\text{slip}}$  it takes for the (initially not injected)

electrons with  $r \approx r_B$  to slip past the bubble can be 2 – 5 times longer than expected from the plasma wave phase velocity. During this time, the electrons are exposed to the strong fields at the back of the bubble. If the bubble now expands fast enough to give the electrons more time to be accelerated to  $v_p$ , they can be trapped. This expansion is achieved by strong initial overfocusing of the laser. While the laser pulse evolves to the matched spot size, the bubble will expand accordingly. If the expansion rate is fast enough, electrons can be trapped.

### 1.10.2 Injection at plasma density transitions

One possibility to overcome the above mentioned limitations is to avoid self-injection and control the injection by shaping the longitudinal plasma density profile. The so-called *downramp injection*, described for the first time by Bulanov et al. [33], is similar to the self-injection into the expanding bubble described in the previous section [100]. Here, a longitudinally decreasing plasma density leads to a continuous increase of the plasma wavelength as shown by eq. (1.20). Effectively, this lowers the phase velocity of the back of the bubble and enables electrons to be trapped longitudinally. The local phase velocity can be expressed as

$$\frac{v_p}{c} = 1 - \frac{\xi}{2n_e} \frac{dn_e}{d\xi}, \quad (1.65)$$

where  $\xi$  is the longitudinal-coordinate in the co-moving frame, with  $\xi = 0$  corresponding to the position of the laser pulse and  $\xi < 0$  being a position behind the laser [79]. The efficient trapping of electrons was verified experimentally by Geddes et al. [34], where a low energy electron beam was generated. While a slow downward transition can trap many electrons in the plasma wave, it has two major disadvantages. Firstly, the continuous trapping of electrons leads to a high relative energy spread. Secondly, a decreasing density and increasing plasma wavelength leads to a fast dephasing of the electron bunch, because it reaches the front part of the plasma oscillation after a short propagation distance. Thus, it is not possible to reach high energies in a single stage. However, the electron bunches could be useful for further acceleration in a second stage if the rather low absolute energy spread can be maintained.

Lower absolute energy spread is required for single-stage operation. This can be achieved by using a sharp density transition instead, i.e., a downward jump in plasma density occurring over a length scale shorter than the plasma wavelength  $\lambda_p$  as illustrated in fig. 1.10. Here, the density changes rapidly from  $n_{e,1}$  to  $n_{e,2}$  with  $n_{e,1} = \alpha n_{e,2}$  and  $\alpha \gtrsim 1$ . The relative change in plasma wavelength is calculated to

$$\frac{\Delta\lambda_p}{\lambda_p} = \frac{\lambda_{p,1} - \lambda_{p,2}}{\lambda_{p,1}} = \sqrt{\frac{n_{e,1}}{n_{e,2}}} \approx \frac{1}{2}(\alpha - 1). \quad (1.66)$$

At the same time, the phase velocity of the plasma wave is also modified.

$$\frac{\Delta v_p}{v_p} = \frac{v_{g,2} - v_{g,1}}{v_{g,1}} \approx \left(1 - \frac{n_{e,2}}{2n_c}\right) \left(1 + \frac{n_{e,1}}{2n_c}\right) \approx \frac{n_{e,2}}{2n_c}(\alpha - 1) \quad (1.67)$$

The two equations show that the relative change in plasma wavelength is much greater than the change in phase velocity for the typical underdense plasmas in the experiments. Unlike in the slow downramp case, where the injection is caused by a reduced phase velocity, here the modified plasma wavelength is the deciding factor. The phase velocity of the plasma wave is basically frozen during the rapid increase of  $\lambda_p$  and the wave is instantly loaded with many electrons (fig. 1.10).

While this scheme has been studied extensively theoretically [102–106] experiments so far have not been able to produce monoenergetic electron bunches. Until now, the density transitions have usually been produced by a second laser pulse propagating transversely to the main beam direction, which is depleting the electron density locally [36, 107, 108]. However, this leads not only to a sharp downramp, but modulates the density profile severely, which might be the reason why only broad energy spectra have been obtained up to now. This problem was recently overcome by a different method to produce the downramp, i.e., using shocks in supersonic flows as density transitions, which will be discussed in the experimental part of this thesis [35].

Generally, manipulation of the plasma density profile is another free parameter in the acceleration schemes that can be introduced in a rather simple way. Thus, the injection can be stabilized and the acceleration can also be tuned in contrast to the self-injection process where typically flat-top or Gaussian density profiles are used and the control over the electron beam is limited.

### 1.10.3 Colliding pulse injection

Another way to control electron injection below the threshold for transverse wave breaking is the use of a second laser pulse enabling electron trapping. While first attempts in a perpendicular focusing geometry [37, 109, 110] had limited success, it was shown in 2006 that a scheme employing counterpropagating laser pulses can provide very accurate control over the injected charge and total energy gain [39, 111]. In this scheme, a standing beat wave with half the wavelength of the drive laser is formed between the main driving laser and the second, counterpropagating pulse [38]. This injection pulse typically has a much lower intensity and cannot drive a large amplitude wakefield. Due to the short wavelength,

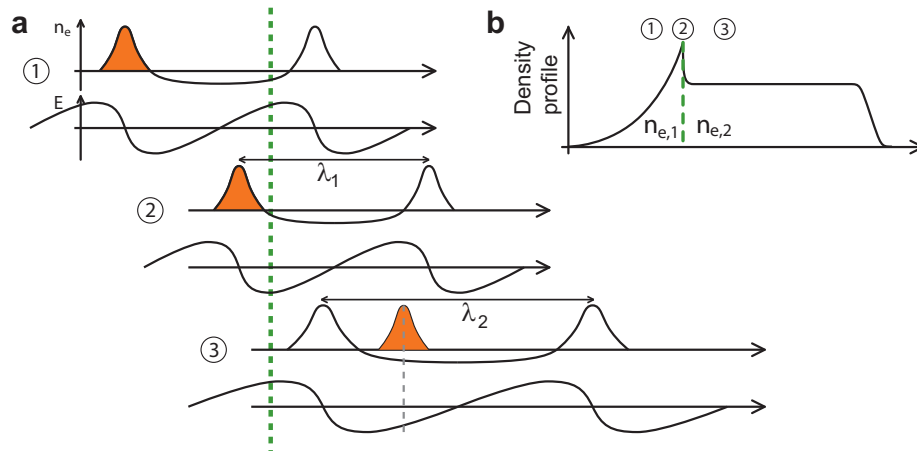


Figure 1.10: **Injection of electrons at a sharp density transition.** Shown are the longitudinal electron density and the electric field for three timeframes while the laser and the trailing plasma wave are traversing the sharp density transition. At the jump, the plasma wavelength is elongated and some of the electrons are injected into the accelerating phase of the plasma wave. The exact position of the injected electron bunch depends on the ratio of the two plasma wavelengths.

the beat wave has a large ponderomotive potential that can pre-accelerate electrons that are then able to catch up with the plasma wave to be accelerated. The number of trapped electrons and the injection position (and thus the electron energy) can be controlled by changing the delay and the amplitude of the injection pulse.

Recently, it was shown by Kotaki et al. [40] that the scheme also works if the beams are not perfectly counterpropagating at  $180^\circ$  but instead at  $135^\circ$ , which greatly reduces the risk of damage to the laser, however the results were not as good as with the counterpropagating geometry.

In 2009, another colliding pulse scheme, the so-called *cold injection* was proposed [41]. Here, instead of giving the electrons an initial kick to catch up with the wakefield, the longitudinal motion of the electron is frozen and the electron can enter the propagating wake. This method has the potential to produce lower energy spread electron bunches, but has not been proven experimentally so far, mainly because of more challenging laser requirements.

#### 1.10.4 Ionization injection

Recently, yet another scheme of electron injection into plasma waves based on the usage of gas mixtures was successfully tested by several groups [42, 43, 112]. A small percentage of a gas with high  $Z$  (here: Nitrogen) is added to the Helium gas target. Due to the higher

ionization intensity threshold (see tab. 1.1), the Nitrogen atoms are not fully ionized before the arrival of the main pulse, but at the highest intensity, and are therefore "born" right inside of the plasma wave and can be trapped. Although electron energies up to 1.5 GeV have been demonstrated recently [30], ionization injection has yet to prove the production of high quality electron beams.

## 1.11 Particle-in-cell simulations (PIC)

Many experimental parameters can be understood and determined by the 1D-equations and the scaling laws described in the last sections. However, a complete understanding of the process is difficult, and many parameters are experimentally not (yet) accessible. Thus, studying laser wakefield acceleration currently heavily depends on simulations. As already mentioned before, so-called *particle-in-cell* (PIC) simulations are used for that purpose.

In contrast to Vlasov codes dealing with an electron density distribution function, PIC codes use discrete macro-particles that are initialized on a grid, typically one macro particle per cell. Depending on the initial density at this position, each macro-particle represents a certain number of electrons, typically  $10^6 - 10^7$ , and thus a specific charge and mass. Most of the time, the plasma is pre-ionized, which reduces computational demands and is a valid assumption, since we have seen in sec. 1.3 that the target gas is ionized completely hundreds of femtoseconds before the peak intensity<sup>3</sup>. The algorithms perform four steps in cycles

**Step 1:** The charge density  $\rho$  and the current density  $\mathbf{j}$  are calculated for each grid point.

**Step 2:** The Maxwell equations are solved with  $\rho$  and  $\mathbf{j}$  from step 1 to obtain the electric and magnetic fields at each grid point.

**Step 3:** The fields are interpolated to each particle position.

**Step 4:** The particles are pushed by the electric and magnetic fields.

Due to the fast increasing computational power, a full three-dimensional particle simulation of a typical electron run can now be completed within one or two days for our parameters. However, it can also take several weeks for large acceleration lengths and longer laser pulses. Fast, two-dimensional simulations can be performed to do shorter parameter

---

<sup>3</sup>This assumption is not valid for ionization injection (sec. 1.10.4). Here, the ionization also has to be computed.

scans, however important effects such as transverse wave breaking can evolve differently in 2D, thus it has to be studied in each case separately, whether 2D is valid.

Several PIC codes have been developed by research groups around the world over the past years. Among others, these are: Virtual-laser-plasma laboratory (VLPL) [113], VORPAL [114], OSIRIS [115], and ILLUMINATION [116]. The latter was used for the simulation data used in this thesis.

Figure 1.11 shows a snapshot of a typical laser wakefield simulation. The laser pulse has already propagated several hundred microns into the plasma and excited a nonlinear plasma wave. In this time frame, electrons have already been injected into the first oscillation (a few electrons can also be seen in the second oscillation) and are now exposed to the strong longitudinal electric field. As seen in fig. 1.11, the accelerated electrons cause a strong azimuthal magnetic field. The visualization of this magnetic field and thus the electron bunch within the plasma is one of the key results presented in this thesis.

PIC simulations are helpful in understanding the underlying physics of laser wakefield acceleration since the experimental access to many important quantities is still limited. Naturally, the simulations are more accurate the smaller the individual cell size (i.e., fewer particles per macroparticle) and the larger the total simulation box, however the chosen parameters are always a trade-off between resolution and available computational power. One particular problem is the underestimation of Coulomb explosion forces because electrons within one macroparticle cannot interact with each other. Additionally, while PIC simulations often show good agreement with the experiment in the electron energy spectrum, the charge is typically overestimated by an order of magnitude.

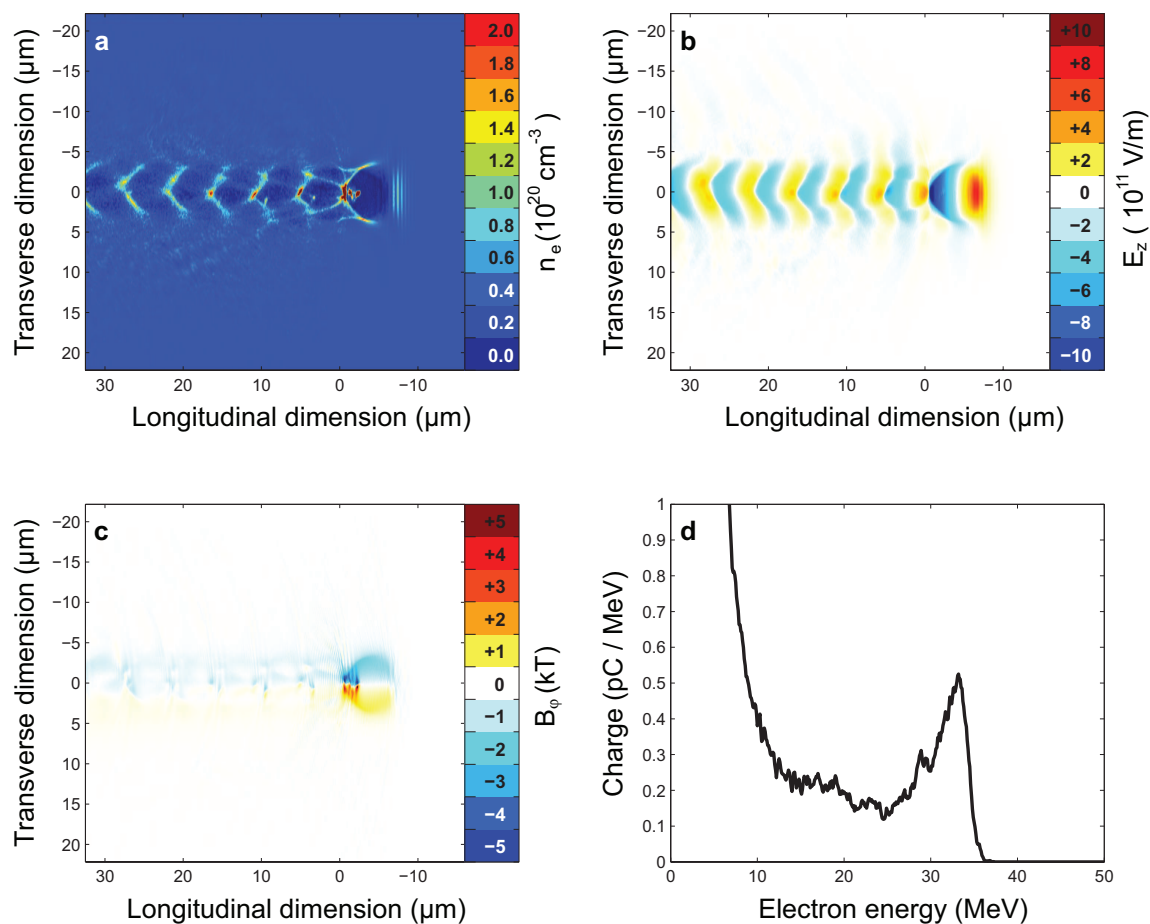


Figure 1.11: **Particle-in-cell simulation at one frame during the interaction.** The laser pulse is propagating from left to right. The complete box has an extension of  $48.5 \mu\text{m}$  longitudinally and  $48.5 \mu\text{m}$  transversally. **a**, Electron density. Some electrons are injected into the first plasma oscillation. Electron bunches with much lower charge are also seen in the second and third plasma oscillation. **b**, Longitudinal electric field, which is co-propagating with the laser pulse and is used to accelerate the electrons to relativistic energies. **c**, Azimuthal magnetic field of the accelerated electron bunch, which is used to detect the electron bunch via the Faraday effect within the plasma (see chapter 4). **d**, Electron energy spectrum. A large number of low energy electrons is visible. These electrons are typically not detected because of a much larger divergence compared to the high energy peak. Thus, only few of these electrons reach the electron spectrometer.





# Chapter 2

## Basic experimental setup

In this chapter, the basic experimental setup for the laser wakefield acceleration experiments is described. In general, three main components are required: a high-intensity, ultra-short laser pulse, a gas target to generate the plasma, and a detection system for the accelerated electrons.

For the results presented in this thesis, the high-intensity laser pulses were either delivered by the Light Wave Synthesizer 20 (LWS-20) or the Advanced Titanium-Sapphire Laser (ATLAS). The two lasers have different pulse duration and energies, thus opening up two separate parameter regimes for the experiments. Both systems are described in more detail in sec. 2.1. The laser pulses are focused into Helium gas, where they ionize the atoms, excite plasma waves, and accelerate electrons as described in the theory about LWFA in the previous chapter. Here, supersonic gas jets with exit diameters between  $150\ \mu\text{m}$  and  $3\ \text{mm}$  were used. Section 2.2 gives details about the exact properties and the characterization of these targets. Finally, the different electron detection systems, such as the electron spectrometer or the integrating current transformer (ICT) are described in sec. 2.3. An overview of the complete setup is shown in fig. 2.1.

### 2.1 Laser systems

#### 2.1.1 Light Wave Synthesizer 20 (LWS-20)

Most experiments presented in this thesis were performed with the LWS-20 laser system, producing down to  $7.7\ \text{fs}$  light pulses with peak powers up to  $16\ \text{TW}$  at a carrier wavelength of  $800\ \text{nm}$  and  $10\ \text{Hz}$  repetition rate by a conventional Ti:sapphire front end in combination with two non-collinear optical parametric chirped pulse amplification (NOPCPA) [17, 117] stages. A layout of the laser system is shown in fig. 2.2. LWS-20 is currently the most

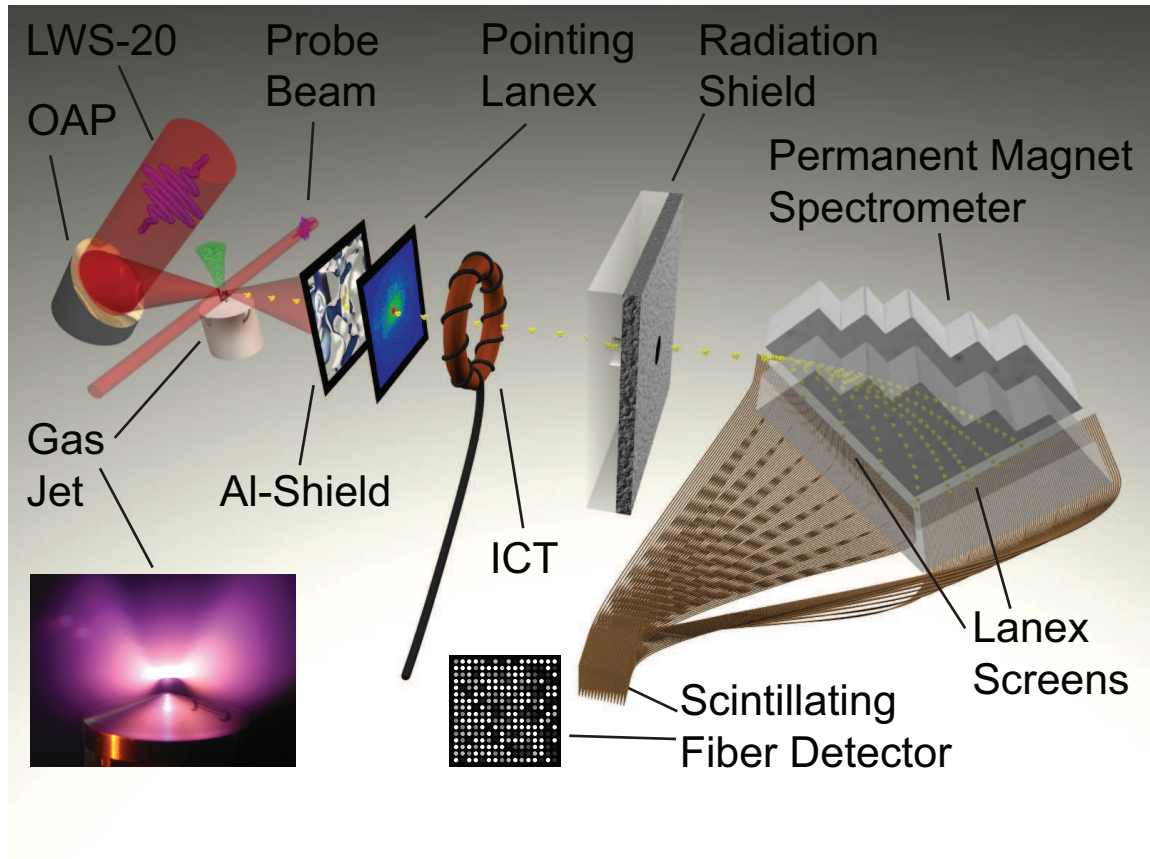


Figure 2.1: **Basic experimental setup for LWFA experiments.** The 8 fs-pulses of LWS-20 (or the 26 fs-pulses of ATLAS) are focused via an off-axis parabolic mirror (OAP) onto a supersonic He jet to accelerate the electrons. Behind the target, the laser light is blocked with a  $10\ \mu\text{m}$  Al foil, while the electrons propagate through the foil towards the electron spectrometer. In between, their profile is measured with an optional scintillating screen and the bunch charge is measured with an integrating current transformer (ICT). The electrons are dispersed by the permanent dipole magnet to measure the energy spectrum. Here, the electrons are detected by absolutely calibrated scintillating screens as well as an array of scintillating fibers that are directed onto a cooled 16-bit CCD camera to reach a high dynamic range.

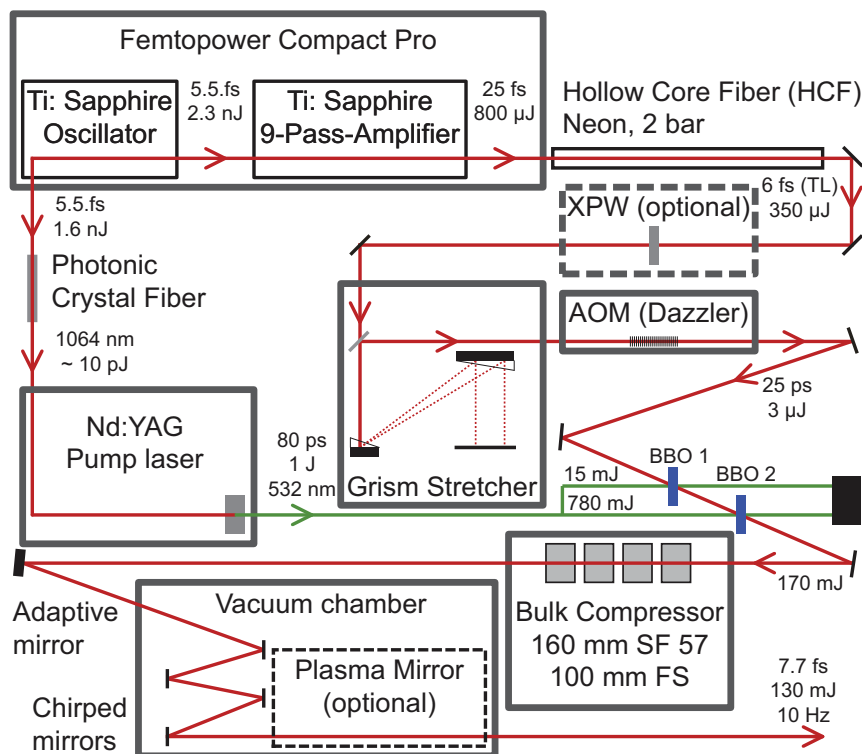


Figure 2.2: **Layout of Light Wave Synthesizer 20.**

intense few-cycle laser system worldwide [118, 119].

The commercial front end (Femtopower Compact Pro, Femtolasers GmbH) of LWS-20 starts with a Rainbow oscillator, producing 5-6 fs pulses at the nJ-level at a repetition rate of 80 MHz. A beamsplitter separates the oscillator output pulses into two parts. About 2/3 of the pulse energy is amplified in a 1 kHz, 9-pass Ti:sapphire amplifier and afterwards compressed to 25 fs. These kHz pulses are then broadened via self-phase modulation in a Ne-filled hollow core fiber (fig. 2.3a) [120]. Subsequently, the pulses are stretched to 30 ps in a negative-dispersion stretcher that consists of a combination of gratings and prisms (GRISM) and pass through an acousto-optical modulator (DAZZLER, Fastlite) that is used for fine-tuning the dispersion. An optional cross-polarized wave generation (XPW) stage to improve the laser pulse contrast is placed between the stages for spectral broadening and temporal stretching. Although this pulse cleaning stage has proven to show a significant improvement of the laser output parameters, it has not been used for

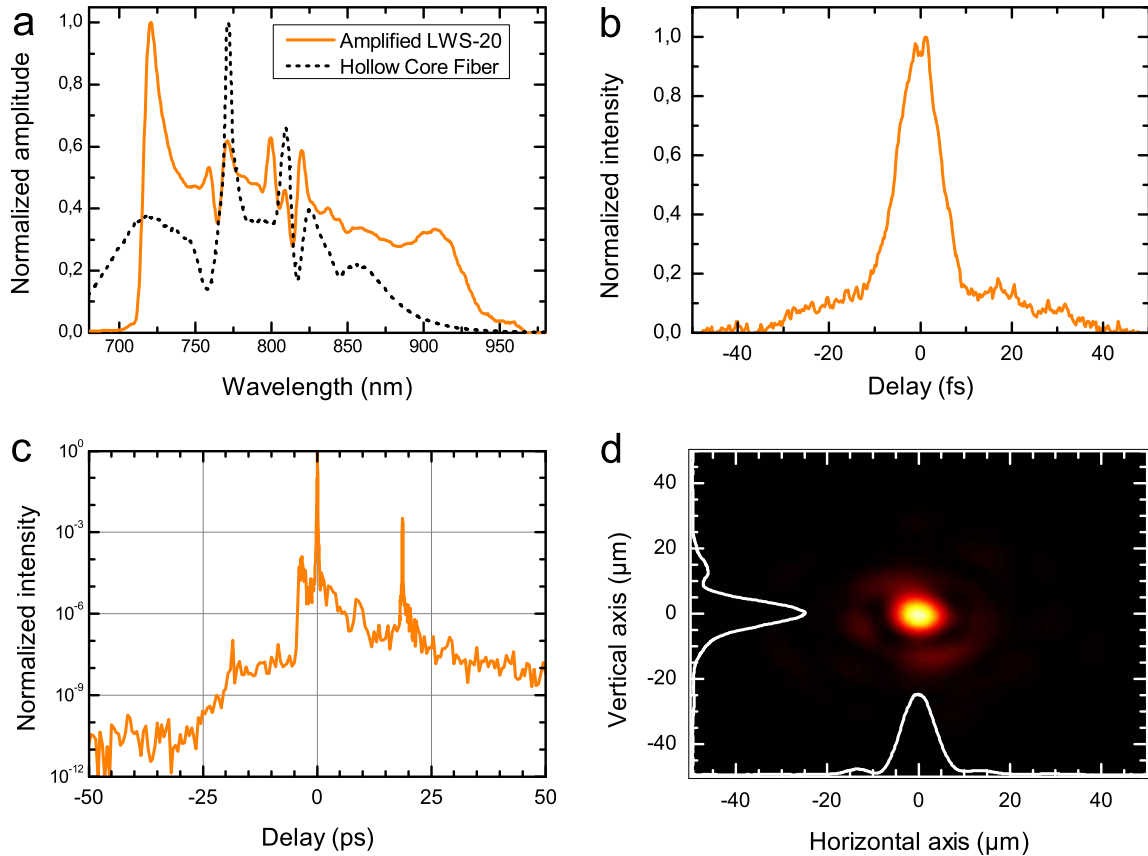


Figure 2.3: **Output parameters of LWS-20.** **a**, Broadened output of the hollow core fiber and amplified spectrum. **b**, Single-shot autocorrelation trace of the compressed output pulses. **c**, Laser pulse contrast measured with a third-order autocorrelator. **d**, Focus with  $8.3 \mu\text{m} \times 8.6 \mu\text{m}$  FWHM obtained with a 312 mm focal length off-axis parabola after optimization with the adaptive mirror.

LWFA but only for surface harmonics experiments so far due to increased complexity of the system. More details about the technique and the results can be found in the appendix.

The non-amplified part of the oscillator pulses (1/3 in energy) is used to optically synchronize the stretched seed pulses with the pump laser for the OPCPA stages. To this end, the remaining oscillator output is focused into a photonic crystal fiber (Thorlabs GmbH) where a soliton at 1064 nm central wavelength at the 10 pJ level is generated to act as a seed for a commercial flash-lamp pumped Nd:YAG laser (EKSPLA), which amplifies these seed pulses at 10 Hz repetition rate. Finally, the pump laser delivers pulses with 2 J energy at 1064 nm that are frequency doubled to 1 J at 532 nm in a DKDP crystal. These pump pulses are now optically synchronized to the stretched seed pulses with a

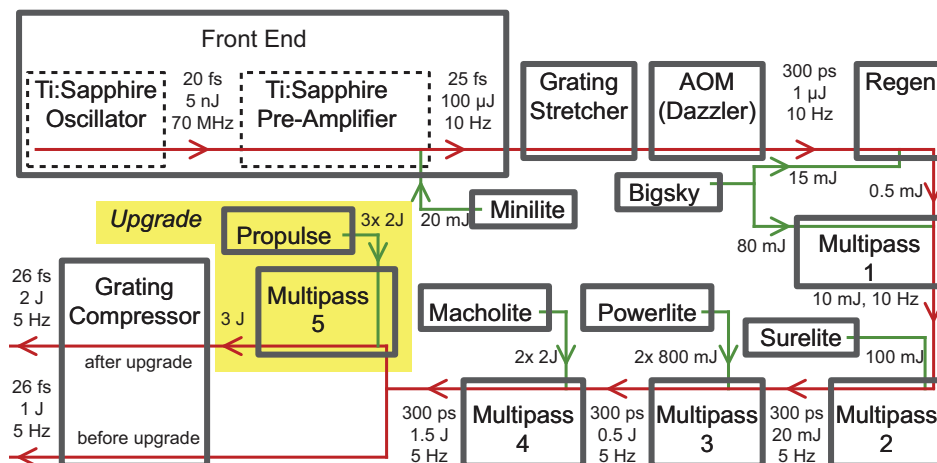


Figure 2.4: Layout of the ATLAS laser system.

timing jitter of  $< 1$  ps. The pump and seed pulses are spatially and temporally overlapped in two NOPCPA stages to amplify the seed to the  $> 100$  mJ level in a spectral range of 700 - 980 nm (see spectra in fig. 2.3a). Due to the negative dispersion stretcher, the pulses can now be compressed via positive dispersion in a combination of bulk glasses and multilayer (chirped) mirrors. The final compression down to 8 fs (fig. 2.3b) with the chirped mirrors is done in vacuum to reduce nonlinear effects in air or in the window of the vacuum chamber.

The contrast of the compressed pulses is shown in fig. 2.3c. For further contrast improvement, the compressed pulses can be optionally reflected from a so-called *Plasma Mirror* [121], which is also installed in the compressor chamber. An adaptive mirror (AM) in closed loop operation allows to correct for wavefront aberrations. The laser beam is sent through a vacuum beam transport line to the experimental chamber where it is focused with an off-axis parabolic mirror to spot sizes on the order of  $10 \mu\text{m}$  depending on the focal length. The focus quality can be optimized further by compensating the additional aberrations from the vacuum transport and the focusing optics via a genetic algorithm modifying the AM surface. Thus, foci with  $\sim 25\%$  of the energy contained in the FWHM, which is 50 % of what would be measured with a perfect Gaussian beam, and intensities up to  $10^{19} \text{ W/cm}^2$  are achieved (fig. 2.3d).

### 2.1.2 Advanced Titanium-Sapphire Laser (ATLAS)

A layout of ATLAS, the second laser used for the LWFA experiments, is shown in fig. 2.4. It starts with a Ti:sapphire oscillator and multipass, producing pulses on the 100  $\mu\text{J}$ -level with 10 Hz. Instead of spectral broadening by self-phase modulation as in LWS-20, the pulses are stretched to 300 ps in a grating-based stretcher after the multipass amplifier. Subsequently, they are further amplified in a regenerative amplifier (regen) and another four flash-lamp-pumped multipass amplifiers to 1.5 J. To reduce gain narrowing of the amplified spectrum which would lead to longer output pulses, an acousto-optical modulator (MAZZLER, Fastlite) is placed in the regen to flatten the spectrum. Thus, a spectral width of 80 nm FWHM after the regen amplifier and 60 nm FWHM after the final multipass is obtained. After passing through the compressor, pulses with 26 fs FWHM duration, 1 J energy at 5 Hz repetition rate are generated. The typical on-target energy during the performed experiments after losses of the vacuum beamline was 770 mJ. During the experimental campaign, a fifth multipass amplifier was also used to double the uncompressed energy (see yellow box in fig. 2.4). Due to increased compression and beamline losses, the on-target energy was about 1.2 J.

## 2.2 Gas targets

### 2.2.1 Subsonic and supersonic nozzles

Pulsed gas nozzles with an opening time on the order of a millisecond are used as targets for the LWFA experiments to reduce the gas load in the vacuum chamber. The shape of the nozzle, i.e., the evolution of the diameter from the valve to the nozzle exit determines the radial gas profile behind the nozzle exit. While cylindrically shaped nozzles with subsonic flow produce Gaussian-like density distributions, flat-top profiles that are sometimes preferred experimentally are generated by supersonic nozzles with the De Laval design. Here, the diameter of the nozzle is first decreasing after the valve, accelerating the gas to the speed of sound  $v_s$ . Then, the diameter is increasing again, which is cooling the gas and decreasing  $v_s$ , and thus increasing the Mach number  $M_1 = v/v_s$ . Thus, profiles with rather sharp edges are achieved. After propagation of 2-3 nozzle exit diameters, the profiles smoothen to a Gaussian-like shape (fig. 2.7).

The gas speed  $v$  and the Mach number  $M_1$  are determined by the ratio  $R$  between the exit diameter and the waist inside of the nozzle. All the nozzles used for the experiments in this thesis have a ratio of  $R = 3$ , an opening angle of  $7^\circ$ , and a Mach number of about  $M_1 \approx 5$ . More details about the nozzle production and simulations of the gas flow are described in Schmid [122].

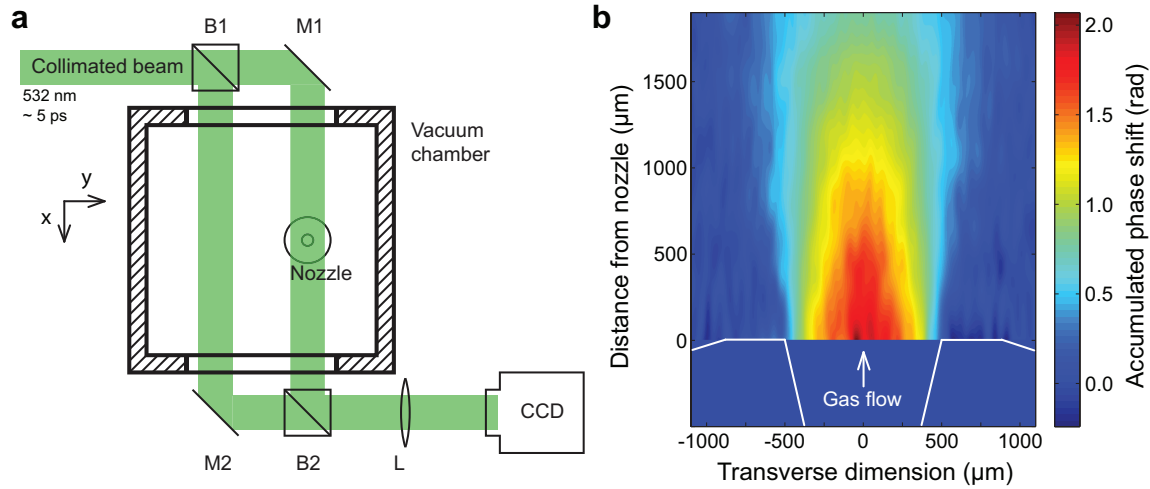


Figure 2.5: **Gas jet interferometry.** **a**, Setup of the Mach-Zehnder interferometer. The collimated laser beam is split by beamsplitter B1 and sent through the vacuum chamber, where the right arm acquires a phase shift corresponding to the gas density. Afterwards, the two beams are combined again by B2 and the interaction region is imaged to a CCD camera by lens L. **b**, Sample phase shift measured for a 1 mm supersonic nozzle with a backing pressure of 14 bar.

### 2.2.2 Gas flow characterization

The gas flow from the supersonic nozzles is characterized in a Mach-Zehnder interferometer (fig. 2.5a). The index of refraction  $n$  and the gas density  $\rho$  are connected by the Gladstone-Dale relationship

$$n - 1 = K\rho, \quad (2.1)$$

where  $K$  is a constant for each gas, which can be calculated with a known value pair of  $n$  and  $\rho$ . Thus, by measuring the accumulated phase shift  $F(y)$  (fig. 2.5b) of a laser beam passing through the gas jet with respect to a reference beam, the gas density is obtained. This phase shift is an integration of the radial profile of the refractive index  $f(r) = n(r) - 1$  along a straight path through the gas. Although all of the LWFA experiments were performed in Helium, Argon is used for the interferometric measurements because it produces the same density distribution as Helium, but has a larger refractive index and thus produces a larger phase shift in the interferogram

$$F(y) = k \int_{-\infty}^{\infty} f(\sqrt{x^2 + y^2}) dx = k \int_y^{\infty} \frac{2f(r)r}{\sqrt{r^2 - y^2}} dr \quad (2.2)$$

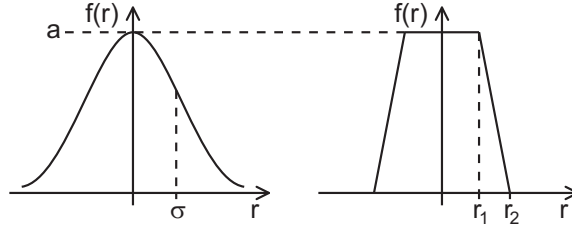


Figure 2.6: **Gaussian and trapezoidal fit functions as given by eq. (2.4).**

with  $k = 2\pi/\lambda$ . The initial radial profile can be obtained from the measurement of  $F(y)$  via Abel inversion assuming radial symmetry.

$$f(r) = -\frac{1}{\pi} \int_r^\infty \frac{dF(y)}{dy} \frac{1}{\sqrt{y^2 - r^2}} dy \quad (2.3)$$

The Abel inversion is performed via the free software IDEA (TU Graz) [123]. However, the Abel inversion is a function of the derivative of the measured phase shift  $F(y)$ . Thus, very clean data with low noise is required for a reliable retrieval. For non-perfect data, the Abel inversion often shows retrieval artefacts, such as peaks at the edge of a plateau region. Additionally, Abel inversion of long arrays requires a significant amount of computational time, making it cumbersome to evaluate many phase lineouts.

Thus, an algorithm has been developed to evaluate the acquired phase shift images not by Abel inversion, but a fitting routine of assumed profiles instead. Abel inversion of selected lineouts have shown that the density profile has the shape of a trapezoid close to the nozzle exit, while it evolves into Gaussian shape for distances larger than 2-3 nozzle exit diameters. The two profiles are expressed with the following functions (see. fig. 2.6):

$$f_{\text{Gauss}}(r) = a e^{-\frac{r^2}{2\sigma^2}}$$

$$f_{\text{Trap}}(r) = \begin{cases} a & \text{for } r \leq r_1 \\ a \frac{r-r_2}{r_1-r_2} & \text{for } r_1 < r \leq r_2 \\ 0 & \text{for } r > r_2. \end{cases} \quad (2.4)$$

Both fit functions  $f(r)$  are integrated analytically with eq. (2.2) to simulate the total phase shift  $F(y)$  measured in the interferometer.



$$F_{\text{Gauss}}(y) = 2ak\sigma \sqrt{\frac{\pi}{2}} \cdot e^{-\frac{y^2}{2\sigma^2}}$$

$$F_{\text{Trap}}(y) = ak \begin{cases} 2x_1 + \frac{1}{\Delta r} \left[ y^2 \log\left(\frac{r_2+x_2}{r_1+x_1}\right) - r_2x_2 - r_1x_1 + 2r_2x_1 \right] & \text{for } |y| \leq r_1 \\ \frac{1}{\Delta r} \left[ y^2 \log\left(\frac{r_2+x_2}{|y|}\right) - r_2x_2 \right] & \text{for } r_1 < |y| \leq r_2 \\ 0 & \text{for } |y| > r_2 \end{cases} \quad (2.5)$$

Here,  $\Delta r = r_1 - r_2$  and  $x_{1,2} = \sqrt{r_{1,2}^2 - y^2}$ . The above equations are used to fit each horizontal line of the interferogram directly after conversion of the scale from  $\mu\text{m}$  to pixel. The refractive index profile is obtained with the fit parameters and the wavelength of the interferometer laser  $\lambda = 532 \text{ nm}$ . Thus, the maximum electron density  $n_{e,\text{max}}$  for a fit profile is calculated with eq. (2.1) to

$$n_{e,\text{max}} = \frac{2a}{K}. \quad (2.6)$$

The above equation has already been adapted for Helium gas used in the LWFA experiments. Since every He atom has two electrons, the electron density of the ionized He plasma will be twice the gas density measured with Ar in the interferometric setup.

This evaluation method is applied to the complete phase image (fig. 2.5b) to calculate the gas profile of each nozzle used in the experiment. Four sample lineouts at different distances to the nozzle exit fitted with both functions are shown in fig. 2.7. For the two lineouts at smaller heights (top row), the trapezoidal fit nicely reproduces the density profiles obtained via Abel inversion. In fact, the fitted profile is most likely more accurate than the Abel inverted one with its strong, unphysical oscillations. For lineouts that are more than two nozzle exit diameters away from the nozzle, the Gaussian fit gives a more realistic picture (bottom row).

### 2.2.3 Shocks in supersonic flows

Additionally to the flat top density profile in the proximity of the nozzle, supersonic flows have another advantage compared to subsonic flows, because they offer a simple way of producing sharp density transitions, which can be used for electron injection into the wakefield (see sec. 1.10). If an obstacle (here: razorblade) is inserted into the flow, the gas has to adapt locally to this distortion because information cannot flow upstream in the supersonic flow (fig. 2.8a). Thus, a shockfront is formed that is propagating through the gas flow at a certain angle  $\alpha$  (see also the detailed description in Schmid [122]). The shock has a higher density than the surrounding gas and very sharp edges, usually on the order

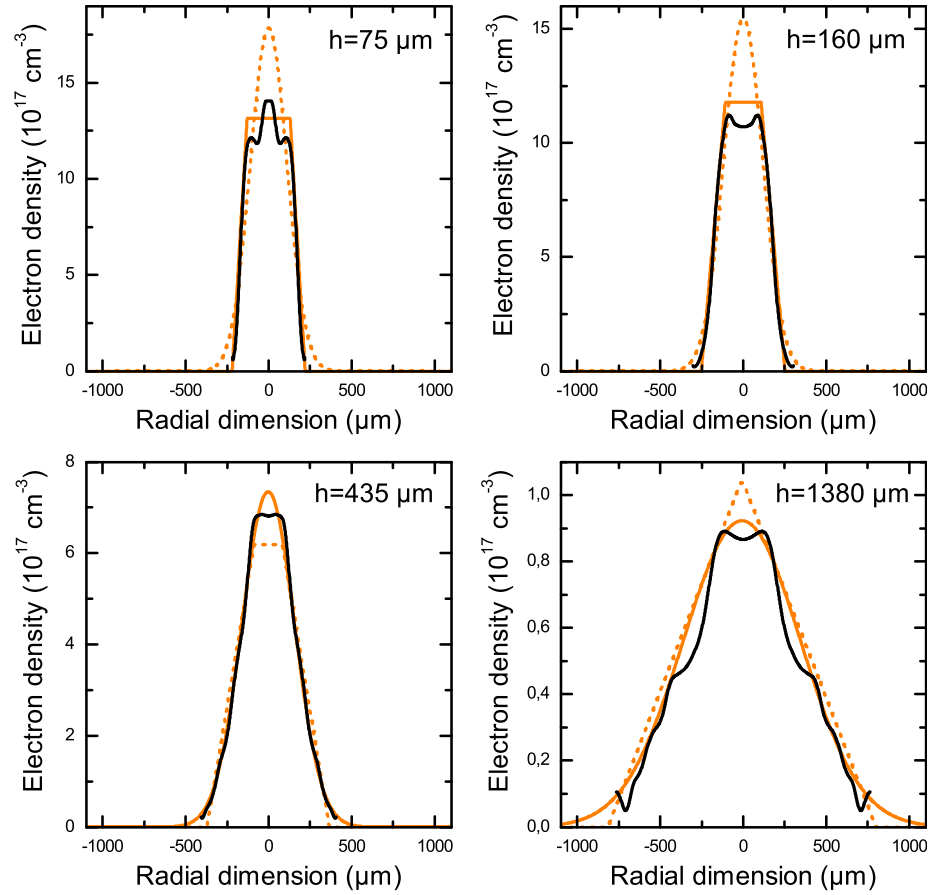


Figure 2.7: **Comparison of fitting routine and Abel inversion.** Shown are four electron density profiles at different heights  $h$  above the nozzle exit for a  $300 \mu\text{m}$  supersonic nozzle. The black curves show the retrieved profile by Abel inversion with the Backus-Gilbert method, the orange lines show the two fit curves. The transition from the trapezoidal profile close to the nozzle to a Gaussian profile further away is visible.

of the mean free path of the gas, which is about 500 nm for Helium at the used densities [124, 125]. Thus, the edge of the shock is the desired sharp density transition.

The ratio of the gas densities before and after the shock is determined by the specific heat ratio  $\kappa$  ( $\kappa = 5/3$  for a monoatomic gas), and the Mach number of the flow  $M_1$  [126].

$$\frac{n_1}{n_2} = 1 - \frac{2}{\kappa + 1} \left( 1 - \frac{1}{(M_1 \sin \alpha)^2} \right) \quad (2.7)$$

$n_1$  and  $n_2$  are the gas densities before and after the shock, respectively. For weak distortions propagating at the minimum angle, i.e., the Mach angle  $\alpha_M = \arcsin(1/M_1)$ , it follows  $n_1 = n_2$ , while the relation has a minimum for a perpendicular shock ( $\alpha = 90^\circ$ ).

Supersonic flows with shocks cannot be characterized with the Mach-Zehnder interferometer as described in the last section, because they are no longer cylindrically symmetric. Thus, the gas profiles are characterized in the undisturbed flow and the density ratio is calculated with eq. (2.7). The precise density profile can also be evaluated during the LWFA experiments as shown in Schmid et al. [35]. Since the variations of the refractive index in the ionized gas of the plasma channel is much larger than the surrounding non-ionized gas (see also sec. 1.5), a cylindrical symmetry not about the nozzle axis, but the propagation direction along the ionizing laser can be assumed, yielding the shockfront profile depicted in fig. 2.8b. Here, a transition of  $5 \mu\text{m}$  is measured, which is due to the limited resolution of the measurement. The real transition is expected to be around  $1 \mu\text{m}$ , which is significantly shorter than the plasma wavelength in the typical experiments ( $\lambda_p \approx 5 - 30 \mu\text{m}$ ).

## 2.3 Electron detection

The third component of a LWFA experiment is the electron detection system (fig. 2.1). Several methods used in conventional accelerators have been adopted to fit the needs of this new type of accelerators. Since up to now the output of LWFA has still fluctuated significantly from shot to shot, single-shot detection schemes are crucial. Additionally, the diagnostics have to be able to measure a wide parameter range both in energy (few MeV to 100s of MeV) and charge ( $< 1 \text{ pC}$  to nCs). The different detection schemes are described in the next section.

### 2.3.1 Energy-independent charge measurements

Two established devices for energy-independent single-shot charge measurements are the so-called Faraday Cup [127] or the Integrating Current Transformer (ICT). However, both technologies have significant disadvantages for LWFA. Faraday Cups measure the beam

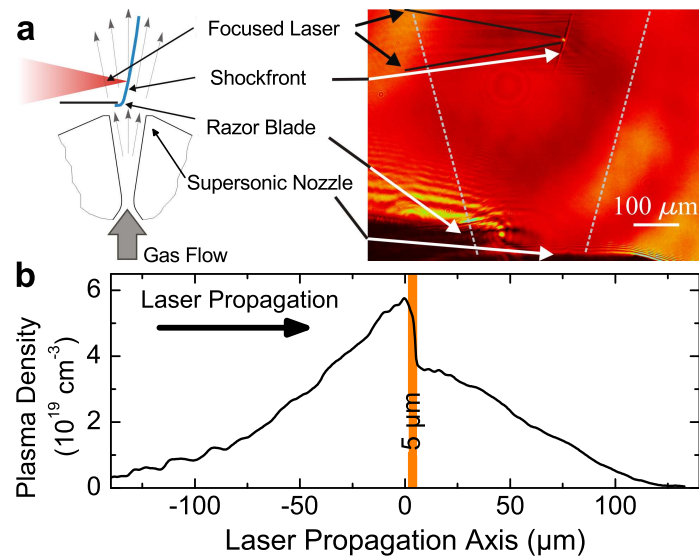


Figure 2.8: **Generation of a shockfront in a supersonic flow.** **a**, Sketch and sideview image of the supersonic flow disrupted by the inserted razor blade. A shockfront with a sharp density gradient evolves, which is used to inject the electrons into the wakefield. **b**, Sample measurement of the longitudinal density profile with a Nomarskii interferometer [35]. A sharp density transition of only a few micron width with a ratio of 3:2 is observed.

charge by blocking the beam, thus the electron beam cannot be used elsewhere simultaneously. ICTs do not interrupt the beam, but measuring charges below 10 pC is difficult because of electronic noise, especially in LWFA experiments where the electro-magnetic pulse generated during the laser-plasma interaction disturbs electronics that are close to the interaction region. Additionally, in LWFA, where the dark current of few MeV electrons often contains an order of magnitude more charge than the short electron bunch at higher energies, energy independent measurements are not sufficient for a good electron beam characterization and are only useful for additional diagnostic purposes.

### 2.3.2 Electron energy spectrometer

Electron energy spectrometers are able to overcome this limitation, because here the electrons are dispersed energy dependently by a dipole magnet before they are detected [44, 128–133]. The LWFA spectrometer in our experiments uses a large permanent magnet and is capable of detecting electrons in a bandwidth of 2 – 400 MeV in a single shot (see fig. 2.9). The electrons enter the magnet at the apex and are bent downwards to the floor. The spectrometer has a 5 cm gap with a magnetic field of 1 T. The exact magnetic field map has been measured with a hall probe to simulate the electron trajectories for different energies. Electrons below 70 MeV are bent by 90° and are imaged to the first detection plane. For energies higher than 70 MeV, the electrons exit through the second detection plane and are slightly defocused in the energy axis. In both planes, the beam is defocused slightly transversally (see Sears et al. [44] for a more detailed description).

Large-area position-sensitive electron detectors are necessary to detect the electrons at the exit planes, which can extend over several hundred cm<sup>2</sup>. Suitable candidates are scintillating materials (fibers or screens) or imaging plates (IP) [129, 132, 134]. IPs have an active layer of tiny crystals ( $\sim 5 \mu\text{m}$ ) that can store high energy radiation. The IPs have to be removed from the vacuum chamber and have to be scanned after exposure to the electron beam to gather the data, thus they are impractical for high repetition rate experiments. Additionally, the charge calibration is difficult and strongly depends on the selected hardware [134].

Scintillator-based detection schemes are more reliable and offer faster read out. Two different systems are installed at the current experiment. The first system is an array of 256 bundles of 3 scintillating fibres with 1 mm diameter each (Saint Gobain Crystals BCF-60, Nemours Cedex, France) [128]. The fiber bundles are separated by 3.5 mm along the detection plane. The fibers are connected to a cooled, 16bit CCD camera (Roper Scientific, Ottobrunn, Germany) via a 2:1 taper. Black acrylic cladding avoids fiber crosstalk. Additionally, the cladding circumvents the coupling of stray laser light into the fiber. Thus, this detection scheme has a very low noise and can detect already electron bunches around

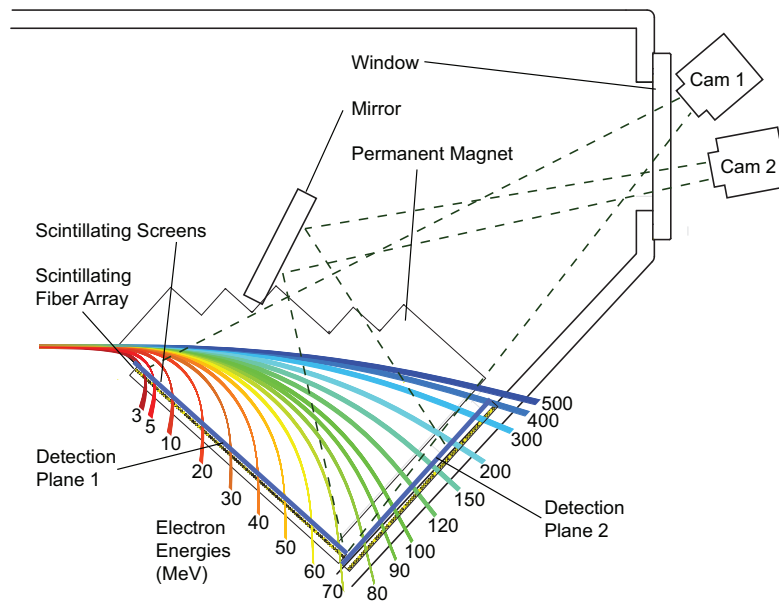


Figure 2.9: **Electron energy spectrometer.** The electrons are deflected energy dependently (coloured lines) by the permanent dipole magnet and are detected with an array of scintillating fibers and two scintillating screens at the two exit planes of the magnet. The scintillating screens are imaged to two CCD cameras that are located outside of the vacuum chamber. In the current setup, electrons up to  $\sim 180$  MeV are detected by the cameras.

1 fC. However, the resolution in the energy spectrum is limited to  $\approx 1$  MeV due to the large spacing of the fibers. The lack of transverse profile information and the saturation threshold of the camera are two other disadvantages of the fiber detector.

Therefore, the exit planes are also covered with powdered phosphor screens that lie on top of the fibers. The light emitting surfaces of the scintillating screens are imaged to two CCD cameras (Grasshopper and SCOR-20SOM-CS, PointGrey, Richmond, BC, Canada). In this setup, the energy resolution is about ten times higher compared to the fiber diagnostic and also information about the transverse electron beam profile can be obtained. However, stray laser light has to be shielded, because the scintillating signal is weak. Therefore, the back part of the vacuum chamber with the spectrometer is carefully blocked from the interaction region of laser and gas jet. To shield the laser light, the electrons pass through a thin Al foil of only  $10 \mu\text{m}$  thickness so that the divergence is not increased significantly.

### 2.3.3 Absolute charge calibration of scintillating screens

Different types of green emitting ( $\approx 545$  nm) scintillating screens are used in typical LWFA experiments. All of the screens use P43 ( $\text{Gd}_2\text{O}_2\text{S}$ ) as phosphor, only the thickness of the scintillating layer is different. The exact composition of the KODAK Lanex Fine screen can be found in Glinec et al. [130]. Eight different screens were chosen (see tab. 2.1) for calibration at the ELBE linear accelerator in Dresden to measure the absolute response and confirm the linear behaviour of the screens. ELBE delivers pulse trains of variable length at a 1 kHz repetition rate with a micropulse repetition rate of 13 MHz. The electron bunches have a maximum energy of 40 MeV, tunable charge up to 80 pC, and a pulse duration of 2 ps. The energy deposited by an electron in the scintillating screen is constant for relativistic energies [130], thus this calibration can be applied for the complete spectral range of current LWFA experiments. The calibration setup is shown in fig. 2.10a.

For all screens, the charge  $Q$  was varied over four orders of magnitude while the scintillation signal was recorded (fig. 2.9b). For  $Q > 50$  pC, pulse trains with several micropulses were used. The micropulse spacing is much shorter than the decay time of the scintillator ( $\approx 1$  ms), thus they can be regarded as a single pulse with higher charge. The absolute calibration was obtained by calculating the collection solid angle and transmission of the imaging system as well as the quantum efficiency of the CCD camera (see Buck et al. [56] and fig. 2.11a for details).

The calibration results are shown in fig. 2.12, where the absolute signal recorded from the scintillator vs. applied charge  $Q$ , which was measured with the ICT. By evaluation of the shape of the signal on the scintillator (fig. 2.10b+c), the applied peak charge density  $\rho_{\text{real}}$  on the scintillator is calculated (also plotted in fig. 2.12), which is important to look for saturation effects as also described on the next pages. It is apparent that all screens

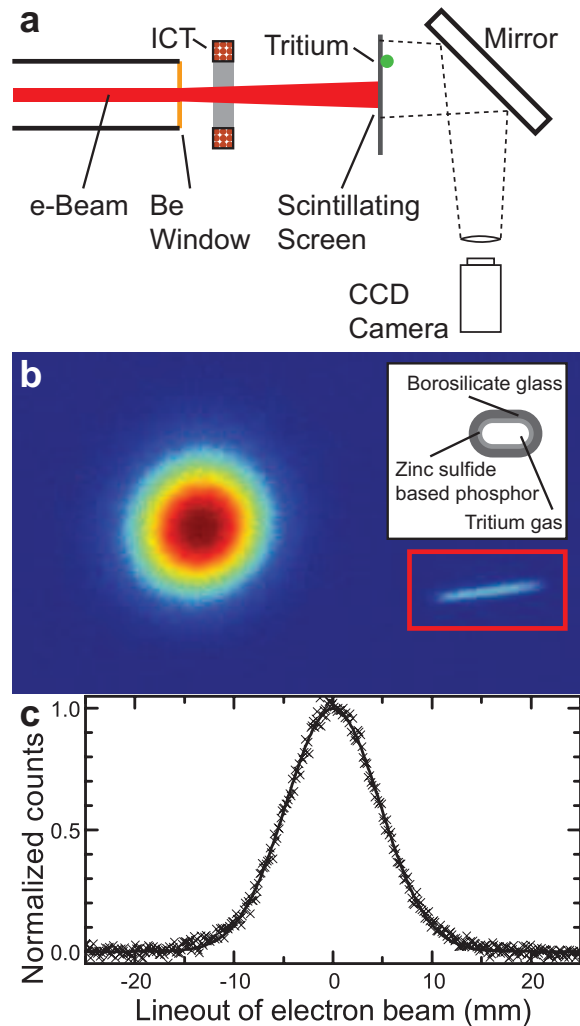


Figure 2.10: **Setup for the calibration of the scintillating screens.** **a**, Setup at ELBE accelerator. The electrons exit the accelerator vacuum through a Beryllium window and hit the scintillating screen at 0.38 m distance. A constant light source (CLS) is placed on the scintillating screen for cross-calibration. The scintillation signal and the CLS are imaged onto a CCD camera. The bunch charge is measured between accelerator and screen with an ICT. **b**, Typical CCD image of electron bunch and CLS (red box). Inset: Cross-section of the Tritium tube. **c**, Lineout of the electron beam in **b**) (crosses) with Gaussian fit (solid line).



Screen	Abs. calibration ( $10^9$ phot./sr/pC)	$N_{\text{scint}}/N_{\text{CLS}, 20 \text{ ms}}/Q$ ( $\text{pC}^{-1}$ )	$\rho_{\text{sat}}$ ( $\text{pC}/\text{mm}^2$ )
KODAK Biomax MS	$14.8 \pm 1.3$	$5.79 \pm 0.26$	$21.8 \pm 5.0$
CAWO OG 16	$12.4 \pm 1.1$	$4.86 \pm 0.21$	$32.9 \pm 6.6$
KODAK Biomax Transcreen HE	$7.85 \pm 0.67$	$3.02 \pm 0.13$	$47 \pm 10$
KODAK Lanex Regular	$6.95 \pm 0.60$	$2.72 \pm 0.12$	$66 \pm 33$
KONICA KR	$6.58 \pm 0.56$	$2.58 \pm 0.11$	$> 100$
KODAK Biomax Transcreen LE	$1.79 \pm 0.15$	$0.700 \pm 0.031$	$> 100$
KODAK Lanex Fine	$1.75 \pm 0.15$	$0.686 \pm 0.030$	$> 100$
KONICA KF	$1.54 \pm 0.13$	$0.602 \pm 0.027$	$> 100$

Table 2.1: Absolute calibration of scintillating screens and onset of saturation.

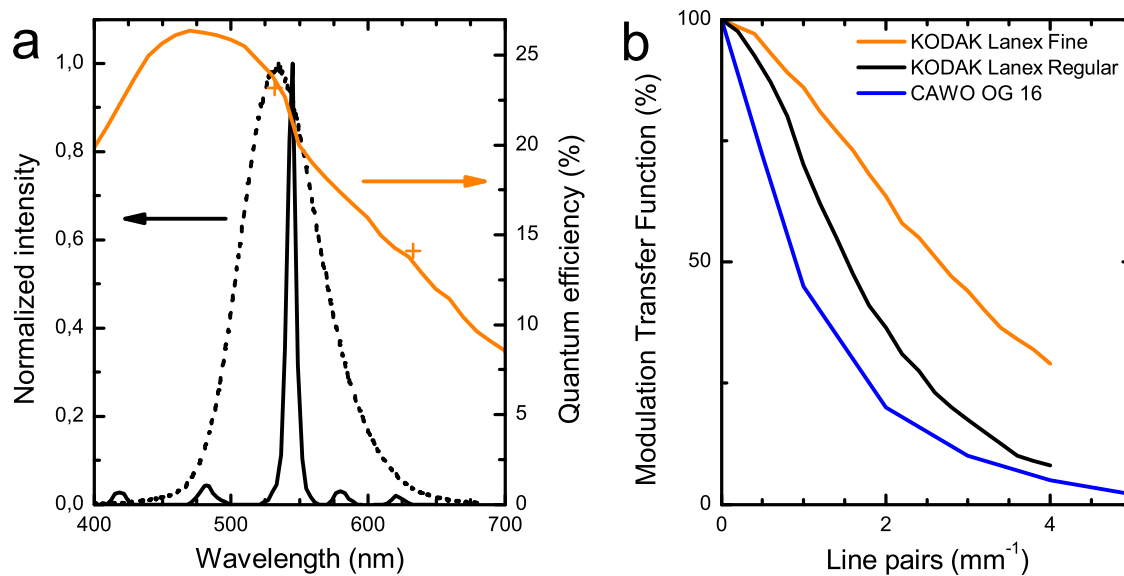


Figure 2.11: **Emission spectrum, quantum efficiency, and modulation transfer function.** **a**, Emission spectra of the CAWO OG 16 screen (solid black line) and the constant light source (dashed line). Measured values of the absolute quantum efficiency of the CCD camera (orange crosses) and scaled quantum efficiency curve of the CCD chip (orange line). **b**, Modulation transfer function (MTF), i.e., resolution of three different scintillating screens. Screens with higher efficiency (e.g. CAWO OG 16) have lower resolution.

show a linear response over a wide measurement range. The KODAK Biomax MS screen has the highest scintillation efficiency, while KONICA KF has the lowest. The efficiency is mainly determined by the thickness of the scintillating layer. Naturally, screens with a thicker phosphor layer also have a lower resolution as shown in fig. 2.11b. However, since the spatial resolution of the imaging system is typically limited to  $\approx 0.5$  mm, the screen resolution is not the limiting factor and screens with a thick layer and high efficiency can be used. KODAK Lanex Regular was used for all experiments presented in this thesis.

When transferring this calibration to the experiment, the absolute calibration of the collection efficiency of the imaging system has to be determined carefully so that the correct charge values are obtained. To simplify the transfer, the scintillating screens have also been cross-calibrated to a constant light source (CLS). To this end, small Tritium-filled capsules covered with a green-emitting phosphor (see inset in fig. 2.10b for a cross-section and 2.11a for the spectrum) were placed on the scintillating screens next to the area where the electron beam was impinging. Thus, the imaging system in the LWFA experiment is calibrated by comparing the intensity from the CLS and the scintillation signal from the accelerated electron bunches. The camera was looking at the scintillator and the CLS almost perpendicularly (fig. 2.9).

Figure 2.13 shows the measured scintillator response for the CAWO OG 16 screen on a linear scale. The small deviation from the linear behaviour points towards an onset of saturation in the scintillator. The saturation signal is fitted with Birk's saturation law [135]

$$\rho_{\text{scint}} = \frac{\rho_{\text{real}}}{1 + B\rho_{\text{real}}}, \quad (2.8)$$

where  $\rho_{\text{scint}}$  is the measured charge density, which is calculated from the scintillation signal, and  $\rho_{\text{real}}$  the actual charge density that was sent to the screen from the accelerator measured with the ICT.  $B$  is a fitparameter determining the onset of saturation. A saturation threshold  $\rho_{\text{sat}}$  is defined as the charge density, at which  $\rho_{\text{scint}}$  will have dropped to 95% of the linear fit. Saturation for four screens was detected (see fig. 2.13b), the thresholds are also given in tab. 2.1. It is assumed that the other four screens are also saturating but at even higher charge densities. For this charge, the macropulse length was already a significant fraction of the scintillator decay time. Thus only a lower limit for the threshold can be given.

For practical considerations,  $\rho_{\text{sat}}$  is not reached by current LWFA experiments because the electron beams with a charge between 10 and 100 pC are typically dispersed over an area on the order of several  $\text{cm}^2$  in the electron spectrometer. The limit can be reached only by focusing with magnetic lenses [136], but even then the real charge can be calculated by the saturation law of eq. (2.8) if the threshold is not exceeded too much.

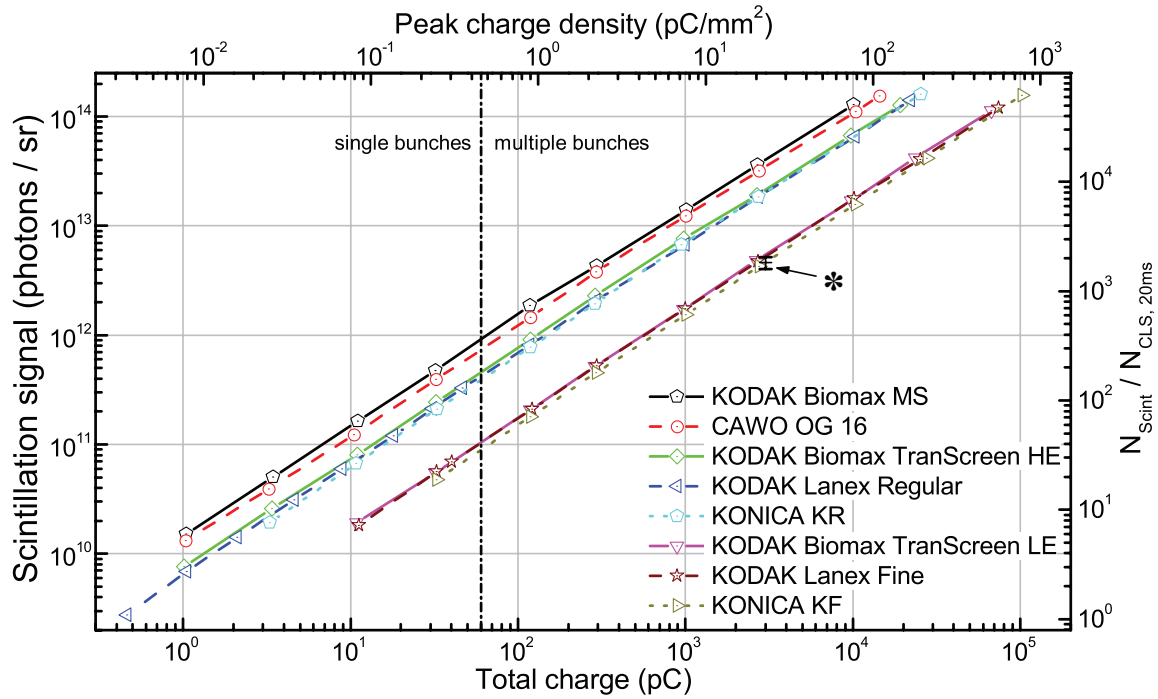


Figure 2.12: **Absolute calibration of scintillating screens.** Log-log-plot of the scintillator signal vs. total charge or charge density respectively for eight different screens. The linearity of all screens is verified over more than four orders of magnitude, the slopes from the linear fit are given in tab. 2.1. The star marks the comparison with the value reported by Glinec et al. [130] for the KODAK Lanex Fine screen, which is in agreement with our measurement.

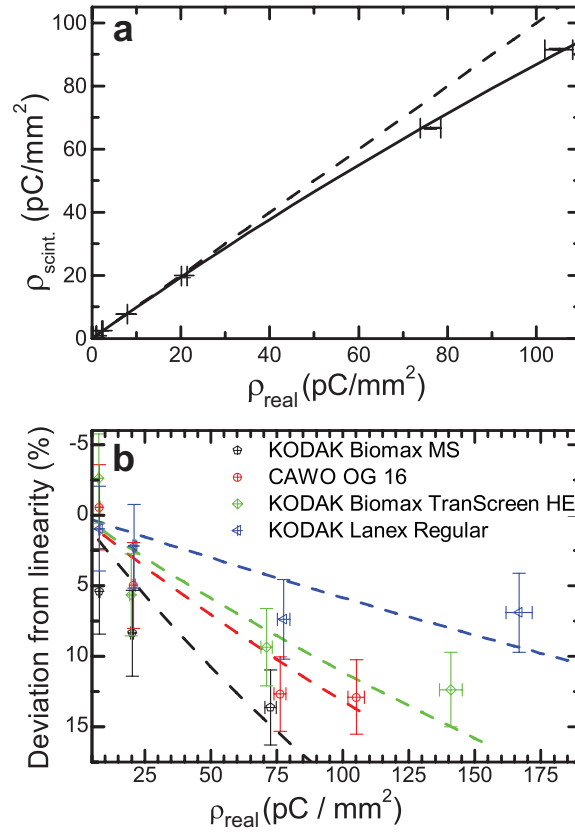


Figure 2.13: **Saturation of scintillating screens.** **a**, Linear plot of the apparent charge density  $\rho_{\text{scint}}$  vs. the applied charge density  $\rho_{\text{real}}$  obtained from the ICT for the CAWO OG 16 screen. The deviation from the linear behaviour (dashed line) is due to saturation of the scintillator and is fitted with eq. (2.8) (solid line). **b**, A deviation from the linearity as in **a**) was detected for four screens. The dashed lines show fits with eq. (2.8).

### 2.3.4 Pointing monitor

The scintillating screens are also used as pointing and divergence monitor. For this purpose, a scintillating screen can be moved into the electron beam at the entry of the electron spectrometer during the experiment (fig. 2.1). The emitted scintillation signal is recorded with another CCD camera (QCam) outside of the vacuum chamber. A  $10\ \mu\text{m}$  Aluminum foil is placed on the scintillating screen to shield the direct laser light, which would disturb the measurement and possibly destroy the camera chip. By measuring the distance between the gas jet and the pointing screen, the beam pointing and the divergence can be obtained.

### 2.3.5 Advanced diagnostics

In the past sections, the basic diagnostic tools to measure the electron energy, charge, and divergence have been described. However, along with the rapid development of LWFA, also the demand for advanced diagnostics is increasing. First application experiments with LWFA produced electron beams, such as the generation of coherent X-ray beams from undulators [32] or Thomson scattering [137], or potentially also ultrafast electron diffraction [138], ask for a characterization of the transversal and longitudinal emittance, i.e., the transverse beam quality and the longitudinal profile / bunch duration. For the further development of LWFA it is also crucial to get more insight into the acceleration process itself, e.g., by visualizing the plasma wave itself [51, 52], if possible together with the injected electron bunch. The results on these advanced diagnostics are presented in chapter 4.



# Chapter 3

## Controlled injection of electrons into wakefields

The theoretical concepts and the basic experimental setup have been introduced in chapters 1 and 2. Now, the experimental results on electron acceleration with different injection mechanisms are presented. Sec. 3.1 is focused on the results obtained with LWS-20 (65 mJ on target, 8 fs) and the self-injection process. A comparison to the previously obtained results with LWS-10 (35 mJ on target, 8 fs) by Schmid et al. is given [57, 122]. Sec. 3.2 shows how the accelerator output was stabilized via controlled injection of electrons at a sharp density transition. Due to the high quality electron bunches obtained here, this method was also used in combination with the ATLAS laser (1 J on target, 26 fs), where bunches with even higher energy and charge could be produced (see sec. 3.3).

### 3.1 LWFA with LWS-20 in the self-injection regime

In the previous experiments performed with LWS-10, i.e., LWS-20 before the energy-doubling upgrade, it was shown that electron bunches with around 25 MeV could be obtained with only 35 mJ on target in the self-injection regime [122]. Single shots up to 50 MeV were observed, but the accelerator output suffered strong instabilities. Typically, only few percent of the laser shots produced high quality electron bunches. The results suggested that the instabilities are mainly caused by the fluctuations of the laser parameters. Since the focused intensity was just at the threshold for the self-injection regime, short series of consecutive shots with similar parameters could only be produced at lower energies, typically 8-15 MeV.

Now, these experiments were repeated in the same setup with the upgraded laser. The 8 fs output pulses of LWS-20 were focused onto a supersonic He gas jet, typically with

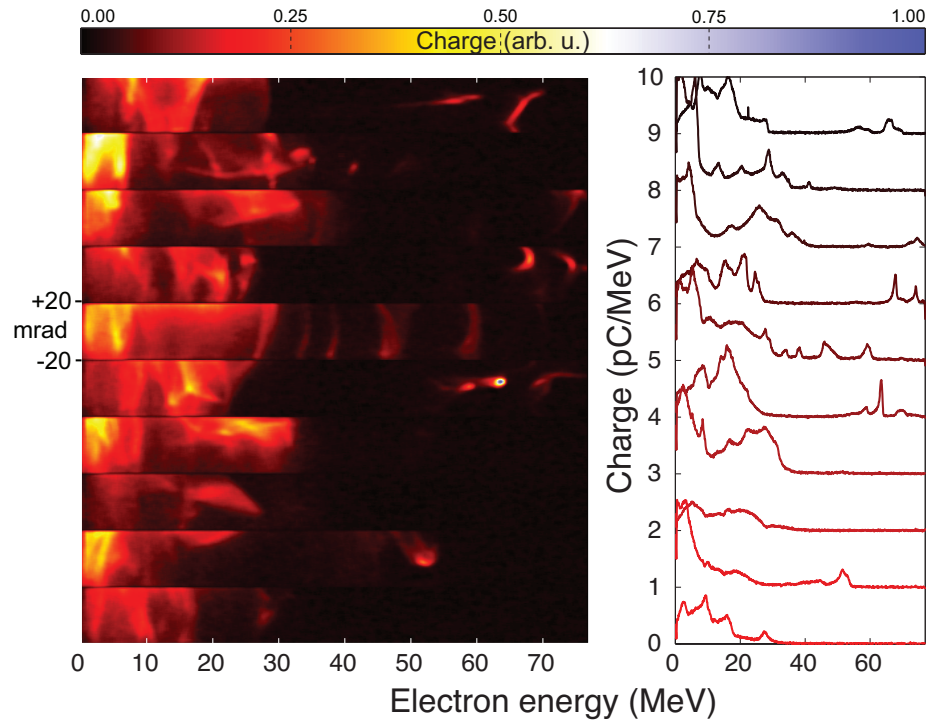


Figure 3.1: **High energy series of self-injected electrons with LWS-20.** False color image of the detected charge on the scintillating screen and lineouts integrated in the angular (vertical) direction of 10 consecutive laser shots. The charge in the high energy peaks is around 1-2 pC, the FWHM divergence about 5 mrad. The lineouts are offset vertically to fit the corresponding scintillator image.



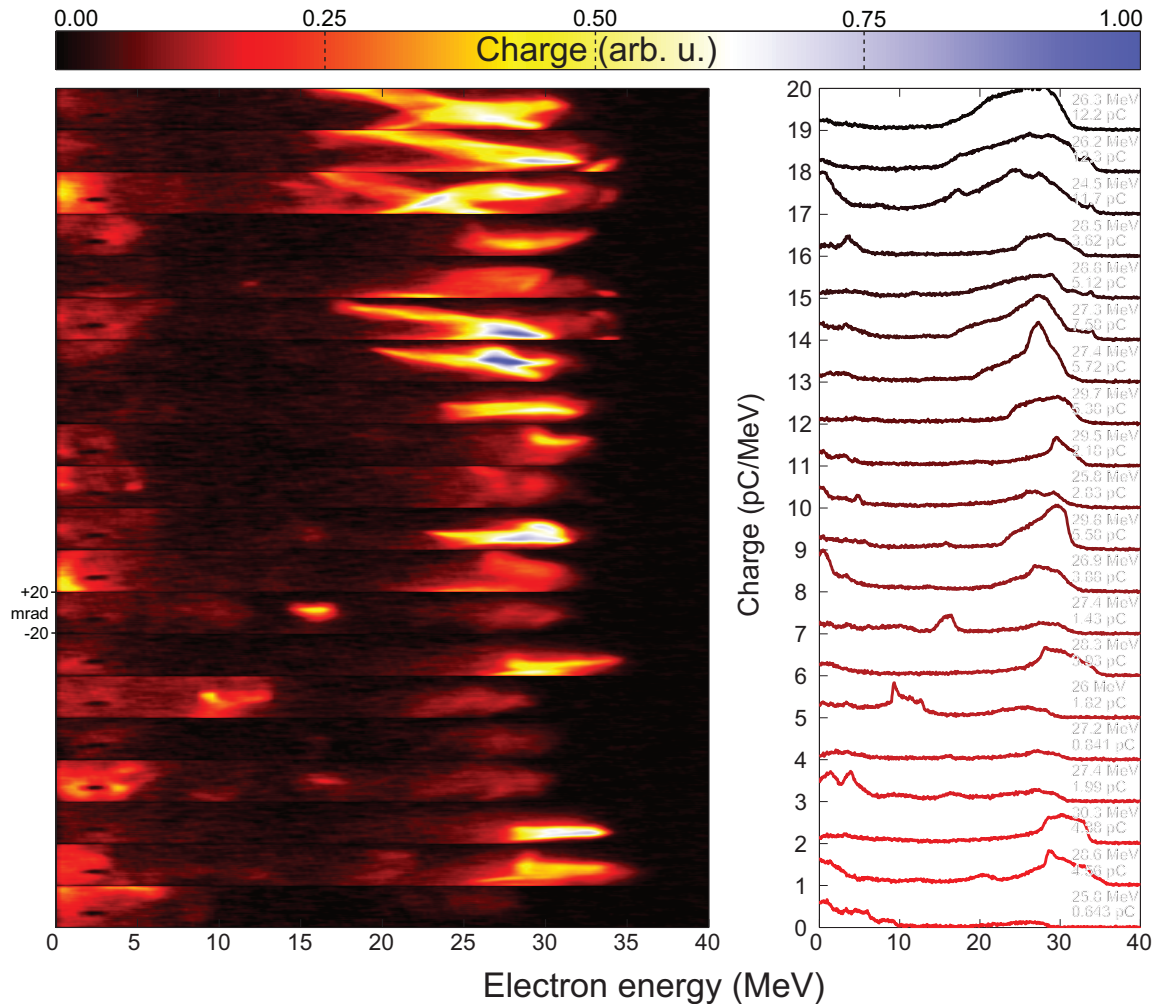


Figure 3.2: **Stable series of self-injected electrons with LWS-20.** False color image of the detected charge on the scintillating screen and lineouts integrated in the angular (vertical) direction of 20 consecutive laser shots. The lineouts are offset vertically to fit the corresponding scintillator image. Statistics for the 500 shots of this run:  $E_{\text{peak}} = (27.7 \pm 2.1)$  MeV,  $\Delta E = (5.7 \pm 2.6)$  MeV FWHM,  $Q = (3.8 \pm 3.6)$  pC, FWHM divergence 8 – 18 mrad.

300-500  $\mu\text{m}$  diameter. Due to a strongly modulated laser beam profile and maybe also residual phase front distortions, about 50 % of the laser energy was scattered into the wings of the focal spot. Thus, about 25 % of the energy are within the FWHM, leading to an intensity of  $2.5 \cdot 10^{18} \text{ W/cm}^2$  (see sec. 2.1.1 for details). Figure 3.1 shows the accelerator output from 10 consecutive laser shots. Here, the parameters ( $n_e = 2.6 \cdot 10^{19} \text{ cm}^{-3}$ ) have been chosen to reach the maximum electron energy. Some peaks in the electron energy spectrum with  $\sim 70 \text{ MeV}$  are visible, which is about 40 % more compared to the previous results before the laser upgrade. This amount of energy increase due to a doubling in laser power agrees with the expected value from the scaling laws (sec. 1.9). However, as it is already visible in the figure, the accelerator output is very unstable at these operating conditions. Only a small percentage of the shots show a nice peak in the electron energy spectrum, typically it is accompanied by a much larger number of low energy electrons with a larger divergence.

The quality of the accelerator output could be increased significantly by tuning the parameters to lower electron energy. Fig. 3.2 shows a series of 20 consecutive shots obtained at  $n_e = 3.6 \cdot 10^{19} \text{ cm}^{-3}$  with carefully optimized parameters. Monoenergetic electron bunches are generated in 90 % of the shots with a peak energy of 25-30 MeV, but rather large charge fluctuations. This observation of stable electrons with self-injection is similar to the findings in Schmid [122], where it was also shown that stable operation can be achieved at lower electron energies. Similar to the comparison of the highest energy shots, the electron energy for stable operation has also increased by about 50 % due to the increased laser energy.

Although this series shows a great improvement compared to the previous results obtained with LWS-10, the fluctuations in the electron parameters, especially the injected charge, could not be removed completely. Additionally, the shots typically show a rather broad energy distribution. The fluctuations are mainly attributed to fluctuations in the laser parameters (energy, spectrum, pulse duration, focus quality) as also suggested by Schmid [122], but other influences, e.g. the exact gas density, are imaginable, too.

The key element for stable or unstable electron acceleration is the injection of background plasma electrons into the plasma wave. The self-injection process used so far is highly nonlinear with the laser intensity, thus even small local fluctuations will lead to big instabilities. Reproducible accelerator operation with similar high-quality electron bunches in  $> 90 \%$  of the laser shots apparently requires a degree of stability of all parameters, which is not realistic in the current setup. Therefore, an advanced scheme of electron injection into wakefields utilizing a sharp density transition is described in next sections. In this scheme, the injection is less dependent on the laser intensity, which leads to more stable accelerator operation. Additionally, the new injection scheme allows for much easier tuning of the electron energy, a parameter with very limited and indirect control in the

self-injection scheme, since it depends strongly on the laser pulse evolution in the plasma.

## 3.2 Controlled injection at sharp density transitions with LWS-20

### 3.2.1 Stable electron runs with tunable energy

As described in sec. 1.10, electrons can not only be injected into wakefields via the self-injection process, but also at transitions in the plasma density. Here, the method of utilizing a sharp, downward density transition was used (see fig. 1.10). As described in more detail in the theory section, some of the background plasma electrons forming the plasma wave can be injected into the accelerating phase of the wakefield upon crossing the density transition.

The density transitions are produced with the same supersonic nozzles that were already used for the self-injection experiments with the same general setup (fig. 2.1). By introducing a razor blade into the flow a shock is created which leads to the step in the longitudinal density profile (see fig. 2.8b and sec. 2.2). The position and the ratio of the density step are defined by the position of the razor blade and the Mach number  $M_1$ . In this advanced scheme, the energy of the accelerated electron bunch can be controlled via the injection position. If the experiment is not limited by dephasing or depletion effects (sec. 1.8), electrons are accelerated from the density transition until the end of the gas jet. A schematic view of the new setup is shown in fig. 2.8a. The razor blade is moved into the flow right above the nozzle exit and the laser is focused into the disturbed flow a few hundred micron above. Fig. 2.8b shows a typical density profile. Since the transition is  $< 5 \mu\text{m}$  wide, the plasma wave "feels" an instantaneous density jump.

Parameter	Low energy	High energy
Electron energy (MeV)	$18.6 \pm 1.6$	$31.6 \pm 2.5$
Energy spread FWHM (MeV)	$3.5 \pm 1.7$	$9.0 \pm 2.8$
Charge (pC)	$0.90 \pm 0.45$	$1.44 \pm 0.87$
Divergence FWHM (mrad)	9 – 12	5 – 10
Electron density ( $\text{cm}^{-3}$ )	$1.2 \cdot 10^{19}$	$2.3 \cdot 10^{19}$
Injection probability	97 %	85 %

Table 3.1: **Parameters of the two electron runs with controlled injection and LWS-20 shown in fig. 3.3.** The given error intervals represent 1 s. d.

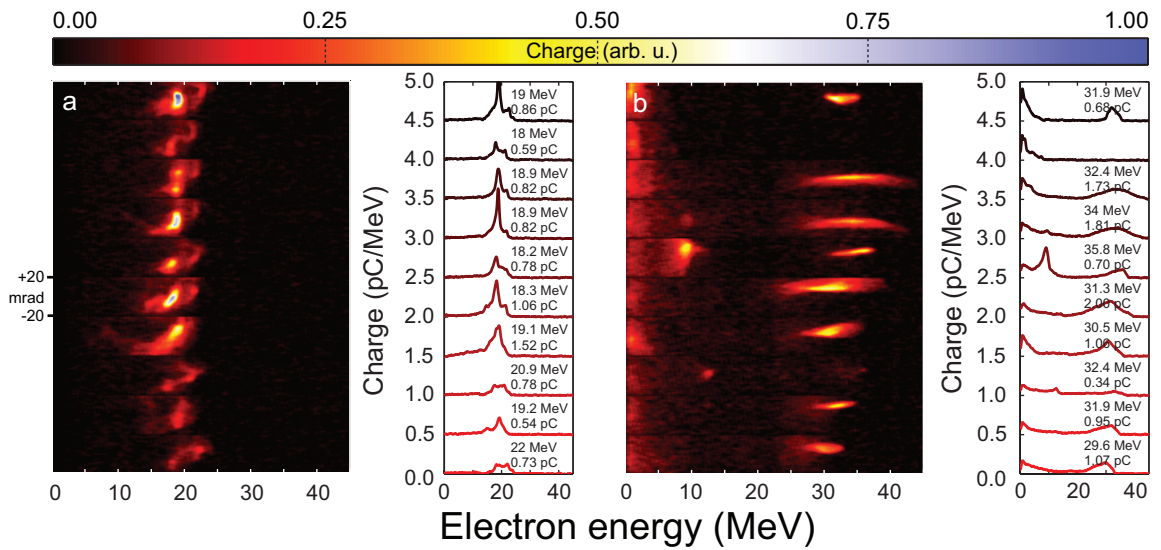


Figure 3.3: **Two stable electron series injected at the density transition with LWS-20.** False color image of the detected charge on the scintillating screen and the corresponding lineouts integrated in the angular (vertical) direction of 10 consecutive laser shots each. The lineouts are offset vertically to fit the corresponding scintillator image. The parameters and statistics for both runs are given in tab. 3.1.

In the experiment, electrons were first accelerated via self-injection in the bubble-regime at  $n_e \sim 3 - 4 \cdot 10^{19} \text{ cm}^{-3}$ . Then, the electron density was lowered (tab. 3.1), until the self-injection process stopped, i.e., the laser still generated a nonlinear wakefield, but the density was not high enough for electron trapping to occur. Upon moving the razor blade into the flow and creating the density transition, electron acceleration was restarted. At the same time, a bright spot was visible at the intersection of the shockfront and the plasma channel (see sideview image in fig. 2.8a). Since the electrons experience the strongest acceleration (from  $v \approx 0$  to  $v \approx c$ ) in the beginning right after the shockfront, they radiate strongly at this position, similar to the wave breaking radiation reported by Thomas et al. [139]. The intensity of the spot showed a correlation with the accelerated charge. These two observations (restart of the acceleration process, bright spot at injection position) support the claim that now the electrons are indeed injected into the wakefield at the electron density jump.

Figure 3.3 shows two series of consecutive shots, where different acceleration parameters (position of the density step, absolute gas density) have been chosen to obtain different peak energies. The detailed run parameters are found in tab. 3.1. It is apparent that the peak energy is stabilized compared to the self-injection results. This is due to the fact that this type of electron injection has a weaker dependence on the nonlinear laser pulse evolution. Additionally, the parameter range to reach stable acceleration is bigger than in the self-injection. Thus, the accelerator is not limited to one good parameter set with one specific peak energy. Instead, the electron energy is tunable by the position of the density transition, as shown by fig. 3.3 (see also further examples in the next sections).

Parameter	Self-injection	Density transition injection
Electron energy (MeV)	$29.5 \pm 2.3$	$18.7 \pm 0.4$
Energy spread FWHM (MeV)	$3.0 \pm 1.9$	$1.5 \pm 0.2$
Charge (pC)	$3.4 \pm 0.6$	$1.3 \pm 0.2$
Divergence FWHM (mrad)	$\sim 10$	$\sim 10$

Table 3.2: **Parameters of the selected shots of two electron runs with self-injection and controlled injection with LWS-20 shown in fig. 3.4.** The given error intervals represent 1 s. d.

A direct comparison of two good runs with self-injection and controlled injection is given in fig. 3.4. Here, the 10 shots with the lowest energy spread of each run have been selected. The improvement in overall beam quality is obvious, especially upon looking at the low energy side of the electron spectra. In contrast to the self-injected electrons, the electron bunches injected at the density transition have no low energy tail, which is due to the temporally confined injection. The improvement also manifests itself in the shot

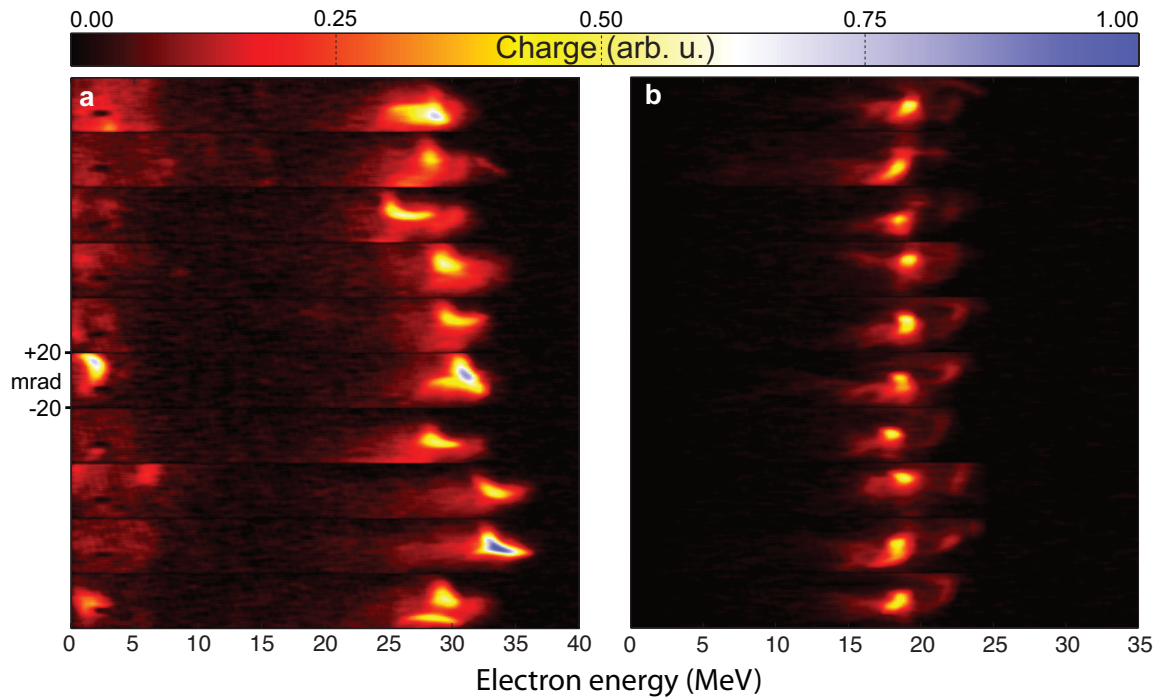


Figure 3.4: **Comparison of self-injection and density transition injection with LWS-20.** False color image of the detected charge on the scintillating screen. For both runs, 10 selected shots with the smallest energy spread obtained with self-injection **a)** and controlled injection **b)** are shown, which corresponds to the best few percent of each run. The shot parameters are given in tab. 3.2.

parameters given in tab. 3.2. While the divergence is similar, all other beam parameters show increased stability in the case of shockfront injection. It appears that the charge is higher in the self-injection case. However, it should be noted that the charge per energy interval, which is the important figure for future applications, is equal for shockfront injection. Most importantly, while only a small percentage of the self-injected electrons have such a high quality and low energy spread, almost all of the shots with shockfront injection show similar parameters to the selected shots (compare with the consecutive shots in fig. 3.2 and 3.3a).

### 3.2.2 Measuring the longitudinal field and dephasing effects

The increased stability of the electron beam enabled a more detailed study of the LWFA process. The peak energy of the electron bunch can be controlled within a certain range as already seen in fig. 3.3. By varying the position of the density transition over a wider range for the same experimental parameters, the accelerating field experienced by the electrons can be studied. Figure 3.5b shows the peak energy for different injection positions. As expected, the energy is smaller for later injection positions, which is a direct consequence of the shortened acceleration length. We see that for longer acceleration distances the energy does not increase linearly, but saturates at a threshold. This can be understood by the dephasing effect (see sec. 1.8). Once the electrons have reached a few MeV energy, they are faster than the plasma wave and thus run into regions of smaller accelerating field in the plasma wave. Assuming a highly nonlinear plasma wave with a linear electric field (comp. fig. 1.4), the energy gain should have a parabolic shape. This is well confirmed by the applied fit (fig. 3.5b).

From the fit parameters, several important quantities of this run are obtained. We see that the acceleration terminates about  $200 \mu\text{m}$  after the center of the gas jet. The longitudinal electron density profile is given in fig. 3.5a. At this position, the density has dropped to about 80 % of the maximum value. When extrapolating towards zero energy, we get a maximum accelerating field of 130 GV/m. A maximum energy gain of 20 MeV is obtained with a total acceleration length of  $300 \mu\text{m}$ . Here, the electron bunch charge is about 1-2 pC, thus the peak energy is not strongly influenced by beamloading (see next section). For longer acceleration length (injection at positions  $< -100 \mu\text{m}$ ) the energy is even expected to drop again. However, this could not be measured because the shockfront could not be moved to this position.

In this experiment, the ratio of the plasma wavelength before and after the transition is  $\sim 1.5$ , i.e., the electrons are expected to be injected at a position approximately  $\lambda_p/4$  before the electron density peak at the back of the bubble. This leads to a reduced dephasing length compared to self-injection, where the electrons start the acceleration from the back

of the bubble. Thus, the measured dephasing length of  $300 \mu\text{m}$  is in good agreement with the value of  $\approx 600 \mu\text{m}$  obtained with eq. (1.60) given in sec. 1.8. The maximum peak energy of 20 MeV in this case is not in contradiction with the 30 MeV electrons obtained at slightly higher density (fig. 3.3), because the density ratio at the step was smaller in the 30 MeV experiment, leading to an injection more into the back of the bubble and longer dephasing length. The measured field of 130 GV/m is expected to be about 50 % of the maximum field out of the same reason.

At the maximum electron density of  $1.8 \cdot 10^{19} \text{ cm}^{-3}$ , the laser group velocity in the plasma is about 99.5 % of the vacuum speed of light. Thus, electrons with 20 MeV travel  $0.005c$  faster than the surrounding accelerating structure. If we assume that the electrons have relativistic speed right after injection, the electron bunch will effectively move  $1.5 \mu\text{m}$  forward in the bubble during the  $300 \mu\text{m}$  of acceleration. This length should equal the distance from the injection position to the bubble center, which is also  $\lambda_p/4$ . Thus, we expect a plasma wavelength of about  $6 \mu\text{m}$ , which is in good agreement with the value of  $7.8 \mu\text{m}$  from the density measurement.

### 3.2.3 Observation of beamloading

Loading the plasma wave with a large number of electrons in turn reduces the accelerating fields significantly, an effect which is commonly referred to as *beamloading* (see sec. 1.8). The question of how many electrons can be loaded into a certain wake without degradation of the bunch parameters is very important, since it enables an estimation of how the LWFA output scales with bigger laser systems that are currently planned or under construction. Due to the stable peak energy of the electron bunch, the effect of the loaded charge on the field could be measured. Fig. 3.6 shows a run similar to fig. 3.3, but this time the shots are not consecutive. Instead, they were sorted by accelerated charge in the energy interval of 3-40 MeV. A clear dependence of the peak energy (fig. 3.6b) and relative energy spread (fig. 3.6c) is visible. In our experiments, the reduction of the acceleration gradient is estimated to be 1.8 MeV/pC. This result is very close to the measurement by Rechatin et al. [90], where a reduction of 1.9 MeV/pC is shown. While these two numbers are similar, they see a rise of the electron energy spread starting around 25 pC, while we already see an effect at 2-3 pC. This could be explained by the fact that they have similar laser intensity ( $a_0 = 1.5$ ), but lower plasma density ( $n_e = 5.7 \cdot 10^{18} \text{ cm}^{-3}$ ) compared to  $n_e = 3.1 \cdot 10^{19} \text{ cm}^{-3}$  in our case. Thus, the plasma wavelength is 2.3 times shorter in our case, which leads to a difference in bubble volume of  $2.3^2 \approx 12$ . Correspondingly, it is expected that the amount of charge that can be loaded in the bigger bubble at lower densities is 12 times higher, which agrees excellently with the measured charge thresholds. The reduction in electron energy, however, is determined by the density of the electron bunch itself within



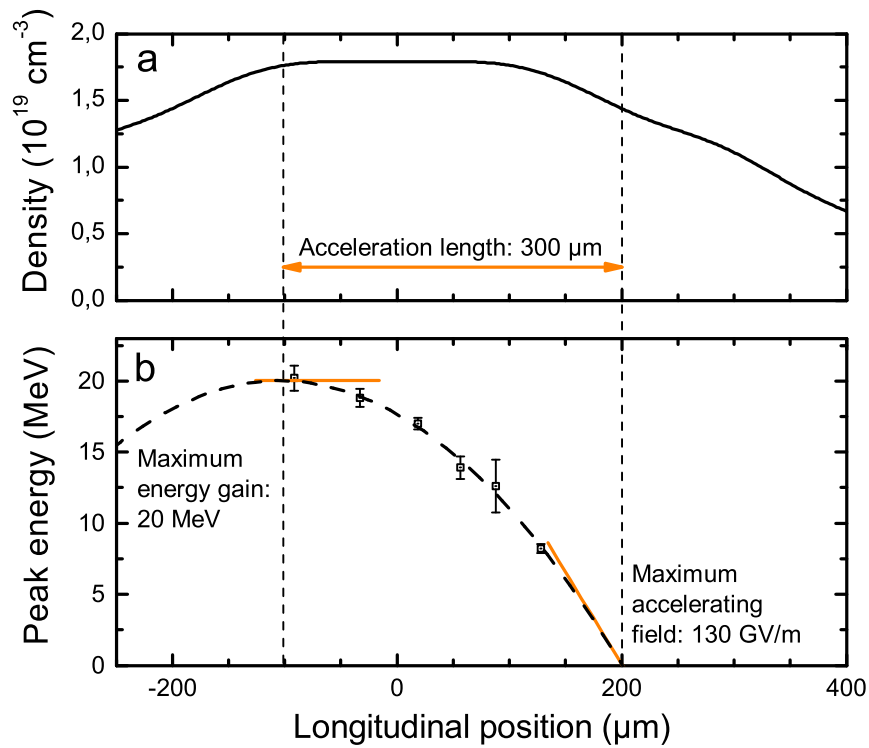


Figure 3.5: **Accelerating field and dephasing of the electron bunch.** **a**, Electron density along the laser propagation evaluated via Abel inversion. **b**, Peak electron energy for different injection positions (black squares) showing the dephasing of the electron bunch with respect to the plasma wave for longer acceleration length (earlier injection). The dashed line shows a parabolic fit to the data points, revealing the maximum energy gain, the accelerating field, and the acceleration length (orange) for these conditions.

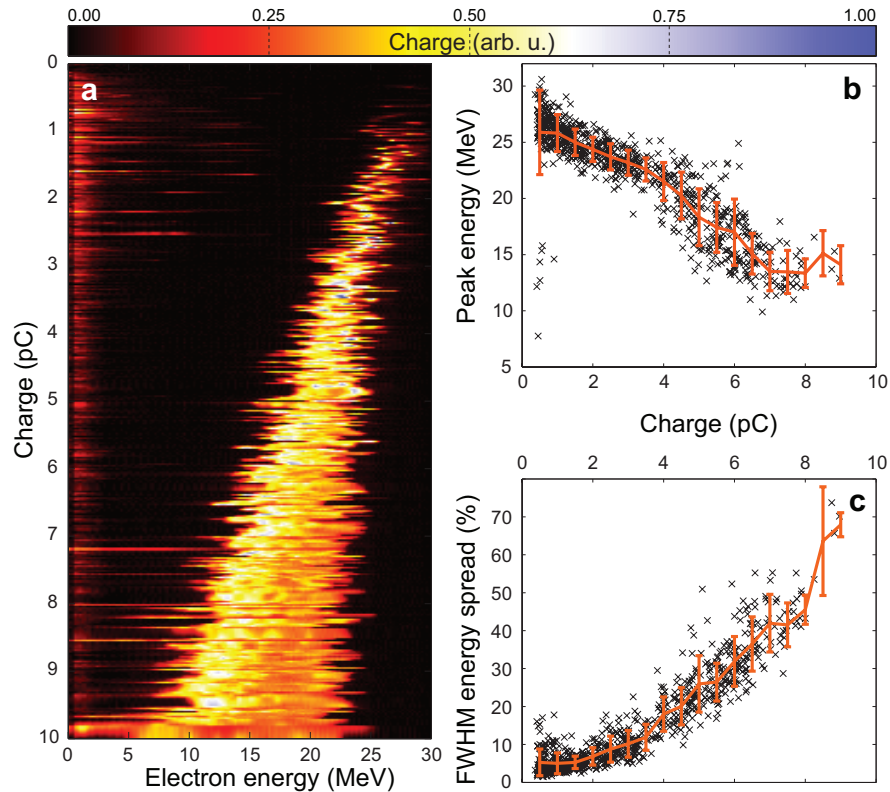


Figure 3.6: **Observation of beamloading.** **a**, Energy spectra of 2300 shots of this run sorted by the charge contained in the 3-40 MeV energy interval. **b** and **c** show the scaling of peak energy and relative energy spread, respectively, vs. peak charge. The orange lines show binned data, error bars are 1 s. d.

the bubble. Thus, it is suggested that in both experiments with similar laser intensity, the electron density in the bunch is the same, leading to a similar reduction of the acceleration gradient.

### 3.2.4 Scaling with the background electron density

Another interesting question which we were able to study is the scaling of the peak electron energy with the background plasma density, in which the wakefield is generated. Experimentally this was achieved by an electron run, where the parameters were first optimized to obtain monoenergetic electron spectra as in fig. 3.3. Afterwards, the backing pressure of the He nozzle was scanned up and down several times while all other param-

ters were fixed in order to study the change in the energy spectrum as shown in fig. 3.7a. The dependence on the electron density of the high energy cut-off of the electron energy spectra is plotted in fig. 3.7b. Here, the electron bunch charge is constant for all densities around 0.5-1.0 pC, so beamloading effects are not important in this case. Although some fluctuations are visible, the data points suggest a linear trend. By extrapolating the data points by a linear fit to zero energy, a density of  $n_e = 5 \cdot 10^{18} \text{cm}^{-3}$  is retrieved. The results seem to be in contradiction with the fourth-root law for the longitudinal electric field at the cold-wavebreaking limit in eq. (1.56).

This could be explained by two different effects. Firstly, it seems that a certain electron density is required to start the acceleration process ( $n_e = 1.0 \cdot 10^{19} \text{cm}^{-3}$ ,  $\lambda_p = 10.5 \mu\text{m}$ ). If the laser pulse duration is much shorter than  $\lambda_p$ , the plasma wave is not driven efficiently and the amplitude drops rapidly (comp. fig. 1.5). Secondly, an increase in density might not only increase the accelerating field, but also extends the region where the density is high enough to sustain an accelerating plasma wave, because here the electron density is not a flat top profile, but similar to the profile shown in fig. 3.5a. Thus, the electron energy would increase due to two effects, explaining the linear rise of the peak energy. The formula for the maximum energy gain due to dephasing of the electrons from eq. (1.61) gives more than 100 MeV for this electron density range, so dephasing is not the limiting factor in this measurement.

The results of this density scan and the results from the previous sections show that the controlled injection at the density transition opens up a wide electron density range for the experiments. However, certain requirements have to be met. The electron density should be chosen such that the plasma wavelength is not much longer than  $\sim 2\tau_{LC}$  to drive the plasma wave efficiently.

## 3.3 Controlled injection with ATLAS

### 3.3.1 Stable injection

Due to the successful demonstration of the shockfront injection scheme with LWS-20, this method was also tried with ATLAS (see sec. 2.1.2). In contrast to LWS-20, the light pulses produced by this laser are longer ( $\tau_{\text{ATLAS}} \approx 26 \text{ fs}$ ), but have an order of magnitude more on-target energy ( $E \approx 770 \text{ mJ}$ ). Thus, they have the potential to produce electron bunches with higher peak energy and more charge, as it was already demonstrated in the past with capillary targets [29, 140]. However, the results obtained with ATLAS so far have very often had broad, plateau-like energy spectra and have shown rather great fluctuations.

The ATLAS shockfront experiments were performed with the same setup as used for LWS-20 (fig. 2.8). Typically, longer acceleration lengths were used. This was achieved

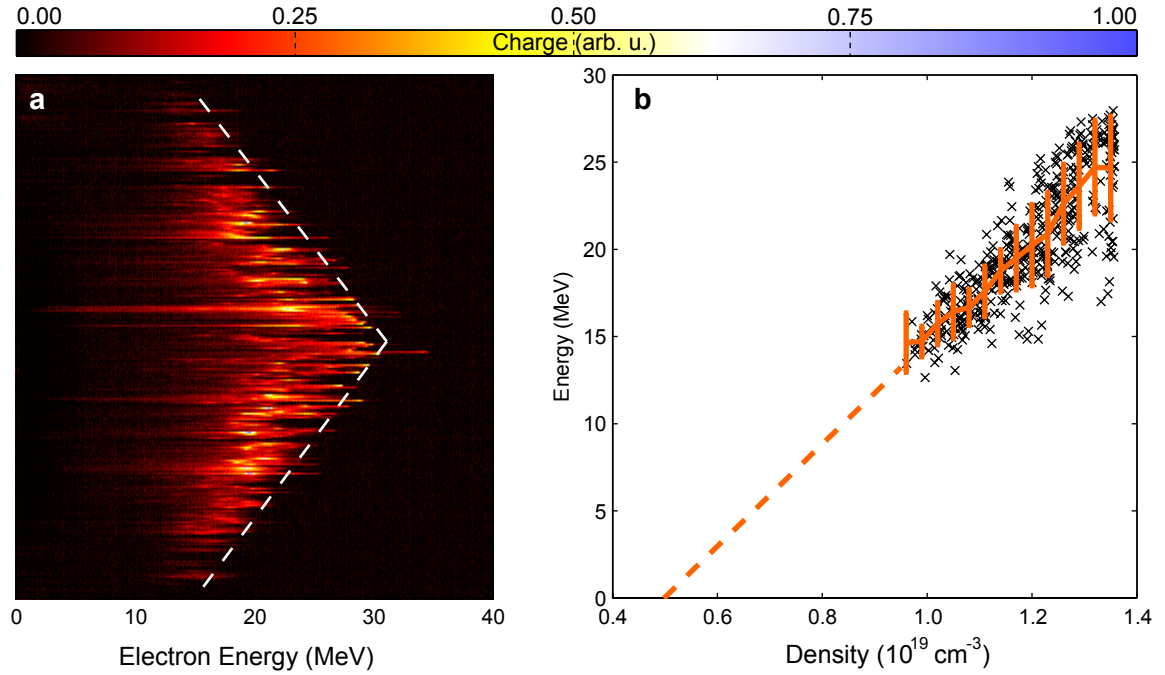


Figure 3.7: **Scaling of the electron energy with the electron density.** **a**, Electron energy spectra of a scan where the electron density was increased and decreased linearly. The white line is a guide to the eye for the high energy cut-off. **b**, The black crosses show the high energy cut-off from several density scans as shown in **a**). The orange line shows binned data points, the error intervals represent 1 s. d. The dashed line is a fit to all the shown data points to extrapolate to zero energy at  $n_e = 5 \cdot 10^{18} \text{ cm}^{-3}$ . The electron bunches have 0.5-1.0 pC charge.

Parameter	Self-injection	Density transition injection
Electron energy (MeV)	$28.3 \pm 1.7$	$24.3 \pm 0.70$
Energy spread FWHM (MeV)	$20.6 \pm 6.7$	$3.07 \pm 0.65$
Charge (pC)	$19.2 \pm 2.0$	$8.0 \pm 1.5$
Divergence FWHM (mrad)	20 – 30	20 – 30
Electron density ( $\text{cm}^{-3}$ )	$1.2 \cdot 10^{19}$	$0.6 \cdot 10^{19}$
Injection probability	93 %	99 %

Table 3.3: **Parameters of the two electron runs with self-injection and controlled injection at the density transition with ATLAS (fig. 3.8).** 500 shots were recorded in each run. The given error intervals represent 1 s. d.

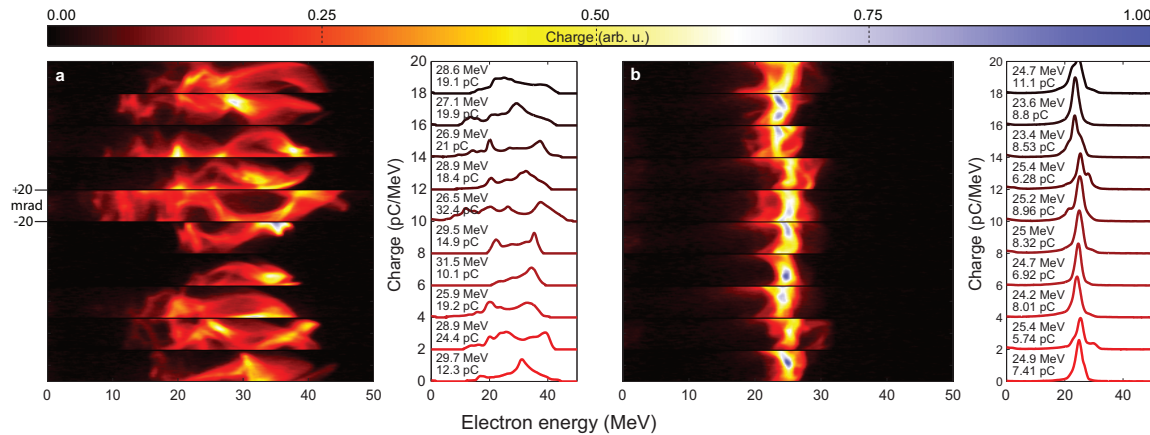


Figure 3.8: **Comparison of self-injection and density transition injection with ATLAS.** False color image of the detected charge on the scintillating screen and the corresponding lineouts integrated in the angular (vertical) direction of 10 consecutive shots with self-injection in **a)** and controlled injection in **b)**. The lineouts are offset vertically to fit the corresponding scintillator image. The electron densities were optimized for the most stable accelerator output. The peak energy in **a)** was evaluated via the first moment because of the broad profiles. The electron parameters are given in tab. 3.3.

either by using bigger gas nozzles (0.5 - 1.5 mm), or by focusing the laser further away from the small nozzles, where a longer, more Gaussian-like profile due to the opening angle of the nozzle is experienced by the laser. First, a comparison between the two injection methods – self-injection and injection at the sharp density transition – was made to prove the injection mechanism. To this end, the ATLAS pulses were focused to a spot size of  $13.5 \mu\text{m}$  FWHM at  $1300 \mu\text{m}$  above the exit of a 1 mm nozzle. Due to non-perfect focus ( $\approx 35\%$  of the energy are in the FWHM), a normalized vector potential of  $a_0 = 2.0$  was reached. Similar to the experiments performed with LWS-20, higher electron densities were needed to accelerate electrons in the self-injection scheme compared to the controlled injection (tab. 3.3). All the parameters except for the electron density were the same for these two runs to have a good comparison.

Figure 3.8 shows 10 consecutive shots of the two comparison runs. A large difference in electron beam quality from self-injection and controlled injection is visible. The detailed electron beam parameters of both runs are given in tab. 3.3. Particularly interesting is the strongly reduced energy spread. While the total integrated charge in the plateau is more in the self-injection case, the charge per energy interval is actually larger for the density transition, as shown by the integrated lineouts in fig. 3.8. Due to the strongly reduced low-energy background with the controlled injection, the harmful background ra-

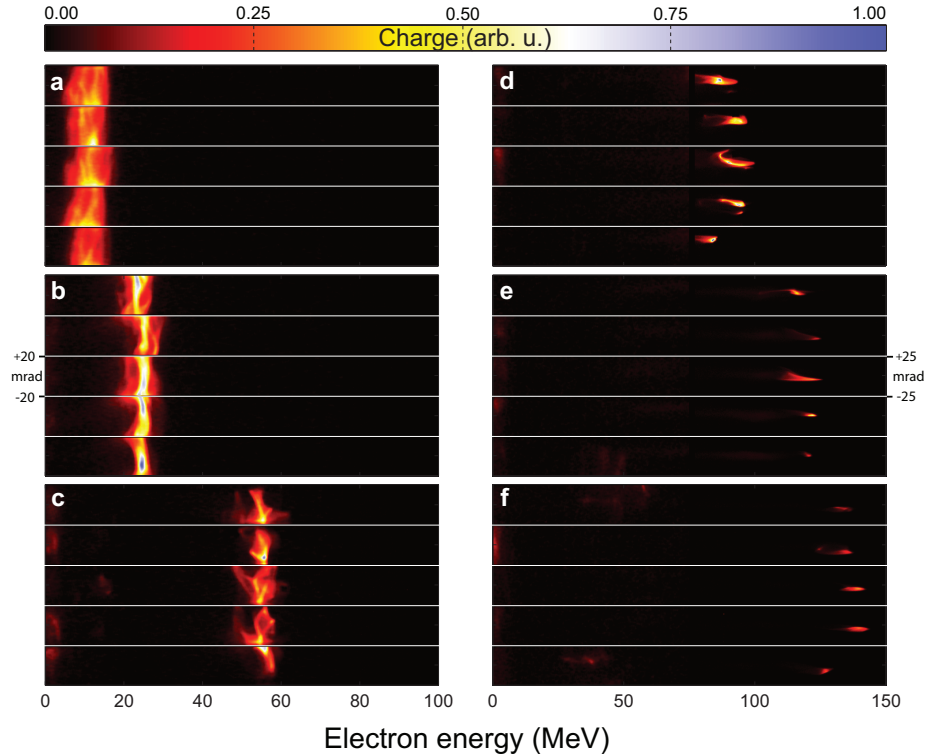


Figure 3.9: **Tunability of LWFA with ATLAS and density transition injection.** Shown are five consecutive shots of six different electron runs, where the accelerator was tuned to different output regimes. The peak energy is stable, the energy bandwidth and the divergence go down for higher electron energies (see tab. 3.4 for run details).

diation generated when stopping the electrons was at least three times lower than in the self-injection case. By comparing these results with the data obtained with LWS-20 and controlled injection, we see that the injected charge was increased by about a factor of 6.

### 3.3.2 Tunability over a wide range

The electron energy in fig. 3.8 is only 25 MeV and thus the same as in the LWS-20 experiments. Due to the higher pulse energy of ATLAS and better stability of all laser parameters, stable electron injection could be obtained much simpler compared to the LWS-20 measurements. Thus, by choosing different parameter of electron density and by varying the position of the shockfront, the accelerator output could be tuned over a wide range (15-150 MeV). The electron energy was not tuned higher due to radiation safety restrictions. Figure 3.9 shows 5 consecutive electron shots for each of 6 electron runs with

different parameters (tab. 3.4). It is apparent that the absolute energy spread is constant around 5-6 MeV, while the electron energy is scaled to higher energies. Since the injection is confined to the narrow time frame when the laser pulse and the plasma wave are crossing the sharp downward density transition, the absolute energy spread is conserved during the acceleration over a distance of many 100  $\mu\text{m}$ . At the same time, the divergence of the electron beam drops significantly for higher electron energies (fig. 3.10a) as it was also observed in our earlier measurements of the emittance of electrons beams produced with LWS-20 [141].

$E_{\text{peak}}$ (MeV)	$\Delta E_{\text{FWHM}}$ (MeV)	$\Delta E/E$ (%)	$Q$ (pC)	Divergence FWHM (mrad)	$n_e$ ( $\text{cm}^{-3}$ )	Nozzle (mm)
$12.1 \pm 1.3$	$8.3 \pm 2.2$	$69 \pm 18$	$8.5 \pm 4.3$	35-40	$2.5 \cdot 10^{18}$	1.0
$25.6 \pm 1.0$	$3.9 \pm 1.0$	$15.2 \pm 3.9$	$6.5 \pm 2.5$	20-30	$6.0 \cdot 10^{18}$	1.0
$54.0 \pm 1.3$	$5.2 \pm 2.4$	$9.6 \pm 4.4$	$6.2 \pm 2.5$	10-15	$5.0 \cdot 10^{18}$	1.0
$95.3 \pm 4.8$	$8.3 \pm 4.7$	$8.7 \pm 4.9$	$6.0 \pm 3.8$	3-6	$2.8 \cdot 10^{18}$	1.5
$119.0 \pm 4.8$	$5.6 \pm 2.4$	$4.7 \pm 2.0$	$1.5 \pm 0.8$	1.8-2.8	$2.7 \cdot 10^{18}$	1.5
$133.3 \pm 7.2$	$6.5 \pm 2.7$	$4.9 \pm 2.0$	$1.2 \pm 1.0$	3.3-3.7	$3.3 \cdot 10^{18}$	1.5

Table 3.4: **Parameters of the six electron runs with controlled injection and ATLAS to show the tunability in fig. 3.9.** The given error intervals represent 1 s. d.

The study of dephasing of the electron bunch in the LWS-20 experiments suggest that the acceleration is stopped approximately, where the electron density has dropped to 80 % of its maximum value (fig. 3.5). By applying this observation to the ATLAS results, the acceleration length can be estimated, even though the end of the acceleration was not measured exactly in these experiments. Figure 3.10b shows the electron energies from the six runs as a function of the assumed acceleration length. Although the experiments have been performed at slightly different electron densities, a linear dependence is found. Thus, the acceleration gradient for ATLAS in this density regime can be estimated to  $\approx 190$  GV/m. This observation is in good agreement with the 40 % larger value of 270 GV/m reported by Faure et al. [39] for similar laser parameters (720 mJ, 30 fs), because in their measurement the electron density was approximately a factor of 2 higher ( $n_e = 7.5 \cdot 10^{18} \text{ cm}^{-3}$ ).

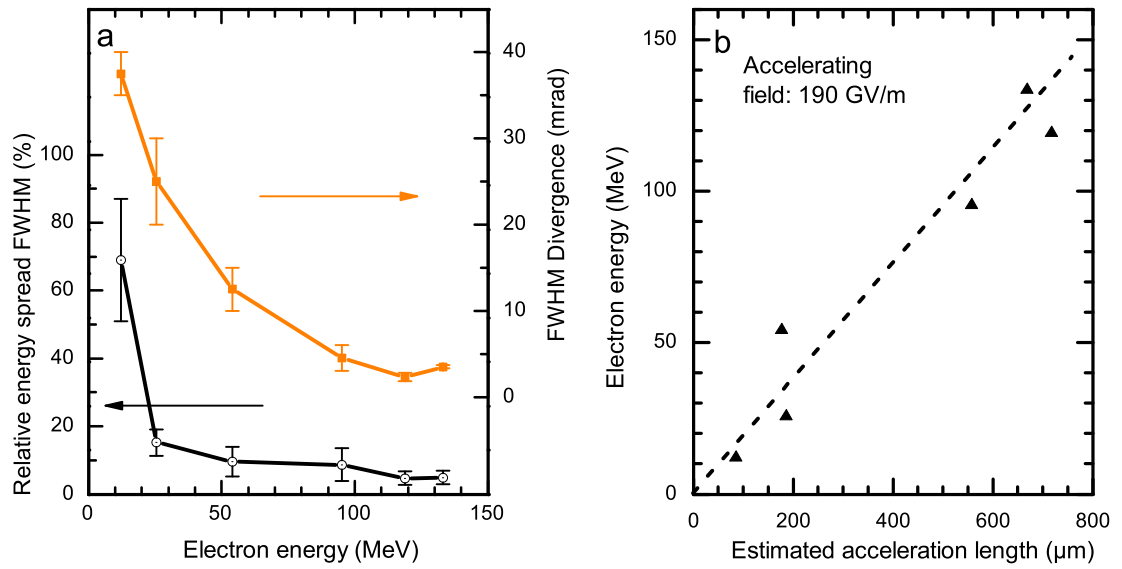


Figure 3.10: **Energy dependence of beam parameters and accelerating field.** **a**, Relative energy spread and FWHM divergence of the six electron runs in fig. 3.9. Error bars are 1 s. **b**, Peak electron energy vs. estimated acceleration length. The acceleration length is estimated as the distance between injection and the position, where the longitudinal density profile drops below 80 %.



# Chapter 4

## Real-time observation of laser-driven electron acceleration

### 4.1 Motivation

Laser wakefield acceleration is capable of accelerating electron pulses with a large bunch charge to relativistic energies as shown in the previous chapter. However, as already mentioned in sec. 2.3 about the basic electron beam diagnostics, the experimental access to the acceleration process itself (as shown in fig. 4.1) has been very limited until now, i.e., direct observation of the the electron bunch and the plasma wave during the interaction has not been possible, and most interpretations of experimental findings have relied on theory or simulations.

First measurements of the plasma wave via frequency-domain holography have been reported in the works of Matlis et al. [51] and Dong et al. [52]. However, due to the time-integrating nature of their measurements, dynamics happening during the process could not be observed. Attempts to measure the electron bunch duration via the transition radiation emitted upon passing through a refractive index boundary [60] were performed by several groups [46–49]. These measurements were only able to give upper limits of  $\geq 30$  fs for the electron bunch duration due to the limited temporal resolution. Only in the recent work of Lundh et al. the authors were able to measure a bunch duration of  $< 2$  fs root-mean-square (RMS) [50]. Still, it has to be pointed out that all bunch duration measurements relied on the indirect measurement of transition radiation. Additionally, the experiments have so far not been able to combine the analysis of the plasma wave and the electron bunch.

This was achieved for the first time via the combination of polarimetry and shadowgraphy, both performed with unprecedented spatio-temporal resolution as described in the

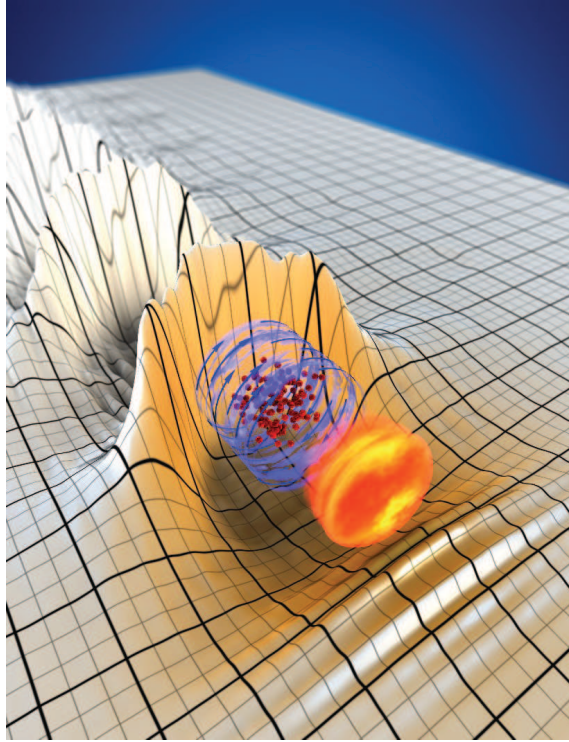


Figure 4.1: **Illustration of laser wakefield acceleration.** The ultrashort laser pulse (orange) drives the plasma wave (3D profile). A number of trapped electrons (red) are trapped in the first oscillation and accelerated by the electric fields in the plasma wave. A magnetic field (blue arrows) is generated by the moving electrons. The density profile was taken from the PIC simulation (fig. 4.3).

next sections. The basic setup for the time-resolved measurements are described in sec. 4.2. Additionally, the experimental findings to expect were simulated via ray-tracing. The experimental detection of the electron bunch inside of the plasma via polarimetry is described in sec. 4.3 and the plasma wave measurement via shadowgraphy in sec. 4.4. Via the combination of both techniques, snapshots of the acceleration process can be taken to reveal the properties illustrated in fig. 4.1, that have only been accessible via simulations up to now. Combinations of many snapshots at different delay steps enable measurements of dynamical effects such as the trapping of electrons inside of the plasma wave (sec. 4.5).

## 4.2 Experimental setup and simulation results

### 4.2.1 Basic setup

The experiments were performed with LWS-20 (sec. 2.1.1) in a setup similar to the one used in the previous chapter (fig. 4.2a). In the current study, the electron accelerator was driven by 8.5 fs (FWHM) laser pulses with an energy of 65 mJ on target. The electrons were trapped via the self-injection mechanism and exhibited a quasi-monoenergetic spectrum of  $E_{\text{peak}} = (19.2 \pm 6.7)$  MeV, an energy spread of  $\Delta E = (2.3 \pm 1.9)$  MeV (FWHM), a divergence of  $(10.9 \pm 3.5)$  mrad (FWHM) after acceleration while carrying a charge of  $Q = (2.3 \pm 1.8)$  pC. Typical electron energy spectra are shown in fig. 4.2c-f.

A small fraction of the main beam ( $\approx 2$  mJ) is split via a hole in one of the plane mirrors upstream of the off-axis parabola and directed (unfocused) onto the gas jet perpendicularly to the main beam (fig. 4.2a+b), where it is used to probe the plasma dynamics. Here, the information about the plasma wave and the electron bunch is imprinted on the properties of the probe pulse by the simultaneous use of two different techniques, namely time-resolved polarimetry [54, 142] and plasma shadowgraphy [76], that are carried out with unprecedented spatio-temporal resolution.

Sub-10-fs polarimetry is based on the probe pulse undergoing polarization rotation due to the Faraday effect caused by the component of the magnetic field parallel to the  $k$ -vector of the probe (see fig. 4.2b and also sec. 1.5). Location, duration, and charge of the electron bunch can be inferred from the measurement of the rotation angle  $\varphi_{\text{rot}}$  in the  $(y, z)$ -plane due to the uniquely short probe pulse [see eq. (1.28)]. Simultaneously, sub-10-fs shadowgraphy provides – via density-dependent deflection of the probe beam – insight into the structure of the plasma wave accelerating the electrons.

### 4.2.2 Simulation of the signal via ray-tracing

PIC simulations (sec. 1.11) are used to validate the intended methodology. The simulation parameters were chosen to closely match the experiment (fig. 4.3). Now, the obtained electron density and magnetic field maps of the plasma are used to calculate the expected signals via ray-tracing. Fig. 4.3g shows an electron energy spectrum from the simulation in comparison with a comparable experimental result. Fig. 4.3a plots the simulated electron density distribution inside the plasma as also shown in fig. 1.11. The trapped electron bunch at the rear side of the bubble is clearly discernible and coincides with the increase of the azimuthal magnetic field (peak field strength: 3.8 kT) around the bunch in fig. 4.3b. Some electrons are not in the plotted plane due to transverse oscillations leading to the apparent structure of the bunch in the density plot. The lineout in fig. 4.3c shows that

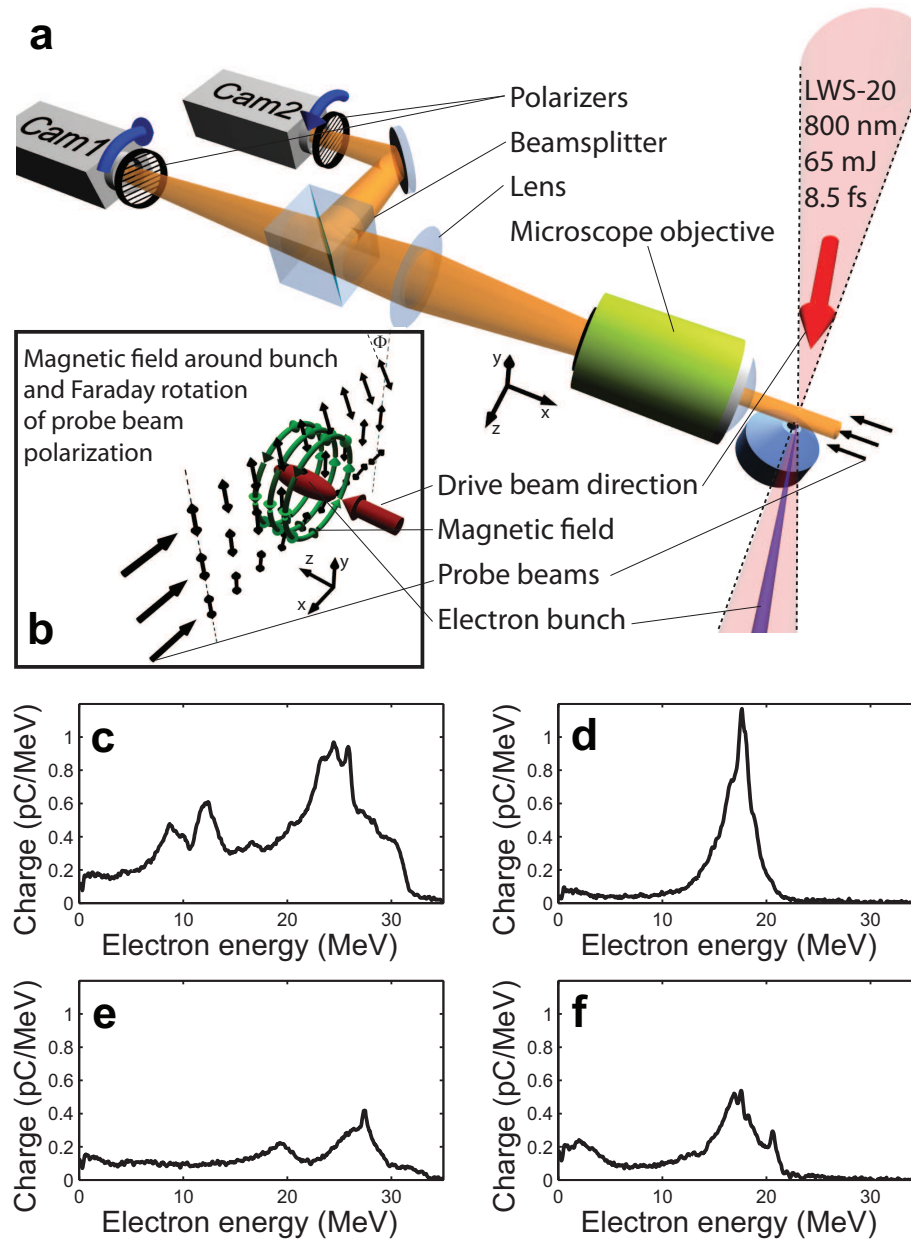


Figure 4.2: **Setup for Faraday rotation and shadowgraphy experiments.** **a**, The ultrashort pulses produced by LWS-20 are focused into a supersonic gas jet with an electron density of  $3.2 \cdot 10^{19} \text{ cm}^{-3}$  produced by a de Laval nozzle with  $300 \mu\text{m}$  exit diameter to generate quasimonochromatic electron bunches. A collimated probe pulse is sent perpendicularly through the plasma to take snapshots of the acceleration process. The interaction region is imaged to two CCD cameras with high resolution. **b**, Illustration of the polarization rotation of the individual rays of the probe beam (black) due to the Faraday effect by the magnetic field (green) of the electron bunch (red). **c-f**, Four electron energy spectra representative for this experimental campaign.

both the electron density and the magnetic field have the same duration of 5.5 fs (FWHM). Thus, the electron bunch duration can be obtained by measuring the longitudinal extent of the magnetic field. Fig. 4.3b also shows an additional magnetic field inside of the bubble which is generated by the displacement current, i.e., the temporally-varying longitudinal electric field. However, this field is by a factor of  $\sim 7$  smaller than the field caused by the moving electrons and has a negligible effect on the polarization rotation. The lineout also shows that another electron bunch is injected into the second plasma oscillation. Due to the much lower charge, its magnetic field is comparable to the one caused by the displacement current and is also negligible here.

The rotation angle of the probe beam polarization  $\varphi_{\text{rot}}$  is simulated by tracking rays of the collimated probe pulse through the three-dimensional arrays of  $n_e$  and  $\mathbf{B}$  obtained from the simulation without taking refraction inside of the plasma into account (fig. 4.3d). The signal is elongated due to several effects. First, the electron bunch is not stationary but propagating further, while the probe beam is traversing the magnetic field of about  $1 \mu\text{m}$  diameter. This is intrinsically included in the raytracing code. Secondly, limited spatial imaging resolution is taken into account by convolving the simulated signal with a 2D-Gaussian profile of  $2 \mu\text{m}$ . The probe pulse duration of 8 fs (FWHM) ( $2.4 \mu\text{m}$ ) is incorporated similarly by smoothing the profile longitudinally with the corresponding Gaussian profile. All these effects are already included in fig. 4.3d. The longitudinal extension of the regions with positive and negative rotation angle is  $3.8 \mu\text{m}$  (12.7 fs) (FWHM).

While the individual rays of the probe beam traverse the plasma, they are deflected at the gradient of the refractive index. This process is illustrated in fig. 4.3e. The deflection is the strongest at the regions of the high density gradient in the plasma wave. Effectively, this leads to an intensity modulation of the probe beam in the plane at the center of the plasma wave with the same periodicity. Imaging this plane to a camera with a high resolution and thus small depth-of-focus in turn shows the modulation as shadowgram of the plasma wave on the camera. The modulation is not averaged out because the probe pulse duration is significantly shorter than the plasma period and the depth-of-focus is comparable to the transverse size of the plasma wave. The deflection of the rays of the collimated probe beam is calculated in the ray-tracing algorithm in the plane including the center of the plasma wave for each propagation step by application of eq. (1.31). A lineout of the modulated intensity is shown in fig. 4.3f. The modulation depth is proportional to the amplitude of the nonlinear plasma wave. Certainly, as the lineout in fig. 4.3g indicates, the measured oscillations are smoothed due to limited resolution and do not reflect the strong nonlinearity of the real plasma wave. However, they still reflect its original period and position. It should be pointed out that the positions of the maxima in the lineouts of the shadowgram do not coincide with the maxima in the electron density, but are about  $\lambda_p/4$  ahead. We will later see that this is also the position where the electron bunch is detected.

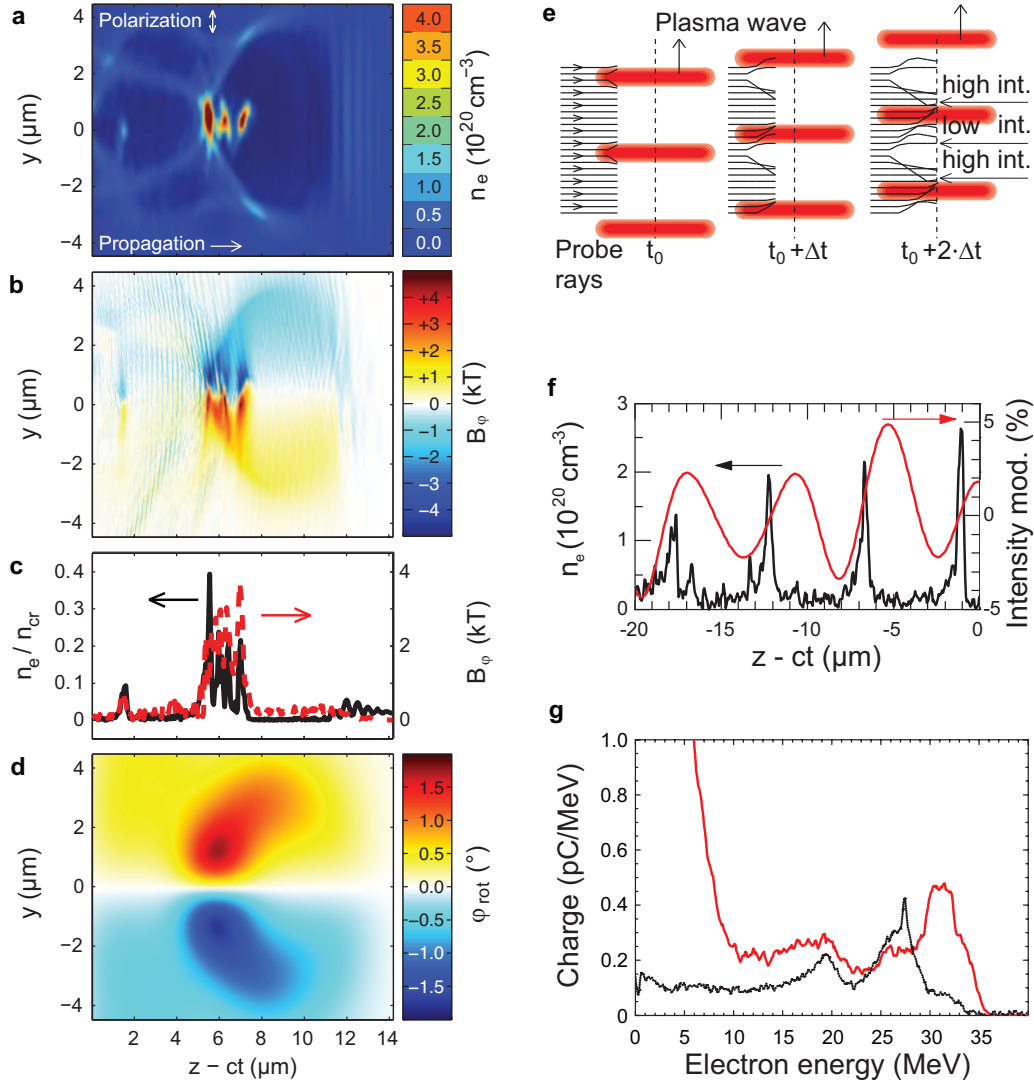


Figure 4.3: **Simulation of the polarimetry and shadowgraphy signal.** The parameters of the PIC simulation have been chosen to closely match the experimental conditions. An 8.0 fs laser pulse (FWHM) is focused to a spot size of  $7.2 \mu\text{m}$  (FWHM), reaching a peak intensity of  $I_{\text{peak}} = 5.8 \cdot 10^{18} \text{ W/cm}^2$ . The focus is located in the center of a  $300 \mu\text{m}$  long flat top density profile with  $n_e = 3.5 \cdot 10^{19} \text{ cm}^{-3}$ . The complete box has an extension of  $48.5 \mu\text{m}$  longitudinally and  $45.2 \mu\text{m}$  transversally. **a**, Electron density map. **b**, Azimuthal magnetic field. **c**, Lineout of the electron density (black solid line) and the magnetic field map (red dashed line). **d**, Simulation of the measured polarization rotation angle. **e**, Illustration of the probe beam (black rays) refraction at the high density peaks of the plasma wave (red) at three instances in time. The probe beam is already refracted in the first half (transversely) of the plasma wave leading to a modulated intensity of the probe beam in the imaged plane (dashed line). **f**, Lineout of the simulated intensity modulation via ray-tracing and the electron density map from the PIC simulation. **g**, Comparison of electron energy spectra obtained at the same time-frame as **a**) and **b**) with a typical experimentally obtained spectrum in this campaign.

The simulated observations of polarimetry and shadowgraphy will now help to interpret the measurements presented in the next sections.

### 4.3 Electron bunch measurements via Faraday rotation

Experimentally, the interaction region is imaged using a combination of a long-working distance plan-apochromatic microscope objective with  $f = 20$  mm (Mitutoyo) and an achromatic lens with  $f = 250$  mm (Thorlabs) as shown in fig. 4.2. The achieved resolution of  $\Delta_{\text{res}} = 2 \mu\text{m}$  was determined by measuring the size of the smallest resolvable structures from the plasma channel as well as testing the imaging system with a resolution target (Edmund Optics). For a sensitive, low-background measurement of  $\varphi_{\text{rot}}$ , the interaction region is imaged simultaneously to two cameras with the help of a non-polarizing beamsplitter cube [54]. Two Glan-laser polarizers with high extinction ratio were placed in front of the CCD cameras. The polarizers were rotated away from extinction of the original probe beam polarization in opposite directions by  $\theta_{\text{pol},i} = \pm(7.0 \pm 0.3)^\circ$ , slightly greater than the expected rotation angles (fig. 4.3d). Thus, the intensity in the images is modulated if the polarization is not uniform and regions with positive polarization rotation appear brighter on one camera than on the other. The measured intensity on the two cameras ( $i = 1, 2$ ) is given by

$$I_{\text{pol},i}(y, z) = I_0(y, z) \cdot T_i \cdot \left[ 1 - \beta_i \cdot \cos^2(\varphi_{\text{rot}}(y, z) - \theta_{\text{pol},i}) \right], \quad (4.1)$$

where  $I_0(y, z)$  is the initial intensity distribution in the collimated probe beam,  $T_i$  the transmission / reflectivity of the beam-splitter, and  $\beta_i = 1 - 1/E_{\text{R},i}$  with  $E_{\text{R},i}$  being the polarization contrast of the beam in the corresponding arm, which is set by the initial laser polarization, the beamsplitter properties, and the polarizer extinction ratio. For this experiment,  $\beta_1 = 0.973 \pm 0.004$  and  $\beta_2 = 0.961 \pm 0.001$  was determined by measuring the transmission of the probe laser as a function of polarizer angle. The rotation angle  $\varphi_{\text{rot}}$  can be deduced by inversion of the intensity ratio of the two images.

$$\frac{I_{\text{pol},1}(y, z)}{I_{\text{pol},2}(y, z)} = \frac{T_1}{T_2} \frac{1 - \beta_1 \cdot \cos^2(\varphi_{\text{rot}}(y, z) - \theta_{\text{pol},1})}{1 - \beta_2 \cdot \cos^2(\varphi_{\text{rot}}(y, z) - \theta_{\text{pol},2})} \quad (4.2)$$

For  $\varphi_{\text{rot}} = 0$ , the equation is simplified to:

$$\frac{I_{\text{pol},1}(y, z)}{I_{\text{pol},2}(y, z)} = \frac{T_1}{T_2} \frac{1 - \beta_1 \cdot \cos^2 \theta_{\text{pol},1}}{1 - \beta_2 \cdot \cos^2 \theta_{\text{pol},2}}. \quad (4.3)$$

Thus, the ratio  $T_1/T_2$  can be determined from the average intensity ratio in the two images without polarization rotation. Returning to eq. (4.2), all parameters are known, and

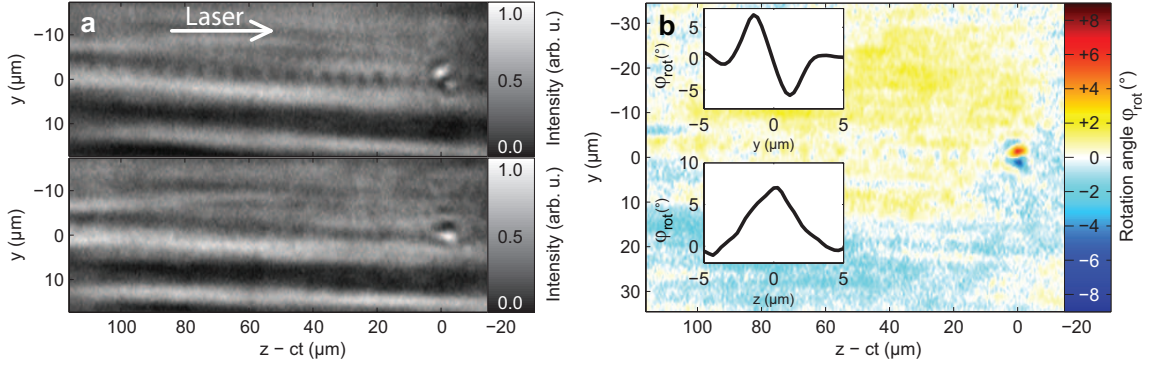


Figure 4.4: **Raw images of the two cameras and evaluated polarization rotation angle.** **a**, Raw images of the same laser shot from camera 1 and 2. While most of the features are the same in both images, the difference at the position of the rotated polarization due to the magnetic field of the electron bunch is clearly visible. **b**, Evaluated image of the rotation angle by division of the two raw images. Upper inset: Vertical lineout. Lower inset: Longitudinal lineout.

$\varphi_{\text{rot}}$  can be calculated by inversion of the formula. For the given experimental parameters, the intensity ratio  $I_{\text{pol},1}(y, z)/I_{\text{pol},2}(y, z)$  as a function of  $\varphi_{\text{rot}}$  is monotonic over a range of  $|\varphi_{\text{rot}}| < 11^\circ$ , which is several degrees larger than the expected rotation angles. Thus, unambiguous numerical inversion to obtain  $\varphi_{\text{rot}}$  from the measured intensity ratio  $I_{\text{pol},1}/I_{\text{pol},2}$  is possible. This method has the advantage of greatly reducing the background, e.g. due to non-homogeneous probe beam profile or intensity modulation due to refraction at the plasma. Additionally, the sign of the polarization rotation can be obtained.

Figure 4.4a shows two raw images from the two cameras for the same laser shot. The most obvious feature in those images are the bright and dark horizontal lines. These lines emerge due to the non-perfect focus of the main beam with scattered laser light far outside the central spot. Thus, an area much larger than the focal spot is (at least partially) ionized. This leads to density modulations which in turn modulate the probe beam intensity due to focusing or defocusing (see also sec. 1.5). Since only regions with rotated polarization are expected to be different in the two raw images due to the different polarizer settings, the horizontal lines are very similar in both images. A signal of rotated polarization is visible at the right hand side of the pictures. While the upper image shows a bright spot above a dark spot, the lower image shows the opposite. This is the expected signal of rotated polarization due to the magnetic field of the electron bunch. It was verified that the signal is indeed originating from polarization rotation by switching the angles of the two polarizers, i.e., tuning polarizer 1 from  $+7^\circ$  to  $-7^\circ$  and vice versa for polarizer 2. In this case the signal was inverted.  $\varphi_{\text{rot}}$  can be quantified by application of eq. (4.2) as shown in fig. 4.4b. All the background features that were visible in the raw images are



now removed and only the rotated polarization stands out from the background. Only one Faraday rotation signal was found in all the images. We see in the figure that the background level is approximately  $\pm 0.5^\circ$ . Thus, a possible second electron bunch in one of the later plasma oscillations, which is also shown by the simulation, is only detected if its charge is more than 10% of the charge of the main electron bunch.

As shown in fig. 4.3, the electron pulse duration can be directly inferred from the polarization rotation signal, which was detected in 85 shots at different positions in the plasma. As we will see in sec. 4.5, the electron bunch duration is constant within the error bars in this range. Averaging all 85 shots like the one in fig. 4.4, the rotation signal appears to have a longitudinal extent of  $\Delta_{\text{rot}} = (3.8 \pm 0.2) \mu\text{m}$  (FWHM), corresponding to a duration  $\tau_{\text{rot}} = \Delta_{\text{rot}}/c$ . This is in excellent agreement with the value obtained from raytracing in fig. 4.3d. As mentioned earlier, several factors have to be taken into account to deconvolve the real electron bunch duration  $\tau_{\text{bunch}}$  from  $\tau_{\text{rot}}$ . The visible signal is elongated due to the limited resolution of imaging system  $\tau_{\text{res}} = \Delta_{\text{res}}/c = 6.7$  fs. Additionally, the probe pulse duration  $\tau_{\text{probe}} = (8.5 \pm 0.5)$  fs and the transverse size of the azimuthal magnetic field (i.e., the transit time of the probe beam through the magnetic field of the electron bunch)  $\tau_{\text{transv}} = \Delta_{\text{transv}}/c = 3.3$  fs have to be considered. The value of  $\tau_{\text{transv}}$  is estimated from the PIC simulation and contributes only marginally to the measured duration of the magnetic field. Thus, the measured rotation signal will have the duration

$$\tau_{\text{rot}} = \sqrt{\tau_{\text{bunch}}^2 + \tau_{\text{res}}^2 + \tau_{\text{probe}}^2 + \tau_{\text{transv}}^2} \quad (4.4)$$

By using the above equation to deconvolve  $\tau_{\text{rot}}$  a mean FWHM electron pulse duration of  $\tau_{\text{bunch}} = 5.8^{+1.9}_{-2.1}$  fs ( $2.5^{+0.8}_{-0.9}$  fs root mean square) is obtained. The non-symmetric error of the electron pulse duration was calculated statistically using distribution functions for the four main parameters ( $\tau_{\text{rot}}$ ,  $\tau_{\text{probe}}$ ,  $\tau_{\text{transv}}$ ,  $\tau_{\text{res}}$ ). The properties of these distributions were determined from the measurement. Calculating the deconvolution for each data set gives the statistical distribution, and thus the mean and the standard error, of the electron bunch duration.

This obtained bunch duration is in good agreement with the simulated value of 5.5 fs. The simulation shows that contributions to the region of rotated polarization from the electrons constituting the plasma wave at the bubble vertex cannot be neglected. Consequently, the actual bunch duration is expected to be even shorter than the result of our above analysis. This is in agreement with the slightly smaller value of 1.4 – 1.8 fs RMS, which was measured indirectly via transition radiation, as reported by Lundh et al. [50].

Since  $\varphi_{\text{rot}}$  depends directly on the magnitude of the magnetic field, it is expected to show a direct dependence on the accelerated charge for each shot. However, a thorough evaluation is difficult since the polarization rotation signal as well as the electron energy spectrum are not detected in every shot. Fluctuations in the electron beam pointing cause

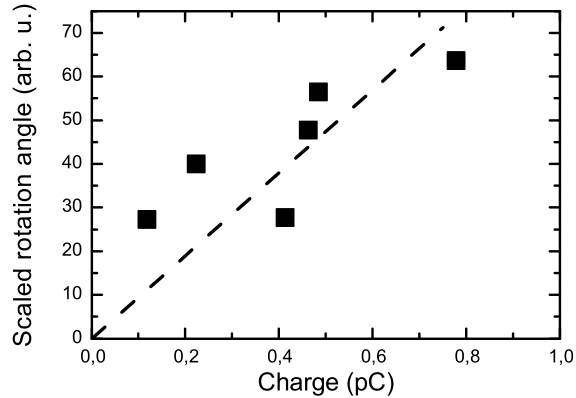


Figure 4.5: **Scaled polarization rotation angle vs. charge.** The rotation angle multiplied with the longitudinal extent of the polarization rotation region is plotted vs. the charge in the peak of the electron energy spectrum detected on the scintillating screen. The dashed line is a guide to the eye for the expected linear behaviour.

the electrons to hit the electron spectrometer only partially or not at all in some of the shots, preventing a precise charge evaluation in these cases. Additionally, due to pointing instabilities of the laser focus, the position of the channel and thus the accelerated electron bunch jitters transversely. Thus, the Faraday rotation signal is not always perfectly inside of the short depth-of-focus of the imaging system and not always detected. If the rotation signal is only slightly out of focus – but still detected – the rotation signal is smeared out, thus increasing the spatial extent, but reducing the maximum rotation angle. Fig. 4.5 shows the rotation angle multiplied with the longitudinal width vs. accelerated charge (detected in the electron spectrometer) of only those shots, where both parameters were measured correctly. The plot confirms the expected dependence of rotation angle and accelerated charge. The lower measurement limit seems to be around 0.1 pC.

#### 4.4 Plasma wave measurements via shadowgraphy

The plasma wave trailing the laser pulse and the electron bunch – visualised by shadowgraphy – is detected to the left of the region with rotated polarization in the raw images (fig. 4.6a-b) as expected from the ray-tracing evaluation. Typically, around 10 - 20 periods are visible. The strong non-linearity of the plasma wave is not reflected due to the limited resolution, however the position, length, and periodicity of the plasma wave are seen. From this large number of plasma oscillations, we learn that the plasma wave does not decay completely already after the first wake. This indicates that the wake is not heavily

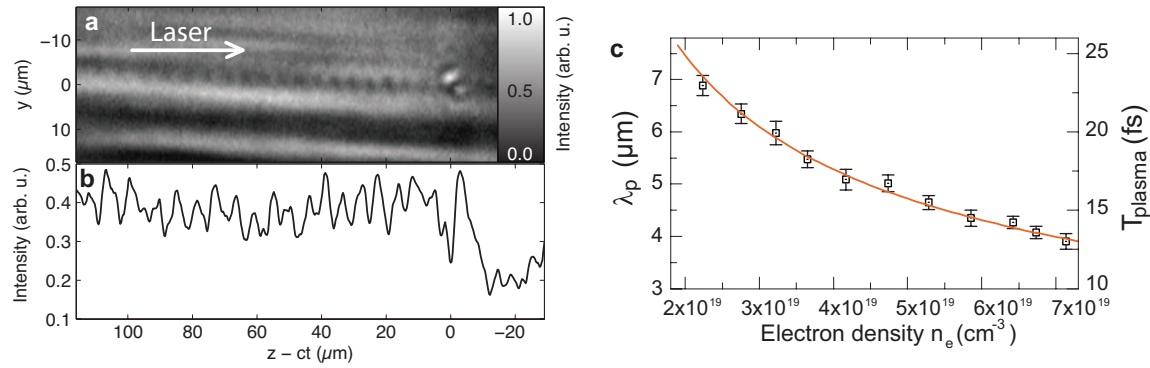


Figure 4.6: **Plasma wave observation via shadowgraphy.** **a**, The plasma wave is visible in the raw image of camera 1 as periodic intensity modulation behind (left) of the signal from the electron bunch. **b**, Lineout of the plasma wave in **a**. **c**, Plasma period vs. electron density. The red line shows the theoretical, non-relativistic plasma period (eq. (4.5)).

loaded as seen by Rechatin et al. [90], since this would lead to rapid destruction of the subsequent plasma oscillations. To obtain firm evidence for the origin of the observed oscillations, their period as a function of electron density was measured, while all other experimental parameters were kept constant (fig. 4.6c). The period of the plasma wave  $T_{\text{plasma}}$  is calculated from the plasma frequency in the non-relativistic limit given in eq. (1.20).

$$T_{\text{plasma}} = 2\pi \sqrt{\frac{\epsilon_0 m_e}{e^2 n_e}} \quad (4.5)$$

The good agreement of the time-resolved plasma oscillation period with the theory corroborates that the oscillations originate from the plasma wave and reveal that the period is not significantly elongated due to relativistic effects under our experimental conditions as also seen by Matsuoka et al. [143]. This observation is in agreement with results of the PIC simulations which predict that the plasma period depends only weakly on the laser intensity (at least) up to an initial normalized vector potential of  $a_0 = 2.1$ .

The observation of the plasma wave can also be used to measure the density ratio at the shockfronts, which were used to generate stable electron injection into wakefields in the previous chapter. Fig. 4.7 shows a raw image of a shockfront experiment, where the plasma wave is visible before and after the shock. In this run, a ratio of 1.30 is measured for the plasma period, corresponding to a density step of 1.69. According to eq. (2.7), the density ratio only depends on the shock angle  $\alpha$  and the Mach number  $M_1$  of the supersonic nozzle. Here, the angle can be measured very accurately to  $\alpha = 18.8^\circ$ . This results in  $M_1 = 4.6$ , which is in good agreement with the simulated value of  $M_1 \approx 5$  [122].

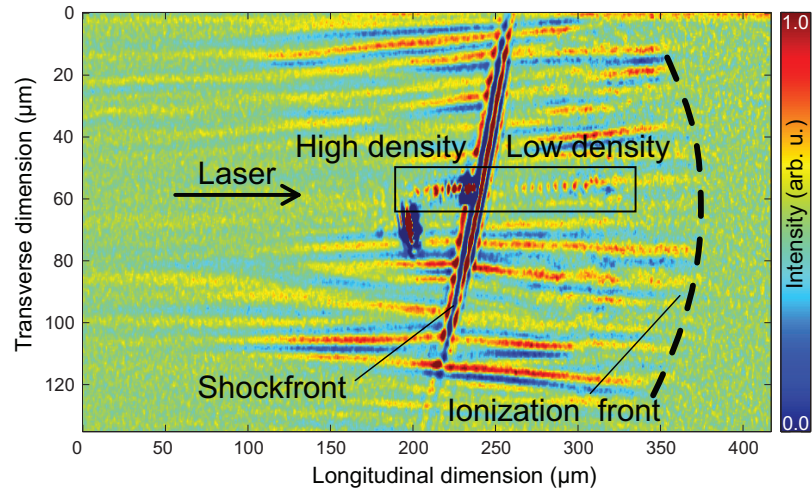


Figure 4.7: **Shadowgram of the shockfront.** The laser pulse is ionizing the gas and exciting the plasma wave. The laser pulse and the accelerated electrons are about  $60 \mu\text{m}$  ( $200 \text{ fs}$ ) behind the ionization front. This value is in agreement with the measured laser contrast curves and the threshold for ionization (tab. 1.1). The distance between first and second ionization front is expected to be  $20 \mu\text{m}$ , thus they are not distinguishable and only one ionization front is visible. The black box marks the visible plasma oscillations. The first few periods are already in the low density part (right of the shockfront), the tail of the plasma wave is still in the high density part (left of the shockfront), where it has a shorter wavelength. The background in the image has been partially subtracted to enhance the visibility of the plasma oscillations.

## 4.5 Snapshots of LWFA via the combination of polarimetry and shadowgraphy

The combination of the two techniques – polarimetry and shadowgraphy – to detect the electron bunch as well as the plasma wave is capable of revealing interesting properties of the acceleration process. By scanning the delay between the drive beam and the probe pulse, snapshots are taken at different stages of the acceleration. A series of snapshots at different delays is shown in fig. 4.8. Plotted is the lineout of the plasma wave shadowgram as well as the position and duration of the detected electron bunch, with the latter inferred from the time-resolved polarimetry data under the assumption of a Gaussian temporal shape of the bunch.

The intensity modulation is visible only behind the Faraday rotation signal, except for one maximum caused by the electrons that are being pushed forward by the laser, which can appear in front of the electrons in some shots (for example fig. 4.8e). At the position of the electron bunch, the signal of the rotated polarization is superimposed on the shadowgram in the raw images. Thus, the plasma wave cannot be seen here. However, conclusions can still be drawn because the peak in the lineout at this position agrees with the periodicity of the rest of the plasma wave. This reveals that the accelerated main electron bunch is trapped inside the first plasma wave oscillation, in agreement with our simulation (fig. 4.2a) as well as earlier experiments by Mangles et al. [144]. A small number of electrons can be found in the second period in the simulation, however the order-of-magnitude weaker magnetic field around those electrons is not expected to be above the background noise level in our measurement. No electron bunch is shown in fig. 4.8a, because the polarization rotation signal was not detected at this delay. Since the beam parameters such as number of periods and bunch duration vary strongly from shot to shot, it is helpful to look at the averaged parameters for each delay step.

Figure 4.9 shows this evolution of the different acceleration parameters. The polarization rotation signals are detected for the first time after a laser pulse propagation distance of  $z \approx 190 \mu\text{m}$  in the gas jet (fig. 4.9a). The mean duration of the polarization rotation signal and the deconvolved electron bunch duration are given for each delay step, i.e., each position inside of the plasma. It can be seen that  $\tau_{\text{bunch}}$  is constant within the error bars, showing an upper limit of of 7-8 fs (FWHM). As mentioned earlier, the electron bunch duration could in fact be much shorter, which is not detected because the polarization rotation signal is only slightly longer than the resolution. Also plotted is the peak polarization rotation angle, which is proportional to the beam current (fig. 4.5). The vanishing of  $\varphi_{\text{rot}}$  for  $z < 190 \mu\text{m}$  and its reaching of maximum at about  $z = 210 \mu\text{m}$ , in combination with a nearly constant  $\tau_{\text{bunch}}$ , indicates that injection is confined to a propagation length of about  $20 \mu\text{m}$  approximately  $z = 200 \mu\text{m}$  downstream from the rising edge of the plasma density.

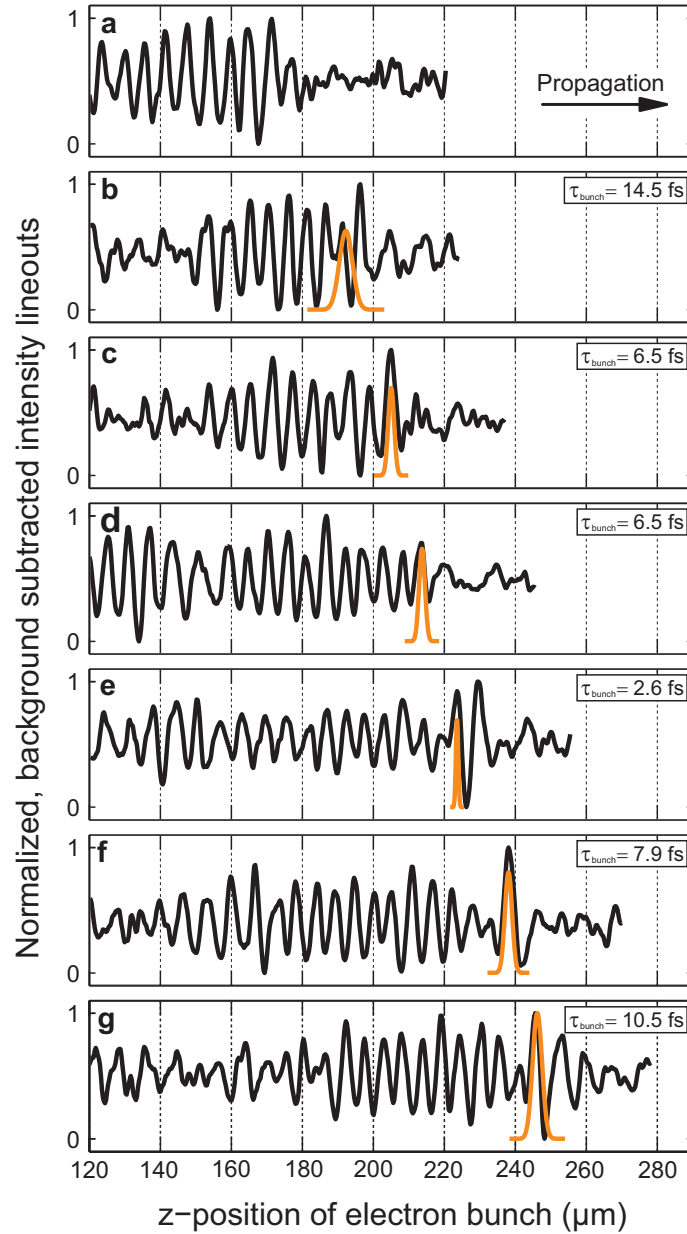


Figure 4.8: **Snapshots of the trapped electrons and the plasma wave.** Shown are normalized lineouts of the plasma wave in the raw images (black line) and the position and duration of the electron bunch assuming a Gaussian shape (orange line) at different time delays between drive pulse and pump pulse. The box gives the deconvolved FWHM bunch duration for each shot. **a**, Lineout of the plasma wave at a delay prior to electron trapping.

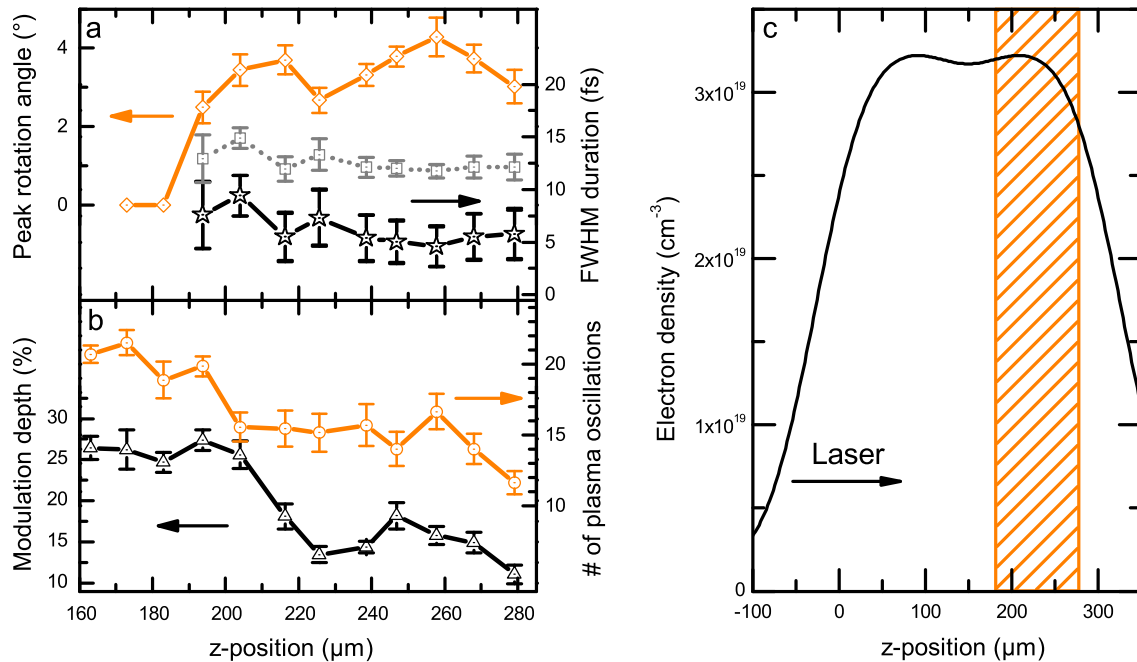


Figure 4.9: **Evolution of the electron bunch duration and the plasma wave during the acceleration process.** **a**, Evolution of the deconvolved FWHM electron pulse duration (black stars), the original duration of the polarization rotation (grey squares), and the peak polarization rotation angle (orange diamonds) during the propagation through the plasma. Each point is an average of 4-22 measurements. **b**, Simultaneous evolution of the number of plasma oscillations (orange circles) and the intensity modulation depth (black triangles) in the shadowgraphy images. The number of plasma oscillations was evaluated by counting by eye the number of visible oscillations in the raw images like fig. 4.6a. The modulation depth is the peak-valley amplitude of the oscillations divided by the average image intensity in this region. Each point is an average of five measurements. Error bars represent 1 s. **d**, **c**, Abel inverted electron density profile. The orange box marks the range where the polarization rotation signal is visible.

These interpretations are supported by the plasma wave dynamics (fig. 4.9b). Over approximately the same longitudinal range as the Faraday rotation signal builds up, the accelerating plasma wave exhibits a decrease in total length, obtained by counting by eye the visible oscillations in the raw images (fig. 4.6a), as well as in its amplitude, which is proportional to the modulation depth of the probe intensity variations. This reduction in plasma wave amplitude is caused by the injected and accelerated electrons that are not located at the regions of high electron density in the plasma wave but in the accelerating phase of the plasma wave. Thus, these electrons do not contribute to the longitudinal electric field but in contrast damp it [90].

The Faraday rotation signal is lost abruptly for  $z > 280 \mu\text{m}$ . This can be understood via comparison with the longitudinal electron density profile of the gas jet (fig. 4.9c). At this position, the density decreases rapidly. Thus, also the medium to perform the polarization rotation drops quickly, reducing the polarization rotation even though the magnetic field of the accelerated electrons is still present. Since the density drops, also the acceleration is expected to terminate soon after, resulting in an acceleration length of approximately  $100 \mu\text{m}$ . Together with the mean peak energy of  $\approx 20 \text{ MeV}$ , an acceleration gradient of  $\approx 200 \text{ GV/m}$  is estimated. This is in agreement with the findings of the previous chapter (fig. 3.5), where a maximum accelerating gradient of  $130 \text{ GV/m}$  was derived for a slightly lower density. The electrons trapped via self-injection typically sit further behind in the bubble compared to the shockfront injected ones, where electrons are injected more into the center. Thus, it is expected that they see a slightly higher accelerating field.



# Chapter 5

## Conclusions

In the framework of this thesis, laser-driven electron acceleration in the LWFA regime has been investigated. The measurements targeted two main areas: the controlled injection of electrons into the laser wakefield and the real-time observation of the acceleration process.

The experiments on controlled injection have been presented in chapter 3. Here, the two major aspects have been the demonstration of this new method of electron injection and the study of several fundamental properties of laser wakefield acceleration using the greatly improved electron beam quality. First, it was shown that after doubling the energy of LWS-20 (65-75 mJ, 8 fs) compared to LWS-10 used by Schmid [122] the electron energy of the electrons via self-injection was improved from 50 MeV to 75 MeV, or from 8-15 MeV to 20-30 MeV in the more stable runs. However, the parameters still showed strong fluctuations, motivating the implementation of an injection mechanism.

Therefore, a novel technique, the injection at a sharp density transition, has been investigated. In this new scheme, instabilities in the acceleration with LWS-20 were significantly reduced because of the lower sensitivity of the density transition injection to the laser parameters and the laser pulse evolution inside of the plasma. Tunable electrons in the range of 10-30 MeV were accelerated in a very reproducible way. It was also shown that the so-called shockfront injection not only increased the injection probability, but also improved the beam quality, especially reducing the energy spread significantly.

One of the major results obtained with LWS-10 (35-40 mJ, 8fs) in the self-injection scheme was that virtually no background of low-energy electrons was visible in the energy spectrum down to the measurement limit of 100 keV [57]. Thus, the harmful background x-ray radiation produced due to stopping of the low-energy electrons, which is a typical byproduct of LWFA experiments, was reduced strongly, and future experiments with the electron beam are not disturbed by the dark current. It was shown that this important property was not only maintained but even further improved in the controlled injection

case by reducing the level of background electrons.

The stable electrons enabled us to study several aspects of LWFA. By varying the injection position and injecting the electrons almost into the center of the bubble, the dephasing of electrons with respect to the plasma wave could be studied. In this experiment, a maximum acceleration length of  $300 \mu\text{m}$  was found, which is in good agreement with the theory. Here, the dephasing length was reduced because of the injection at the density transition. Due to the large amount of injected charge, also beamloading effects were visible. At an electron density of  $n_e = 3.1 \cdot 10^{19} \text{ cm}^{-3}$ , the energy spread of the electrons increased for charges  $> 2 \text{ pC}$ , and the maximum energy was reduced by  $1.8 \text{ MeV/pC}$ . Furthermore, electron density scans showed that a minimum density of  $n_e = 1.0 \cdot 10^{19} \text{ cm}^{-3}$  is required for LWS-20 to drive the plasma wave efficiently and a linear dependence of maximum energy gain and electron density was observed.

Experiments with longer laser pulses generated by ATLAS (770 mJ, 26 fs), showed that the injection at the density transition was also applicable to other experimental parameters and improved the electron beam stability. The different shockfront injection runs demonstrated tunability over a wide range of 15-150 MeV and peak charge of up to tens of pC in a high quality peak in the electron energy spectrum. Despite the longer laser pulses, the accelerator showed the same extremely low background as the LWS-20 experiments. A reduction in generated harmful secondary radiation by at least a factor of 3 was observed for controlled injection compared to self-injection.

In the second main part of this thesis (chapter 4), an advanced diagnostic tool for laser wakefield acceleration was presented. With this new method, snapshots of the acceleration process itself were taken, visualizing both the electron bunch and the accelerating plasma waves. This was achieved by using a small fraction of the drive laser pulse (65 mJ, 8 fs) as a probe beam, which was sent perpendicular to the electron propagation direction through the plasma. Here, information about electron bunch and plasma wave was imprinted into the properties of the probe beam by the simultaneous application of time-resolved polarimetry and time-resolved shadowgraphy. The azimuthal magnetic field of the accelerated electrons caused a localized rotation of the probe beam polarization due to the Faraday effect. At the same time, the probe beam intensity was modified due to refraction at the high density gradients of the plasma wave.

Thus, the new technique provided first direct insight into the acceleration process, revealing many important properties of the self-injection mechanism used in these experiments. When focusing LWS-20 into a  $300 \mu\text{m}$  He gas jet, we were able to measure that self-injection of the electron bunch into the plasma wave started after a propagation distance of the laser pulse of  $200 \mu\text{m}$ . The measurements showed that most of the injection is confined to a region of  $20\text{-}30 \mu\text{m}$  around this position.

By measuring the longitudinal extent of the polarization rotation region, the duration

of the electron bunch within the plasma could be calculated because its azimuthal field had the same length as the bunch itself as shown by simulations. We saw that the bunch duration was almost constant during the acceleration. A duration of  $5.8^{+1.9}_{-2.1}$  fs (FWHM) was measured, which confirms the expected ultrashort bunch length. However, as already mentioned, the resolution was very close to this measured value, thus the pulse duration could in fact be shorter and the measurement presents only an upper limit.

In contrast to earlier measurements of the plasma wave in a time-integrating scheme by Matlis et al. [51], our technique revealed dynamical effects. Shortly after the electron bunch was injected, the plasma wave amplitude decreased, which was expected due to the injected electrons damping the wave. Additionally, we observed a shortening of the wave, i.e., a reduction in number of plasma oscillations. It should be pointed out, however, that many plasma oscillations were visible in all cases, suggesting that the experimental parameters were still far away from the "true" bubble-regime, the strongly nonlinear LWFA regime, where only one plasma oscillation should have survived. Even though the plasma wave consisted of many oscillations, the electron bunch was found in the first period. As shown in chapter 4, shadowgraphy could also be applied to other experimental settings. To this end, it was used to measure the ratio of the plasma wavelength before and after the density jump of the shockfront. Thus, the combination of the two time-resolved measurements was an invaluable diagnostic tool for the laser wakefield acceleration experiments and will strongly enhance further understanding of future measurements.



# Chapter 6

## Outlook

In chapter 3, results on self-injection with LWS-20 were presented. The accelerator showed improved quality compared to the older LWS-10 results, however the accelerator stability was not yet in the necessary range for first applications of the electron bunches. For the envisaged ultrafast electron diffraction (UED), stable electrons with lower peak energy are required. The threshold for the "true" bubble regime ( $a_0 > 4$ ) could be overcome significantly upon completion of the current upgrade of LWS-20 to even shorter pulse duration of only two optical cycles ( $\approx 5.0$  fs) with equal pulse energy ( $\approx 100$  mJ). In the expected parameter regime, the acceleration length will be extremely short, opening up the path for stable electron acceleration in the few-MeV range.

While the ultrashort, low energy electron bunches produced with LWS-20 are intended for time-resolved experiments, the ATLAS electrons are envisaged for secondary x-ray sources. One route for narrow-band, soft-x-ray radiation is the generation of undulator radiation by high energy electrons as reported by Fuchs et al. [32]. First experiments on controlled density transition injection performed with the upgraded ATLAS system showed tunability of the peak energy up to 200 MeV (fig. 6.1), however due to radiation protection restrictions higher energies were not produced. Preparations are currently under way to repeat the experiments in a different setup, where the necessary electron bunches of several 100 MeV could be produced.

Electron bunches with moderate energy are desired for Thomson backscattering experiments. Here, a second laser pulse is reflected from the accelerated electrons. Due to the relativistic motion of this "electron mirror", the initial photon energy is Doppler upshifted approximately by  $4\gamma^2$  of the electron bunch. Thus, the electron bunches should have an energy around 50 MeV to reach photon energies in the hard x-ray regime on the order of 50 keV. Preliminary experiments with the upgraded ATLAS laser have shown that with careful tuning of all parameters stable electron bunches with up to 100 pC on average can

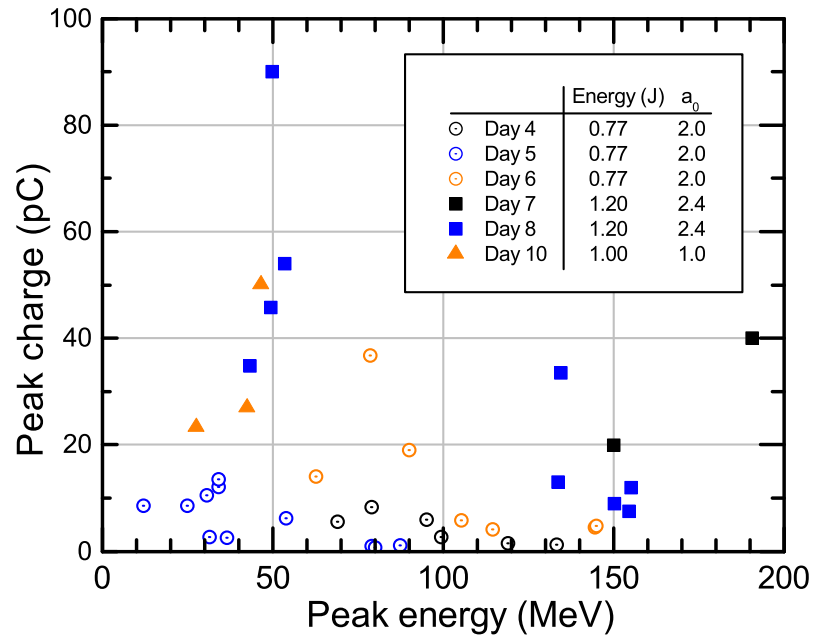


Figure 6.1: **Overview over mean energy and charge of the peak in the electron energy spectrum of all stable runs with ATLAS.** The open circles represent electron runs performed before the ATLAS upgrade as also presented in chapter 3. The closed symbols represent measurements performed after the upgrade in two different focusing geometries.

be accelerated at this energy range (fig. 6.1). These bunch charges are a factor of 5-10 higher compared to the results obtained with ATLAS before the upgrade. Preparations to split the ATLAS pulses and use one part for the Thomson backscattering experiments are currently under way due to these promising results.

The future also looks bright for the advanced diagnostic tools of LWFA developed in this thesis. While an ultrashort pulse duration ( $\leq 10$  fs) is desired for time-resolved polarimetry to detect the electron bunch and to measure its duration inside of the plasma, shadowgrams of the plasma wave are also possible with the more common Ti:sapphire lasers with pulse durations of 20-40 fs. The plasma wavelength for the typical operation conditions scales with the laser pulse duration, thus shadowgraphy is also possible with these systems if the good spatial resolution is maintained. Here, dynamic effects in plasma wave amplitude and oscillation number, and also possible relativistic elongation effects could be measured. In a more complicated setup, the probe beam could be spectrally broadened in a Ne-filled hollow core fiber and compressed down to few-fs duration. Thus, the electron bunch duration measurement could also be performed with these longer pulses.

The polarimetry and shadowgraphy measurements with LWS-20 will strongly benefit from the current laser upgrade. By reducing the pulse duration to 5.0 fs and optimizing the imaging optics, the longitudinal resolution, i.e., the combination of spatial resolution and probe pulse duration, could be reduced from 3.2 to 2.0  $\mu\text{m}$ . Thus, more precise measurements of the electron bunch duration and the plasma wave will be possible, potentially revealing more dynamical effects and structure of the electron bunch and the plasma wave. This will enable a more detailed investigation of the injection process and will allow for further benchmarking of simulation codes.

Time-resolved polarimetry and shadowgraphy will also enable more detailed studies of other injection schemes, e.g. density transition injection, ionization-induced injection, or colliding pulse injection (sec. 1.10). For example, it was shown already in chapter 4 that the plasma wave can be diagnosed before and after the density transition. In a preliminary experiment the time-resolved polarimetry technique has also been applied to a density transition experiments. The visibility and evolution of the electron beam parameters are shown in fig. 6.2. We see that the bunch duration is constant throughout the acceleration process and has a similar value compared to the self-injection results. It is interesting to note that electrons are detected only about 30-50  $\mu\text{m}$  after the shock. During propagation and acceleration, the polarization rotation signal seems to decrease with position and vanishes completely after a propagation of slightly more than 100  $\mu\text{m}$  after the shockfront. This is explained by the decreasing density inside of the bubble. These preliminary results and future experiments with this advanced diagnostic will greatly enhance our understanding of the laser wakefield acceleration and the injection process.

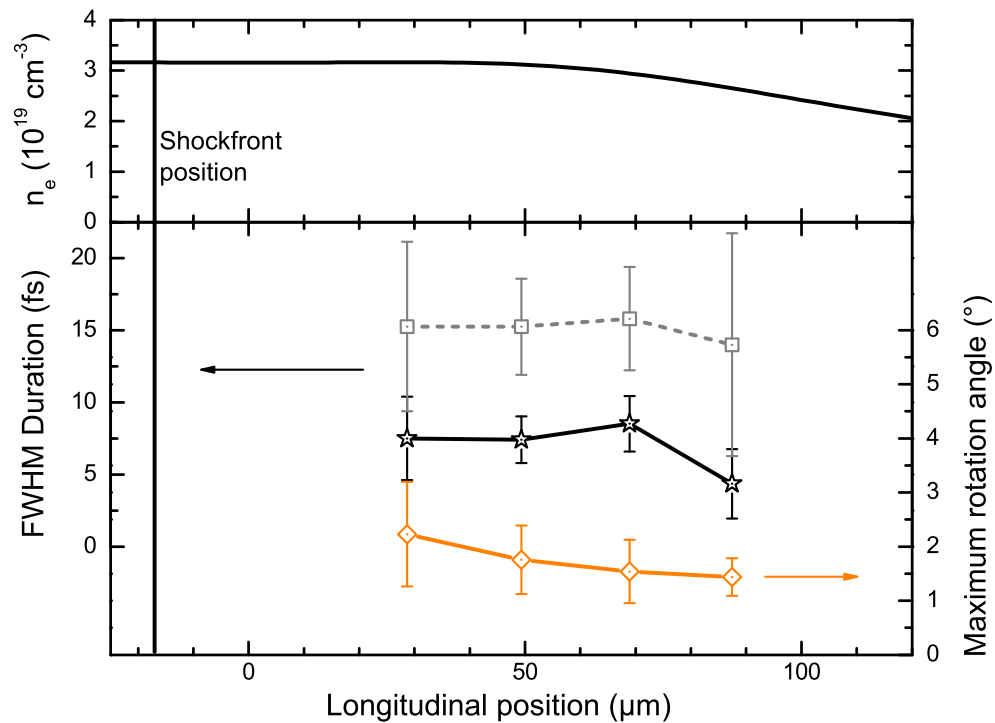


Figure 6.2: **Evolution of the electron bunch parameters during the acceleration process with controlled injection.** The vertical black line marks the position of the shockfront and thus the electron trapping. The upper panel shows the undisturbed electron density profile obtained via interferometry. Due to the density jump at the shockfront, the electron density to the left of the black line is in fact higher. The lower panel shows the evolution of the duration of the polarization rotation signal (grey), the deconvolved electron bunch duration (black), and the maximum rotation angle (orange) during the acceleration process.



# Appendix A

## Cross-Polarized Wave Generation (XPW)

Pulse contrast, i.e., the ratio of the intensity at a given time instant before the peak and the pulse's peak intensity, is an important property of high-intensity laser systems. The ultrashort laser pulses on the fs-timescale generated by state-of-the-art laser systems typically have a background with lower intensity on the ps- to ns-timescale. This background is often composed of a ns-pedestal due to amplified spontaneous emission (ASE), pre- and postpulses (e.g. due to internal reflections in one of the optics), and a pedestal on the few-ps timescale due to imperfect compression. Owing to the high intensity of those laser pulses in the  $10^{18} - 10^{19}$  W/cm<sup>2</sup> range, even a pulse preceding background, which is 6-7 orders of magnitude less intense than the main pulse, can lead to ionization of the target. This is especially important for laser interactions with solid targets, because here the pre-plasma expands due to the pulse background leading to a significantly increased plasma scale length before the arrival of the main pulse, which is altering or completely inhibiting the desired interaction process with the surface. Thus, contrast enhancement is very important for high-intensity laser systems. To this end, several methods have been developed, of which the most common ones are plasma mirrors [59, 145] and cross-polarized wave generation [146, 147].

In a plasma mirror (PM) setup, the output pulses of a laser are focused onto a target with antireflex (AR) coating. The peak intensity in the laser spot is chosen such that the pulse-preceding background is transmitted, but the leading foot of the main pulse creates a plasma with high reflectivity ( $\approx 75\%$ ), thus the contrast of the reflected laser pulse is improved by the ratio between the reflectivity of the AR coating and the peak reflectivity. While this method can improve the contrast by 2-3 orders of magnitude, it has the disadvantage that a significant amount of the laser pulse energy is lost in the reflection

at the plasma surface.

This energy loss is particularly unfavorable for LWS-20, because the on-target laser pulse energy is already very small ( $< 100$  mJ). This problem can be overcome by using crossed-polarized wave generation (XPW) instead of the PM. In contrast to the PM, XPW is a technique that works at lower intensities ( $10^{12} - 10^{13}$  W/cm<sup>2</sup>), thus it can be implemented before the main amplification stages, which are compensating the energy loss. However, pulse compression is needed for XPW. Here, the laser pulses are focused into a crystal with isotropic linear susceptibility but large third-order nonlinearity  $\chi^{(3)}(\omega; \omega, -\omega, \omega)$  (typically BaF<sub>2</sub>). If the crystal is tuned to the correct angle, the laser pulse is converted to the perpendicular polarization at the same frequency in a four-wave mixing process ( $\omega + \omega - \omega = \omega$ ) with an efficiency of up to 10-20 %. Due to the third-order dependence on the intensity of the process, the main laser pulse is converted much more efficiently than the weak background. The new pulse with perpendicular polarization and enhanced contrast has to be separated from the incident laser pulse. To this end, crossed polarizers are placed before and after the crystal to clean the input polarization and transmit only the converted part afterwards. The final output contrast  $C_{\text{out}}$  with  $C = I_{\text{background}}/I_{\text{peak}}$  is calculated by

$$C_{\text{out}} \approx C_{\text{in}}^3 + C_{\text{in}} \cdot R, \quad (\text{A.1})$$

where  $R$  is the extinction ratio of the two polarizers. We see that the contrast enhancement is usually limited by  $R \approx 10^{-4} - 10^{-5}$  for a typical input contrast of  $C_{\text{in}} \approx 10^{-7}$ .

The XPW setup implemented in LWS-20 is shown in fig. A.1 (compare also to fig. 2.2 with the complete LWS-20 setup). Before the hollow core fiber (HCF) output pulses are sent to the crystal they have to be compressed to the Fourier-limit to achieve good conversion efficiency and convert the complete spectrum. To this end, the pulses are over-compressed by 16 reflections on double-angle chirped mirrors [148]. This compression also accounts for the propagation in air and the thin, linear polarizer (LPVIS100, Thorlabs) used to clean the input polarization. The final compression down to  $\approx 6$  fs is achieved with a 4.5 mm fused silica plate. The compressed pulses with a remaining energy of 140  $\mu\text{J}$  are sent through a telescope, which is slightly detuned to focus the pulses to a spot size of around 500  $\mu\text{m}$  FWHM on the crystal. Thus, the right intensity of  $\approx 5 \cdot 10^{12}$  W/cm<sup>2</sup> is reached. Here, a BaF<sub>2</sub> crystal with 2 mm thickness and the holographic [011]-cut yielded the best results [149]. Typically, internal conversion efficiencies of 15-20 % are achieved. The converted pulses are separated from the unconverted fundamental pulses with a Glan-Laser polarizer with high extinction ratio. Since the laser pulses are focused into the nonlinear crystal for conversion, XPW also acts as a spatial filter. Thus, a high quality output profile is observed (fig. A.1), which is significantly cleaned compared to the HCF output profile with its ring around the main spot. Additionally, the spectral phase of the

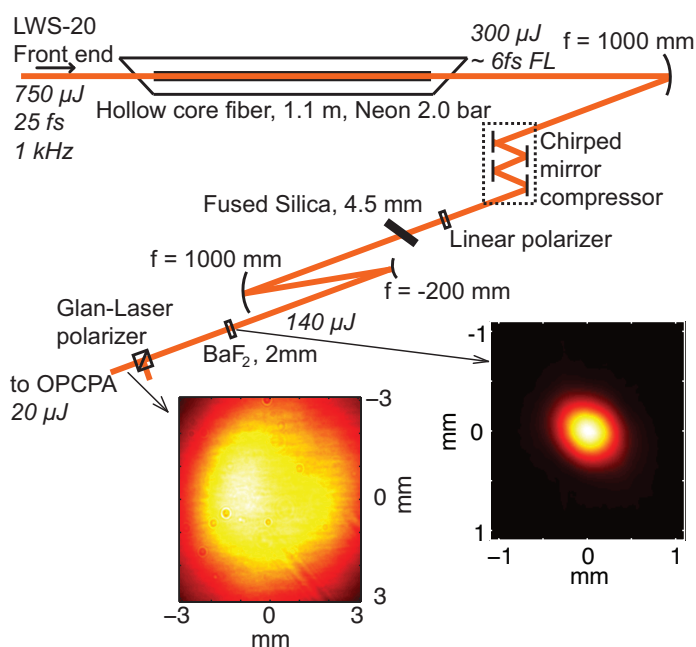


Figure A.1: **Cross-polarized wave generation setup.** The pulses from the front end of LWS-20 with  $750 \mu\text{J}$  are focused into a Neon filled hollow core fiber, where the spectrum is broadened to support pulse durations of 5.5 - 6 fs. Subsequently, the pulses are compressed by 16 double-angle chirped mirror reflections, the linear polarizer and a fused silica glass plate at Brewster's angle. The Fourier-limited pulses are sent into the 2 mm  $\text{BaF}_2$  crystal. A telescope is used to focus the pulses to a large spot size of  $500 \mu\text{m}$  (right inset). After conversion, the initial pulse and the converted part are separated by a Glan-Laser polarizer. The pulses with the enhanced contrast are sent to the stretcher and the OPCPA stages for final amplification (fig. 2.2).

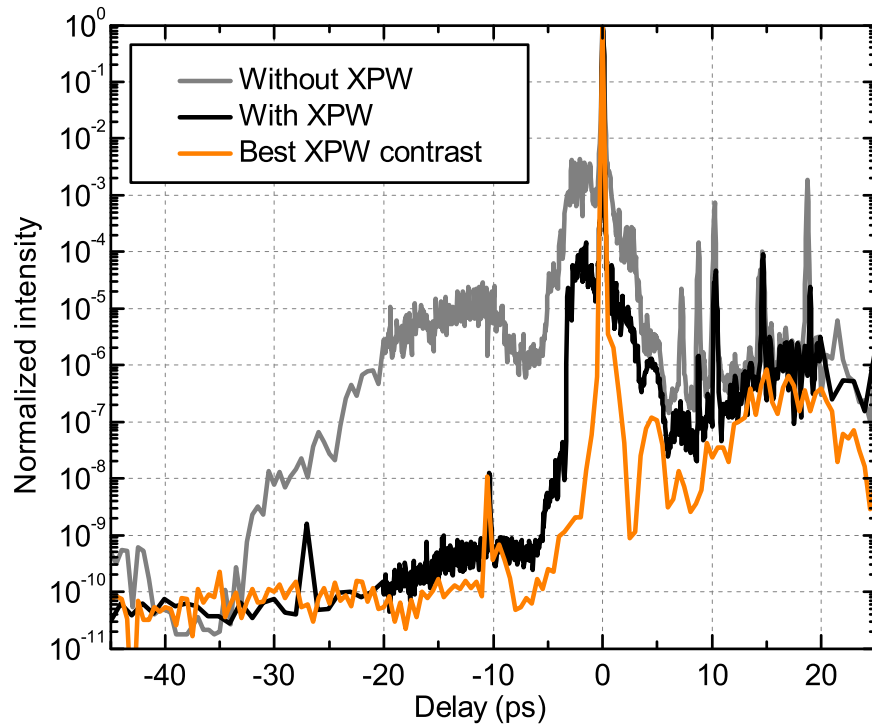


Figure A.2: **Contrast enhancement of LWS-20 with XPW.** The grey and black curve show contrast measurements with and without implemented XPW on the same measurement day. The contrast is improved by up to 4.5 orders of magnitude around 20 ps before the pulse. The signal is below the detection threshold outside of the OPCPA pump window, the same improvement is expected there. The orange curve shows the best contrast measured with XPW with optimum input contrast from the front end. The prepulse at -10 ps is a measurement artefact of the postpulse at +10 ps with higher intensity.

pulses is also smoothed by the XPW process eventually leading to an improved temporal pulse shape [150].

The output pulses are then sent to the stretcher and subsequently to the two OPCPA stages for amplification to the >100 mJ level. Figure A.2 shows the contrast of the LWS-20 after amplification measured with a home-built third-order autocorrelator with high dynamic range [151]. The laser pulse contrast in the 10 - 30 ps (before the pulse) range is improved by 4.5 orders of magnitude as expected from eq. (A.1). For this measurement, the contrast of the front end was deliberately decreased to show the XPW improvement. The ns-pedestal coming from ASE in the front end is only visible in the  $\pm 40$  ps window due to the OPCPA pump duration of 80 ps. Thus, the ns-background is expected to be

---

$10^{-10} - 10^{-11}$  outside of this window without improvement by the XPW in the presented measurement. For optimum laser operations, this expected to be around  $10^{-13}$ . A contrast of 10 orders of magnitude already 5 ps before the pulse was achieved under these conditions with XPW (orange curve). The complete XPW setup has a throughput around 7 %, which significantly lowers the input energy for the OPCPA. This could lead to an increased level of superfluorescence, i.e., the analogue to ASE in OPA. During the measurements, this increased superfluorescence level was not detected, thus the seed energy was still high enough for good OPCPA operation.

When using XPW with longer laser pulses and narrower spectrum, the pulses can be shortened by a factor of  $\sqrt{3}$ , if they are compressed to the Fourier limit upon entering the crystal. Naturally, this shortening will lead to a broadening of the spectrum. When using short pulses with sub-10-fs, spectral broadening is less efficient because already short propagation inside of the crystal leads to a significant elongation of the pulse. It was found in the experiment that a crystal thickness of 2 mm is a good trade-off between conversion efficiency and spectral broadening (fig. A.3). This spectral broadening will be beneficial for the current upgrade of LWS-20 to around 5.0 fs, where a spectral range of 580 - 1000 nm is amplified in the subsequent OPCPA stages.

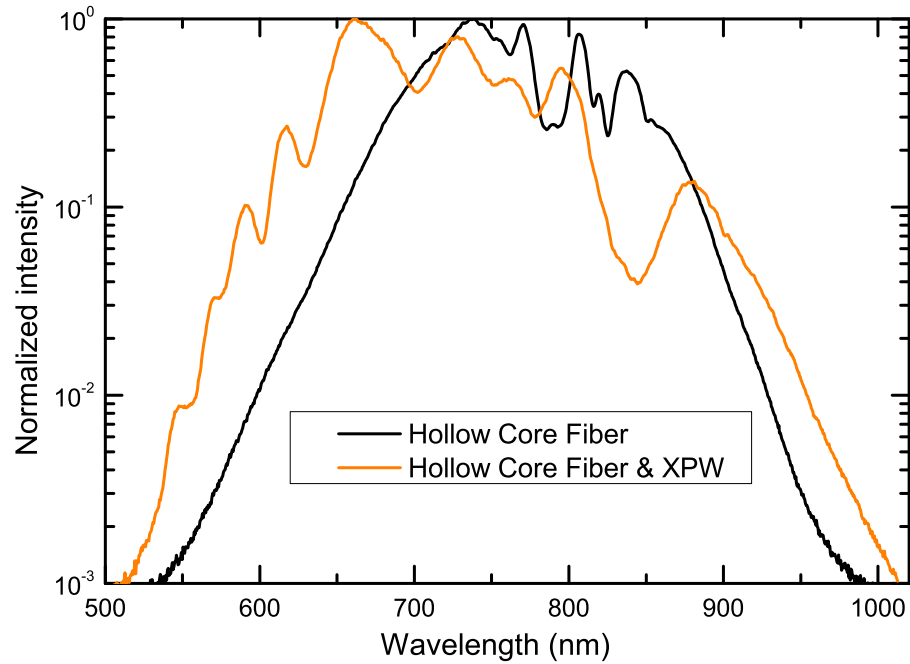


Figure A.3: **Spectral broadening by cross-polarized wave generation.** Shown is a comparison between the initial spectrum of the hollow core fiber output and the spectrum of the perpendicularly polarized pulse measured after the second polarizer. Spectral components have been added on both sides due to the nonlinear process, increasing the available signal for broadband amplification in the two OPA stages.

# Bibliography

- [1] J. D. Cockcroft and E. T. S. Walton. Experiments with high velocity positive ions. ii. The disintegration of elements by high velocity protons. *Proc. R. Soc. Lond. A*, 137:229–242, 1932.
- [2] L. Evans and P. Bryant. LHC machine, 2008.
- [3] A. W. Chao and M. Tigner. *Handbook of Accelerator Physics and Engineering*. World Scientific Pub. Co., 1998.
- [4] SSC – The Superconducting Super Collider Project. URL <http://www.hep.net/ssc/>. Downloaded 20 July 2011.
- [5] J. Mervis and C. Seife. Lots of reasons, but few lessons. *Science*, 302(5642):38–40, 2003.
- [6] A. Cho. International team releases design, cost for next great particle smasher. *Science*, 315(5813):746, 2007.
- [7] M. Spira, A. Djouadi, D. Graudenz, and R. M. Zerwas. Higgs boson production at the LHC. *Nuclear Physics B*, 453(1-2):17–82, 1995.
- [8] D. A. G. Deacon, L. R. Elias, J. M. J. Madey, G. J. Ramian, H. A. Schwettman, and T. I. Smith. First operation of a free-electron laser. *Phys. Rev. Lett.*, 38(16):892–, 1977.
- [9] H. Eickhoff, R. Bär, A. Dolinskii, Th. Haberer, B. Schlitt, P. Spiller, U. Weinreich, and the GSI Therapy Project Group. HICAT - the german hospital-based light ion cancer therapy project. In *Proceedings of the 2003 Particle Accelerator Conference*, 2003.
- [10] A. I. Akhiezer and R. V. Polovin. Theory of wave motion of an electron plasma. *Soviet Physics, JETP*, 3:696, 1956.

- 
- [11] T. Tajima and J. M. Dawson. Laser electron accelerator. *Phys. Rev. Lett.*, 43(4): 267–, 1979.
- [12] P. Chen, J. M. Dawson, R. W. Huff, and T. Katsouleas. Acceleration of electrons by the interaction of a bunched electron beam with a plasma. *Phys. Rev. Lett.*, 54(7): 693–, 1985.
- [13] J. B. Rosenzweig. Nonlinear plasma dynamics in the plasma wake-field accelerator. *Phys. Rev. Lett.*, 58(6):555–, 1987.
- [14] J. B. Rosenzweig, D. B. Cline, B. Cole, H. Figueroa, W. Gai, R. Konecny, J. Norem, P. Schoessow, and J. Simpson. Experimental observation of plasma wake-field acceleration. *Phys. Rev. Lett.*, 61(1):98–, 1988.
- [15] I. Blumenfeld, C. E. Clayton, F.-J. Decker, M. J. Hogan, C. Huang, R. Ischebeck, R. Iverson, C. Joshi, T. Katsouleas, N. Kirby, W. Lu, K. A. Marsh, W. B. Mori, P. Muggli, E. Oz, R. H. Siemann, D. Walz, and M. Zhou. Energy doubling of 42 GeV electrons in a metre-scale plasma wakefield accelerator. *Nature*, 445(7129): 741–744, 2007.
- [16] M. Everett, A. Lal, D. Gordon, C. E. Clayton, K. A. Marsh, and C. Joshi. Trapped electron acceleration by a laser-driven relativistic plasma wave. *Nature*, 368(6471): 527–529, 1994.
- [17] D. Strickland and G. Mourou. Compression of amplified chirped optical pulses. *Optics Communications*, 56(3):219–221, 1985.
- [18] H. Hamster, A. Sullivan, S. Gordon, W. White, and R. W. Falcone. Subpicosecond, electromagnetic pulses from intense laser-plasma interaction. *Phys. Rev. Lett.*, 71(17):2725–, 1993.
- [19] K. Nakajima, T. Kawakubo, H. Nakanishi, A. Ogata, Y. Kato, Y. Kitagawa, R. Kodama, K. Mima, H. Shiraga, K. Suzuki, T. Zhang, Y. Sakawa, T. Shoji, Y. Nishida, N. Yugami, M. Downer, D. Fisher, B. Newberger, and T. Tajima. A proof-of-principle experiment of laser wakefield acceleration. *Physica Scripta*, 1994(T52): 61, 1994.
- [20] A. Modena, Z. Najmudin, A. Dangor, C. Clayton, K. A. Marsh, C. Joshi, V. Malka, C. Darrow, C. Danson, D. Neely, and F. Walsh. Electron acceleration from the breaking of relativistic plasma waves. *Nature*, 377(6550):606–608, 1995.



- [21] A. Pukhov, Z.-M. Sheng, and J. Meyer-ter-Vehn. Particle acceleration in relativistic laser channels. *Phys. Plasmas*, 6(7):2847–2854, 1999.
- [22] C. Gahn, G. D. Tsakiris, A. Pukhov, J. Meyer-ter-Vehn, G. Pretzler, P. Thirolf, D. Habs, and K. J. Witte. Multi-MeV electron beam generation by direct laser acceleration in high-density plasma channels. *Phys. Rev. Lett.*, 83(23):4772–, 1999.
- [23] V. Malka, S. Fritzler, E. Lefebvre, M.-M. Aleonard, F. Burgy, J.-P. Chambaret, J.-F. Chemin, K. Krushelnick, G. Malka, S. P. D. Mangles, Z. Najmudin, M. Pittman, J.-P. Rousseau, J.-N. Scheurer, B. Walton, and A. E. Dangor. Electron acceleration by a wake field forced by an intense ultrashort laser pulse. *Science*, 298(5598):1596–1600, 2002.
- [24] A. Pukhov and J. Meyer-ter-Vehn. Laser wake field acceleration: the highly non-linear broken-wave regime. *Applied Physics B: Lasers and Optics*, 74(4):355–361, 2002.
- [25] S. P. D. Mangles, C. D. Murphy, Z. Najmudin, A. G. R. Thomas, J. L. Collier, A. E. Dangor, E. J. Divall, P. S. Foster, J. G. Gallacher, C. J. Hooker, D. A. Jaroszynski, A. J. Langley, W. B. Mori, P. A. Norreys, F. S. Tsung, R. Viskup, B. R. Walton, and K. Krushelnick. Monoenergetic beams of relativistic electrons from intense laser-plasma interactions. *Nature*, 431(7008):535–538, 2004.
- [26] C. G. R. Geddes, Cs. Toth, J. van Tilborg, E. Esarey, C. B. Schroeder, D. Bruhwiler, C. Nieter, J. Cary, and W. P. Leemans. High-quality electron beams from a laser wakefield accelerator using plasma-channel guiding. *Nature*, 431(7008):538–541, 2004.
- [27] J. Faure, Y. Glinec, A. Pukhov, S. Kiselev, S. Gordienko, E. Lefebvre, J.-P. Rousseau, F. Burgy, and V. Malka. A laser-plasma accelerator producing monoenergetic electron beams. *Nature*, 431(7008):541–544, 2004.
- [28] W. P. Leemans, B. Nagler, A. J. Gonsalves, Cs. Tóth, K. Nakamura, C. G. R. Geddes, E. Esarey, C. B. Schroeder, and S. M. Hooker. GeV electron beams from a centimetre-scale accelerator. *Nat Phys*, 2(10):696–699, 2006.
- [29] S. Karsch, J. Osterhoff, A. Popp, T. P. Rowlands-Rees, Zs. Major, M. Fuchs, M. Marx, R. Hörlein, K. Schmid, L. Veisz, S. Becker, U. Schramm, B. Hidding, G. Pretzler, D. Habs, F. Grüner, F. Krausz, and S. M. Hooker. GeV-scale electron acceleration in a gas-filled capillary discharge waveguide. *New Journal of Physics*, 9(11):415, 2007.

- [30] C. E. Clayton, J. E. Ralph, F. Albert, R. A. Fonseca, S. H. Glenzer, C. Joshi, W. Lu, K. A. Marsh, S. F. Martins, W. B. Mori, A. Pak, F. S. Tsung, B. B. Pollock, J. S. Ross, L. O. Silva, and D. H. Froula. Self-guided laser wakefield acceleration beyond 1 GeV using ionization-induced injection. *Phys. Rev. Lett.*, 105(10):105003–, 2010.
- [31] W. Leemans and E. Esarey. Laser-driven plasma-wave electron accelerators. *Physics Today*, 62:44–49, 2009.
- [32] M. Fuchs, R. Weingartner, A. Popp, Zs. Major, S. Becker, J. Osterhoff, I. Cortie, B. Zeitler, R. Hörlein, G. D. Tsakiris, U. Schramm, T. P. Rowlands-Rees, S. M. Hooker, D. Habs, F. Krausz, S. Karsch, and F. Grüner. Laser-driven soft-x-ray undulator source. *Nat Phys*, 5(11):826–829, 2009.
- [33] S. Bulanov, N. Naumova, F. Pegoraro, and J. Sakai. Particle injection into the wave acceleration phase due to nonlinear wake wave breaking. *Phys. Rev. E*, 58(5):R5257–, 1998.
- [34] C. G. R. Geddes, K. Nakamura, G. R. Plateau, Cs. Toth, E. Cormier-Michel, E. Esarey, C. B. Schroeder, J. R. Cary, and W. P. Leemans. Plasma-density-gradient injection of low absolute-momentum-spread electron bunches. *Phys. Rev. Lett.*, 100(21):215004–, 2008.
- [35] K. Schmid, A. Buck, C. M. S. Sears, J. M. Mikhailova, R. Tautz, D. Herrmann, M. Geissler, F. Krausz, and L. Veisz. Density-transition based electron injector for laser driven wakefield accelerators. *Phys. Rev. ST Accel. Beams*, 13(9):091301–, 2010.
- [36] J. Faure, C. Rechatin, O. Lundh, L. Ammoura, and V. Malka. Injection and acceleration of quasimonoenergetic relativistic electron beams using density gradients at the edges of a plasma channel. *Phys. Plasmas*, 17(8):083107–8, 2010.
- [37] D. Umstadter, J. K. Kim, and E. Dodd. Laser injection of ultrashort electron pulses into wakefield plasma waves. *Phys. Rev. Lett.*, 76(12):2073–, 1996.
- [38] E. Esarey, R. F. Hubbard, W. P. Leemans, A. Ting, and P. Sprangle. Electron injection into plasma wakefields by colliding laser pulses. *Phys. Rev. Lett.*, 79(14):2682–, 1997.
- [39] J. Faure, C. Rechatin, A. Norlin, A. Lifschitz, Y. Glinec, and V. Malka. Controlled injection and acceleration of electrons in plasma wakefields by colliding laser pulses. *Nature*, 444(7120):737–739, 2006.

- [40] H. Kotaki, I. Daito, M. Kando, Y. Hayashi, K. Kawase, T. Kameshima, Y. Fukuda, T. Homma, J. Ma, L.-M. Chen, T. Zh. Esirkepov, A. S. Pirozhkov, J. K. Koga, A. Faenov, T. Pikuz, H. Kiriya, H. Okada, T. Shimomura, Y. Nakai, M. Tanoue, H. Sasao, D. Wakai, H. Matsuura, S. Kondo, S. Kanazawa, A. Sugiyama, H. Daido, and S. V. Bulanov. Electron optical injection with head-on and countercrossing colliding laser pulses. *Phys. Rev. Lett.*, 103(19):194803–, 2009.
- [41] X. Davoine, E. Lefebvre, C. Rechatin, J. Faure, and V. Malka. Cold optical injection producing monoenergetic, multi-GeV electron bunches. *Phys. Rev. Lett.*, 102(6):065001–, 2009.
- [42] A. Pak, K. A. Marsh, S. F. Martins, W. Lu, W. B. Mori, and C. Joshi. Injection and trapping of tunnel-ionized electrons into laser-produced wakes. *Phys. Rev. Lett.*, 104(2):025003–, 2010.
- [43] C. McGuffey, A. G. R. Thomas, W. Schumaker, T. Matsuoka, V. Chvykov, F. J. Dollar, G. Kalintchenko, V. Yanovsky, A. Maksimchuk, K. Krushelnick, V. Yu. Bychenkov, I. V. Glazyrin, and A. V. Karpeev. Ionization induced trapping in a laser wakefield accelerator. *Phys. Rev. Lett.*, 104(2):025004–, 2010.
- [44] C. M. S. Sears, S. Benavides Cuevas, U. Schramm, K. Schmid, A. Buck, D. Habs, F. Krausz, and L. Veisz. A high resolution, broad energy acceptance spectrometer for laser wakefield acceleration experiments. *Rev. Sci. Instrum.*, 81(7):073304–7, 2010.
- [45] E. Brunetti, R. P. Shanks, G. G. Manahan, M. R. Islam, B. Ersfeld, M. P. Anania, S. Cipiccia, R. C. Issac, G. Raj, G. Vieux, G. H. Welsh, S. M. Wiggins, and D. A. Jaroszynski. Low emittance, high brilliance relativistic electron beams from a laser-plasma accelerator. *Phys. Rev. Lett.*, 105(21):215007–, 2010.
- [46] J. van Tilborg, C. B. Schroeder, C. V. Filip, Cs. Tóth, C. G. R. Geddes, G. Fubiani, R. Huber, R. A. Kaindl, E. Esarey, and W. P. Leemans. Temporal characterization of femtosecond laser-plasma-accelerated electron bunches using terahertz radiation. *Phys. Rev. Lett.*, 96(1):014801–, 2006.
- [47] T. Ohkubo, A. Maekawa, R. Tsujii, T. Hosokai, K. Kinoshita, K. Kobayashi, M. Uesaka, A. Zhidkov, K. Nemoto, Y. Kondo, and Y. Shibata. Temporal characteristics of monoenergetic electron beams generated by the laser wakefield acceleration. *Phys. Rev. ST Accel. Beams*, 10(3):031301–, 2007.

- [48] J. van Tilborg, Cs. Tóth, N. H. Matlis, G. R. Plateau, and W. P. Leemans. Single-shot measurement of the spectral envelope of broad-bandwidth terahertz pulses from femtosecond electron bunches. *Opt. Lett.*, 33(11):1186–1188, 2008.
- [49] A. D. Debus, M. Bussmann, U. Schramm, R. Sauerbrey, C. D. Murphy, Zs. Major, R. Hörlein, L. Veisz, K. Schmid, J. Schreiber, K. Witte, S. P. Jamison, J. G. Gallacher, D. A. Jaroszynski, M. C. Kaluza, B. Hidding, S. Kiselev, R. Heathcote, P. S. Foster, D. Neely, E. J. Divall, C. J. Hooker, J. M. Smith, K. Ertel, A. J. Langley, P. Norreys, and J. L. Collier. Electron bunch length measurements from laser-accelerated electrons using single-shot thz time-domain interferometry. *Phys. Rev. Lett.*, 104(8):084802–, 2010.
- [50] O. Lundh, J. Lim, C. Rechatin, L. Ammoura, A. Ben-Ismaïl, X. Davoine, G. Gallot, J-P. Goddet, E. Lefebvre, V. Malka, and J. Faure. Few femtosecond, few kiloampere electron bunch produced by a laser-plasma accelerator. *Nat Phys*, 7:219–222, 2011.
- [51] N. H. Matlis, S. Reed, S. S. Bulanov, V. Chvykov, G. Kalintchenko, T. Matsuoka, P. Rousseau, V. Yanovsky, A. Maksimchuk, S. Kalmykov, G. Shvets, and M. C. Downer. Snapshots of laser wakefields. *Nat Phys*, 2(11):749–753, 2006.
- [52] P. Dong, S. A. Reed, S. A. Yi, S. Kalmykov, G. Shvets, M. C. Downer, N. H. Matlis, W. P. Leemans, C. McGuffey, S. S. Bulanov, V. Chvykov, G. Kalintchenko, K. Krushelnick, A. Maksimchuk, T. Matsuoka, A. G. R. Thomas, and V. Yanovsky. Formation of optical bullets in laser-driven plasma bubble accelerators. *Phys. Rev. Lett.*, 104(13):134801–, 2010.
- [53] P. Dong, S. A. Reed, S. A. Yi, S. Kalmykov, Z. Y. Li, G. Shvets, N. H. Matlis, C. McGuffey, S. S. Bulanov, V. Chvykov, G. Kalintchenko, K. Krushelnick, A. Maksimchuk, T. Matsuoka, A. G. R. Thomas, V. Yanovsky, and M. C. Downer. Holographic visualization of laser wakefields. *New Journal of Physics*, 12(4):045016, 2010.
- [54] M. C. Kaluza, H.-P. Schlenvoigt, S. P. D. Mangles, A. G. R. Thomas, A. E. Dangor, H. Schworer, W. B. Mori, Z. Najmudin, and K. M. Krushelnick. Measurement of magnetic-field structures in a laser-wakefield accelerator. *Phys. Rev. Lett.*, 105(11):115002–, 2010.
- [55] A. Buck, M. Nicolai, K. Schmid, C. M. S. Sears, A. Sävert, J. M. Mikhailova, F. Krausz, M. C. Kaluza, and L. Veisz. Real-time observation of laser-driven electron acceleration. *Nat Phys*, 7(7):543–548, 2011.

- [56] A. Buck, K. Zeil, A. Popp, K. Schmid, A. Jochmann, S. D. Kraft, B. Hidding, T. Kudyakov, C. M. S. Sears, L. Veisz, S. Karsch, J. Pawelke, R. Sauerbrey, T. Cowan, F. Krausz, and U. Schramm. Absolute charge calibration of scintillating screens for relativistic electron detection. *Rev. Sci. Instrum.*, 81(3):033301–6, 2010.
- [57] K. Schmid, L. Veisz, F. Tavella, S. Benavides, R. Tautz, D. Herrmann, A. Buck, B. Hidding, A. Marcinkevicius, U. Schramm, M. Geissler, J. Meyer-ter Vehn, D. Habs, and F. Krausz. Few-cycle laser-driven electron acceleration. *Phys. Rev. Lett.*, 102(12):124801–4, 2009.
- [58] L. Veisz, K. Schmid, F. Tavella, S. Benavides, R. Tautz, D. Herrmann, A. Buck, B. Hidding, A. Marcinkevicius, U. Schramm, M. Geissler, J. Meyer-ter Vehn, D. Habs, and F. Krausz. Laser-driven electron acceleration in plasmas with few-cycle pulses. *Comptes Rendus Physique*, 10(2-3):140–147, 2009.
- [59] J. M. Mikhailova, A. Buck, A. Borot, K. Schmid, C. M. S. Sears, G. D. Tsakiris, F. Krausz, and L. Veisz. Ultra-high-contrast few-cycle pulses for multipetawatt-class laser technology. *Opt. Lett.*, 36(16):3145–3147, August 2011.
- [60] J. D. Jackson. *Classical Electrodynamics*. Wiley, 3rd edition, 1998.
- [61] V. Yanovsky, V. Chvykov, G. Kalinchenko, P. Rousseau, T. Planchon, T. Matsuoka, A. Maksimchuk, J. Nees, G. Cheriaux, G. Mourou, and K. Krushelnick. Ultra-high intensity-300-TW laser at 0.1 Hz repetition rate. *Opt. Express*, 16(3):2109–2114, 2008.
- [62] C. I. Moore, J. P. Knauer, and D. D. Meyerhofer. Observation of the transition from thomson to compton scattering in multiphoton interactions with low-energy electrons. *Phys. Rev. Lett.*, 74(13):2439–, 1995.
- [63] D. D. Meyerhofer. High-intensity-laser-electron scattering. *IEEE Journal of Quantum Electronics*, 33(11):1935–1941, 1997.
- [64] P. M. Woodward. A method of calculating the field over a plane. *Journal of the Institution of Electrical Engineers*, 93:1554–1558, 1947.
- [65] J. D. Lawson. Lasers and accelerators. *IEEE Transactions on Nuclear Science*, 26(9):4217–4219, 1979.
- [66] T. Plettner, R. L. Byer, E. Colby, B. Cowan, C. M. S. Sears, J. E. Spencer, and R. H. Siemann. Visible-laser acceleration of relativistic electrons in a semi-infinite vacuum. *Phys. Rev. Lett.*, 95(13):134801, 2005.

- [67] L. V. Keldysh. Ionization in the field of a strong electromagnetic wave. *Sov. Phys.-JETP*, 20:1037, 1965.
- [68] P. Gibbon. *Short Pulse Laser Interactions with Matter: An Introduction*. Imperial College Press, 2005.
- [69] M. V. Ammosov, N. B. Delone, and V. P. Krainov. Tunnel ionization of complex atoms and of atomic ions in an alternating electromagnetic field. *Soviet Physics, Journal of Experimental and Theoretical Physics*, 64 (6):1191–1194, 1986.
- [70] R. J. Goldston and P. H. Rutherford. *Introduction to Plasma Physics*. Taylor & Francis, 1995.
- [71] W. L. Kruer. *The Physics of Laser Plasma Interactions*. Westview Press, 2003.
- [72] D. von der Linde, T. Engers, G. Jenke, P. Agostini, G. Grillon, E. Nibbering, A. Mysyrowicz, and A. Antonetti. Generation of high-order harmonics from solid surfaces by intense femtosecond laser pulses. *Phys. Rev. A*, 52(1):R25–, 1995.
- [73] P. Gibbon. Harmonic generation by femtosecond laser-solid interaction: A coherent "water-window" light source? *Phys. Rev. Lett.*, 76(1):50–, 1996.
- [74] R. Lichters, J. Meyer-ter-Vehn, and A. Pukhov. Short-pulse laser harmonics from oscillating plasma surfaces driven at relativistic intensity. *Phys. Plasmas*, 3(9):3425–3437, 1996.
- [75] C. Gerthsen. *Physik*, volume 22. Springer-Verlag, 2002.
- [76] G. S. Settles. *Schlieren and Shadowgraph Techniques*. Springer-Verlag, 2001.
- [77] P. Sprangle, E. Esarey, and A. Ting. Nonlinear theory of intense laser-plasma interactions. *Phys. Rev. Lett.*, 64(17):2011–, 1990.
- [78] P. Sprangle, E. Esarey, J. Krall, and G. Joyce. Propagation and guiding of intense laser pulses in plasmas. *Phys. Rev. Lett.*, 69(15):2200–, 1992.
- [79] E. Esarey, C. B. Schroeder, and W. P. Leemans. Physics of laser-driven plasma-based electron accelerators. *Rev. Mod. Phys.*, 81(3):1229–, 2009.
- [80] R. J. Noble. Plasma-wave generation in the beat-wave accelerator. *Phys. Rev. A*, 32 (1):460–, 1985.

- [81] P. Sprangle, E. Esarey, A. Ting, and G. Joyce. Laser wakefield acceleration and relativistic optical guiding. *Appl. Phys. Lett.*, 53(22):2146–2148, 1988.
- [82] S. V. Bulanov, V. I. Kirsanov, and A. S. Sakharov. Excitation of ultra-relativistic langmuir waves by electromagnetic pulses. *Physica Scripta*, T30:208–209, 1990.
- [83] V. I. Berezhiani and I. G. Murusidze. Relativistic wake-field generation by an intense laser pulse in a plasma. *Physics Letters A*, 148(6-7):338–340, 1990.
- [84] Z. M. Sheng and J. Meyer-ter-Vehn. Relativistic wave breaking in warm plasmas. *Physics of Plasmas*, 4:493, 1996.
- [85] J. Meyer-ter-Vehn and A. Pukhov. Lecture on relativistic laser plasma interaction: I. Analytical tools.
- [86] T. Esirkepov, S. V. Bulanov, M. Yamagiwa, and T. Tajima. Electron, positron, and photon wakefield acceleration: Trapping, wake overtaking, and ponderomotive acceleration. *Phys. Rev. Lett.*, 96(1):014803–, 2006.
- [87] E. Esarey and M. Pilloff. Trapping and acceleration in nonlinear plasma waves. *Phys. Plasmas*, 2(5):1432–1436, 1995.
- [88] T. Katsouleas. Beam loading in plasma accelerators. *Particle Accelerators*, 22: 81–99, 1987.
- [89] M. Tzoufras, W. Lu, F. S. Tsung, C. Huang, W. B. Mori, T. Katsouleas, J. Vieira, R. A. Fonseca, and L. O. Silva. Beam loading in the nonlinear regime of plasma-based acceleration. *Phys. Rev. Lett.*, 101(14):145002–, 2008.
- [90] C. Rechatin, X. Davoine, A. Lifschitz, A. Ben Ismail, J. Lim, E. Lefebvre, J. Faure, and V. Malka. Observation of beam loading in a laser-plasma accelerator. *Phys. Rev. Lett.*, 103(19):194804–, 2009.
- [91] M. Tzoufras, W. Lu, F. S. Tsung, C. Huang, W. B. Mori, T. Katsouleas, J. Vieira, R. A. Fonseca, and L. O. Silva. Beam loading by electrons in nonlinear plasma wakes. *Phys. Plasmas*, 16(5):056705–12, 2009.
- [92] A. Pukhov and S. Gordienko. Bubble regime of wake field acceleration: similarity theory and optimal scalings. *Philosophical Transactions of the Royal Society A: Mathematical, Physical and Engineering Sciences*, 364(1840):623–633, 2006.
- [93] S. Gordienko and A. Pukhov. Scalings for ultrarelativistic laser plasmas and quasi-monoenergetic electrons. *Phys. Plasmas*, 12(4):043109–11, 2005.

- [94] W. Lu, M. Tzoufras, C. Joshi, F. S. Tsung, W. B. Mori, J. Vieira, R. A. Fonseca, and L. O. Silva. Generating multi-GeV electron bunches using single stage laser wakefield acceleration in a 3D nonlinear regime. *Phys. Rev. ST Accel. Beams*, 10(6):061301–, 2007.
- [95] T. Katsouleas. Accelerator physics: Electrons hang ten on laser wake. *Nature*, 431(7008):515–516, 2004.
- [96] S. V. Bulanov, F. Pegoraro, A. M. Pukhov, and A. S. Sakharov. Transverse-wake wave breaking. *Phys. Rev. Lett.*, 78(22):4205–, 1997.
- [97] P. Mora and T. M. Antonsen. Electron cavitation and acceleration in the wake of an ultraintense, self-focused laser pulse. *Phys. Rev. E*, 53(3):R2068–, 1996.
- [98] I. Kostyukov, A. Pukhov, and S. Kiselev. Phenomenological theory of laser-plasma interaction in “bubble” regime. *Phys. Plasmas*, 11(11):5256–5264, 2004.
- [99] I. Kostyukov, E. Nerush, A. Pukhov, and V. Seredov. Electron self-injection in multidimensional relativistic-plasma wake fields. *Phys. Rev. Lett.*, 103(17):175003, 2009.
- [100] S. Kalmykov, S. A. Yi, V. Khudik, and G. Shvets. Electron self-injection and trapping into an evolving plasma bubble. *Phys. Rev. Lett.*, 103(13):135004–, 2009.
- [101] S. Y. Kalmykov, A. Beck, S. A. Yi, V. Khudik, B. A. Shadwick, E. Lefebvre, and M. C. Downer. Electron self-injection into an evolving plasma bubble: The way to a dark current free GeV-scale laser accelerator. In *Proceedings of the 2010 Advanced Accelerator Workshop*, 2010.
- [102] H. Suk, N. Barov, J. B. Rosenzweig, and E. Esarey. Plasma electron trapping and acceleration in a plasma wake field using a density transition. *Phys. Rev. Lett.*, 86(6):1011–, 2001.
- [103] P. Tomassini, M. Galimberti, A. Giulietti, D. Giulietti, L. A. Gizzi, L. Labate, and F. Pegoraro. Production of high-quality electron beams in numerical experiments of laser wakefield acceleration with longitudinal wave breaking. *Phys. Rev. ST Accel. Beams*, 6(12):121301–, 2003.
- [104] H. Suk, H. J. Lee, and I. S. Ko. Generation of high-energy electrons by a femtosecond terawatt laser propagating through a sharp downward density transition. *J. Opt. Soc. Am. B*, 21(7):1391–1396, 2004.



- [105] A. V. Brantov, T. Zh. Esirkepov, M. Kando, H. Kotaki, V. Yu. Bychenkov, and S. V. Bulanov. Controlled electron injection into the wake wave using plasma density inhomogeneity. *Phys. Plasmas*, 15(7):073111–10, 2008.
- [106] J. U. Kim, N. Hafz, and H. Suk. Electron trapping and acceleration across a parabolic plasma density profile. *Phys. Rev. E*, 69(2):026409–, 2004.
- [107] T.-Y. Chien, C.-L. Chang, C.-H. Lee, J.-Y. Lin, J. Wang, and S.-Y. Chen. Spatially localized self-injection of electrons in a self-modulated laser-wakefield accelerator by using a laser-induced transient density ramp. *Phys. Rev. Lett.*, 94(11):115003–, 2005.
- [108] J. Kim, H. Jang, S. Yoo, M. Hur, I. Hwang, J. Lim, V. Kulagin, H. Suk, I. W. Choi, N. Hafz, H. T. Kim, K.-H. Hong, T. J. Yu, J. H. Sung, T. M. Jeong, Y.-C. Noh, D.-K. Ko, and J. Lee. Quasi-monoenergetic electron-beam generation using a laser accelerator for ultra-short x-ray sources. *J. Korean Phys. Soc.*, 51:397, 2007.
- [109] P. Zhang, N. Saleh, S. Chen, Z. M. Sheng, and D. Umstadter. Laser-energy transfer and enhancement of plasma waves and electron beams by interfering high-intensity laser pulses. *Phys. Rev. Lett.*, 91(22):225001–, 2003.
- [110] E. S. Dodd, J. K. Kim, and D. Umstadter. Simulation of ultrashort electron pulse generation from optical injection into wake-field plasma waves. *Phys. Rev. E*, 70(5):056410–, 2004.
- [111] C. Rechatin, J. Faure, A. Ben-Ismaïl, J. Lim, R. Fitour, A. Specka, H. Videau, A. Tafzi, F. Burgy, and V. Malka. Controlling the phase-space volume of injected electrons in a laser-plasma accelerator. *Phys. Rev. Lett.*, 102(16):164801, 2009.
- [112] K. P. Singh and V. Sajal. Quasimonoenergetic collimated electrons from the ionization of nitrogen by a chirped intense laser pulse. *Phys. Plasmas*, 16(4):043113–8, 2009.
- [113] A. Pukhov and J. Meyer-ter Vehn. Relativistic magnetic self-channeling of light in near-critical plasma: Three-dimensional particle-in-cell simulation. *Phys. Rev. Lett.*, 76(21):3975–, 1996.
- [114] C. Nieter and J. R. Cary. VORPAL: a versatile plasma simulation code. *Journal of Computational Physics*, 196(2):448–473, 2004.

- [115] R. Fonseca, L. Silva, F. Tsung, V. Decyk, W. Lu, C. Ren, W. Mori, S. Deng, S. Lee, T. Katsouleas, and J. Adam. OSIRIS: A three-dimensional, fully relativistic particle in cell code for modeling plasma based accelerators. *Lecture Notes in Computer Science*, 2331:342–351, 2002.
- [116] M. Geissler, J. Schreiber, and J. Meyer-ter Vehn. Bubble acceleration of electrons with few-cycle laser pulses. *New Journal of Physics*, 8(9):186, 2006.
- [117] A. Dubietis, G. Jonusauskas, and A. Piskarskas. Powerful femtosecond pulse generation by chirped and stretched pulse parametric amplification in BBO crystal. *Optics Communications*, 88(4-6):437–440, 1992.
- [118] F. Tavella, Y. Nomura, L. Veisz, V. Pervak, A. Marcinkevicius, and F. Krausz. Dispersion management for a sub-10-fs, 10 TW optical parametric chirped-pulse amplifier. *Opt. Lett.*, 32(15):2227–2229, 2007.
- [119] D. Herrmann, L. Veisz, R. Tautz, F. Tavella, K. Schmid, V. Pervak, and F. Krausz. Generation of sub-three-cycle, 16 TW light pulses by using noncollinear optical parametric chirped-pulse amplification. *Opt. Lett.*, 34(16):2459–2461, 2009.
- [120] A. L. Cavalieri, E. Goulielmakis, B. Horvath, W. Helml, M. Schultze, M. Fieß, V. Pervak, L. Veisz, V. S. Yakovlev, M. Uiberacker, A. Apolonski, F. Krausz, and R. Kienberger. Intense 1.5-cycle near infrared laser waveforms and their use for the generation of ultra-broadband soft-x-ray harmonic continua. *New Journal of Physics*, 9(7):242, 2007.
- [121] C. Thaury, F. Quere, J.-P. Geindre, A. Levy, T. Ceccotti, P. Monot, M. Bougeard, F. Reau, P. D’Oliveira, P. Audebert, R. Marjoribanks, and Ph. Martin. Plasma mirrors for ultrahigh-intensity optics. *Nat Phys*, 3(6):424–429, 2007.
- [122] K. Schmid. *Supersonic Micro-Jets And Their Application to Few-Cycle Laser-Driven Electron Acceleration*. PhD thesis, Ludwigs-Maximilians-Universität München, 2009.
- [123] IDEA – Interferometric Data Evaluation Algorithms. URL <http://www.optics.tugraz.at/idea/idea.html>. Downloaded 20 July 2011.
- [124] H. M. Mott-Smith. The solution of the boltzmann equation for a shock wave. *Phys. Rev.*, 82(6):885–, 1951.
- [125] D. Haenel. *Molekulare Gasdynamik*. Springer-Verlag, 2004.

- [126] R. D. Zucker and O. Biblarz. *Fundamentals of Gas Dynamics*. Wiley, New York, 2002.
- [127] K. L. Brown and G. W. Tautfest. Faraday-cup monitors for high-energy electron beams. *Rev. Sci. Instrum.*, 27(9):696–702, 1956.
- [128] C. Gahn, G. D. Tsakiris, K. J. Witte, P. Thirolf, and D. Habs. A novel 45-channel electron spectrometer for high intensity laser-plasma interaction studies. *Rev. Sci. Instrum.*, 71(4):1642–1645, 2000.
- [129] K. A. Tanaka, T. Yabuuchi, T. Sato, R. Kodama, Y. Kitagawa, T. Takahashi, T. Ikeda, Y. Honda, and S. Okuda. Calibration of imaging plate for high energy electron spectrometer. *Rev. Sci. Instrum.*, 76(1):013507–5, 2005.
- [130] Y. Glinec, J. Faure, A. Guemnie-Tafo, V. Malka, H. Monard, J. P. Larbre, V. De Waele, J. L. Marignier, and M. Mostafavi. Absolute calibration for a broad range single shot electron spectrometer. *Rev. Sci. Instrum.*, 77(10):103301–6, 2006.
- [131] B. Hidding, G. Pretzler, M. Clever, F. Brandl, F. Zamponi, A. Lübcke, T. Kämpfer, I. Uschmann, E. Förster, U. Schramm, R. Sauerbrey, E. Kroupp, L. Veisz, K. Schmid, S. Benavides, and S. Karsch. Novel method for characterizing relativistic electron beams in a harsh laser-plasma environment. *Rev. Sci. Instrum.*, 78(8):083301–8, 2007.
- [132] S. Masuda, E. Miura, K. Koyama, and S. Kato. Absolute calibration of an electron spectrometer using high energy electrons produced by the laser-plasma interaction. *Rev. Sci. Instrum.*, 79(8):083301–4, 2008.
- [133] K. Nakamura, W. Wan, N. Ybarrolaza, D. Syversrud, J. Wallig, and W. P. Leemans. Broadband single-shot electron spectrometer for GeV-class laser-plasma-based accelerators. *Rev. Sci. Instrum.*, 79(5):053301–5, 2008.
- [134] K. Zeil, S. D. Kraft, A. Jochmann, F. Kroll, W. Jahr, U. Schramm, L. Karsch, J. Pawelke, B. Hidding, and G. Pretzler. Absolute response of Fuji imaging plate detectors to picosecond-electron bunches. *Rev. Sci. Instrum.*, 81(1):013307–6, 2010.
- [135] J. B. Birks. *The Theory and Practice of Scintillation Counting*. Pergamon Press, Oxford, 1964.
- [136] T. Eichner, F. Grüner, S. Becker, M. Fuchs, D. Habs, R. Weingartner, U. Schramm, H. Backe, P. Kunz, and W. Lauth. Miniature magnetic devices for laser-based, table-top free-electron lasers. *Phys. Rev. ST Accel. Beams*, 10(8):082401–, 2007.

- [137] H. Schwoerer, B. Liesfeld, H.-P. Schlenvoigt, K.-U. Amthor, and R. Sauerbrey. Thomson-backscattered X Rays from laser-accelerated electrons. *Phys. Rev. Lett.*, 96(1):014802–, 2006.
- [138] J. B. Hastings, F. M. Rudakov, D. H. Dowell, J. F. Schmerge, J. D. Cardoza, J. M. Castro, S. M. Gierman, H. Loos, and P. M. Weber. Ultrafast time-resolved electron diffraction with megavolt electron beams. *Appl. Phys. Lett.*, 89(18):184109–3, 2006.
- [139] A. G. R. Thomas, S. P. D. Mangles, Z. Najmudin, M. C. Kaluza, C. D. Murphy, and K. Krushelnick. Measurements of wave-breaking radiation from a laser-wakefield accelerator. *Phys. Rev. Lett.*, 98(5):054802–, 2007.
- [140] J. Osterhoff, A. Popp, Zs. Major, B. Marx, T. P. Rowlands-Rees, M. Fuchs, M. Geissler, R. Hörlein, B. Hidding, S. Becker, E. A. Peralta, U. Schramm, F. Grüner, D. Habs, F. Krausz, S. M. Hooker, and S. Karsch. Generation of stable, low-divergence electron beams by laser-wakefield acceleration in a steady-state-flow gas cell. *Phys. Rev. Lett.*, 101(8):085002–, 2008.
- [141] C. M. S. Sears, A. Buck, K. Schmid, J. Mikhailova, F. Krausz, and L. Veisz. Emitance and divergence of laser wakefield accelerated electrons. *Phys. Rev. ST Accel. Beams*, 13(9):092803–, 2010.
- [142] J. A. Stamper and B. H. Ripin. Faraday-rotation measurements of megagauss magnetic fields in laser-produced plasmas. *Phys. Rev. Lett.*, 34(3):138–, 1975.
- [143] T. Matsuoka, C. McGuffey, P. G. Cummings, Y. Horovitz, F. Dollar, V. Chvykov, G. Kalintchenko, P. Rousseau, V. Yanovsky, S. S. Bulanov, A. G. R. Thomas, A. Maksimchuk, and K. Krushelnick. Stimulated Raman side scattering in laser wakefield acceleration. *Phys. Rev. Lett.*, 105(3):034801–, 2010.
- [144] S. P. D. Mangles, A. G. R. Thomas, M. C. Kaluza, O. Lundh, F. Lindau, A. Persson, F. S. Tsung, Z. Najmudin, W. B. Mori, C.-G. Wahlström, and K. Krushelnick. Laser-wakefield acceleration of monoenergetic electron beams in the first plasma-wave period. *Phys. Rev. Lett.*, 96(21):215001–, 2006.
- [145] A. Lévy, T. Ceccotti, P. D’Oliveira, F. Réau, M. Perdrix, F. Quéré, P. Monot, M. Bougeard, H. Lagadec, P. Martin, J.-P. Geindre, and P. Audebert. Double plasma mirror for ultrahigh temporal contrast ultraintense laser pulses. *Opt. Lett.*, 32(3): 310–312, 2007.

- [146] A. Jullien, O. Albert, F. Burgy, G. Hamoniaux, J.-P. Rousseau, J.-P. Chambaret, F. Augé-Rochereau, G. Chériaux, J. Etchepare, N. Minkovski, and S. M. Saltiel.  $10^{-10}$  temporal contrast for femtosecond ultraintense lasers by cross-polarized wave generation. *Opt. Lett.*, 30(8):920–922, 2005.
- [147] V. Chvykov, P. Rousseau, S. Reed, G. Kalinchenko, and V. Yanovsky. Generation of  $10^{11}$  contrast 50 TW laser pulses. *Opt. Lett.*, 31(10):1456–1458, 2006.
- [148] V. Pervak, I. Ahmad, M. K. Trubetskov, A. V. Tikhonravov, and F. Krausz. Double-angle multilayer mirrors with smooth dispersion characteristics. *Opt. Express*, 17(10):7943–7951, 2009.
- [149] L. Canova, S. Kourtev, N. Minkovski, A. Jullien, R. Lopez-Martens, O. Albert, and S. M. Saltiel. Efficient generation of cross-polarized femtosecond pulses in cubic crystals with holographic cut orientation. *Appl. Phys. Lett.*, 92(23):231102–3, 2008.
- [150] A. Jullien, C. Durfee, A. Trisorio, L. Canova, J.-P. Rousseau, B. Mercier, L. Antonucci, G. Chériaux, O. Albert, and R. Lopez-Martens. Nonlinear spectral cleaning of few-cycle pulses via cross-polarized wave (XPW) generation. *Applied Physics B: Lasers and Optics*, 96(2):293–299, 2009.
- [151] F. Tavella, K. Schmid, N. Ishii, A. Marcinkevicius, L. Veisz, and F. Krausz. High-dynamic range pulse-contrast measurements of a broadband optical parametric chirped-pulse amplifier. *Applied Physics B: Lasers and Optics*, 81(6):753–756, 2005.



# Publications by the Author

## Journal articles

(Articles are listed in reverse order of appearance.)

J. M. Mikhailova, [A. Buck](#), A. Borot, K. Schmid, C. M. S. Sears, G. D. Tsakiris, F. Krausz, and L. Veisz. Ultrahigh-contrast few-cycle pulses for petawatt-class laser technology. *Opt. Lett.*, 36:3145, 2011.

[A. Buck](#), M. Nicolai, K. Schmid, C. M. S. Sears, A. Sävert, J. M. Mikhailova, F. Krausz, M. C. Kaluza, and L. Veisz. Real-time observation of laser-driven electron acceleration. *Nat Phys.* 7:543, 2011.

C. M. S. Sears, [A. Buck](#), K. Schmid, J. M. Mikhailova, F. Krausz, and L. Veisz. Emittance and divergence of laser wakefield accelerated electrons. *Phys. Rev. ST Accel. Beams* 13:092803, 2010.

K. Schmid, [A. Buck](#), C. M. S. Sears, J. M. Mikhailova, R. Tautz, D. Herrmann, M. Geissler, F. Krausz, and L. Veisz. Density-transition based electron injector for laser driven wakefield accelerators. *Phys. Rev. ST Accel. Beams* 13:091301, 2010.

C. M. S. Sears, S. Benavides Cuevas, U. Schramm, K. Schmid, [A. Buck](#), D. Habs, F. Krausz, and L. Veisz. A high resolution, broad energy acceptance spectrometer for laser wakefield acceleration experiments. *Rev. Sci. Instrum.* 81:073304, 2010.

A. Buck, K. Zeil, A. Popp, K. Schmid, A. Jochmann, S. D. Kraft, B. Hidding, T. Kudyakov, C. M. S. Sears, L. Veisz, S. Karsch, J. Pawelke, R. Sauerbrey, T. Cowan, F. Krausz, and U. Schramm. Absolute charge calibration of scintillating screens for relativistic electron detection. *Rev. Sci. Instrum.* 81:033301, 2010.

C. M. S. Sears, A. Buck, K. Schmid, L. Veisz, D. Herrmann, J. M. Mikhailova, R. Tautz, and F. Krausz. Attosecond slicing of an LWFA produced electron beam. *Proc. SPIE* 7359:735904, 2009.

L. Veisz, K. Schmid, F. Tavella, S. Benavides, R. Tautz, D. Herrmann, A. Buck, B. Hidding, A. Marcinkevicius, U. Schramm, M. Geissler, J. Meyer-ter-Vehn, D. Habs, and F. Krausz. Laser-driven electron acceleration in plasmas with few-cycle pulses. *Compt. Rend. Phys.*, 10(2-3):140–147, 2009.

K. Schmid, L. Veisz, F. Tavella, S. Benavides, R. Tautz, D. Herrmann, A. Buck, B. Hidding, A. Marcinkevicius, U. Schramm, M. Geissler, J. Meyer-ter-Vehn, D. Habs, and F. Krausz. Few-cycle laser-driven electron acceleration. *Phys. Rev. Lett.*, 102(12):124801, 2009.

## Popular science articles

A. Buck, L. Veisz, and M. C. Kaluza. Wie ein Laser Elektronen beschleunigt. *Physik in unserer Zeit*, 42:165-166, 2011.

## Manuscripts in preparation

A. Buck, J. Wenz, J. Xu, J. M. Mikhailova, F. Krausz, S. Karsch, and L. Veisz. Stabilization and control of laser-driven electron acceleration via a sharp density transition. In preparation.



# Data archiving

The experimental raw data, the evaluation files, and the figures can be found on the Data Archive Server of the Laboratory for Attosecond Physics at the Max Planck Institute of Quantum Optics. The directories and filenames of all used files are given for each figure on the next pages. Typically, these directories contain Matlab files to evaluate the raw data, plot files created with OriginPro 8.1, and the final .eps files used in the thesis. The raw data is placed in a separate folder together with an explanatory text document stating the day the data was acquired.

## Figure 1.1

Comparison of different ionization mechanisms.

► figure file `chapter1\Fig1-1_Ionization3.eps`

## Figure 1.2

Refraction of a probe beam at the plasma.

► figure file `chapter1\Fig1-2_Plasmalens2.eps`

## Figure 1.3

Snell's law.

► figure file `chapter1\Fig1-3_Snell1.eps`

## Figure 1.4

Nonlinear, one-dimensional wakefield in the quasi-static-amplitude approximation.

► simulation file `chapter1\eval\solution2_1D_wakefield_phase_space.m`

► plot file `chapter1\Fig1-4_Preparation_wakefield.opj`

► figure file `chapter1\Fig1-4_1D_wakefield2.eps`

## Figure 1.5

Optimum wakefield driving conditions.

► simulation file `chapter1\eval\optimum_driving_conditions.m`

▶ figure file      `chapter1\Fig1-5_1D_maximumfield2.eps`

### Figure 1.6

Longitudinal phase-space in the one-dimensional model.

▶ simulation file `chapter1\eval\solution2_1D_wakefield_phase_space.m`

▶ figure file      `chapter1\Fig1-6_Phasespace6.eps`

### Figure 1.7

Comparison of dephasing and depletion length.

▶ plot file        `chapter1\Fig1-7_Preparation_Depletion_Dephasing.opj`

▶ figure file      `chapter1\Fig1-7_Depletion_Dephasing3.eps`

### Figure 1.8

Illustration of the beamloading effect.

▶ figure file      `chapter1\Fig1-8_Beamloading5.eps`

### Figure 1.9

Transverse wave breaking in the "bubble" regime.

▶ figure file      `chapter1\Fig1-9_Bubble.eps`

### Figure 1.10

Injection of electrons at a sharp density transition.

▶ figure file      `chapter1\Fig1-10_Injection_at_sharp_transition.eps`

### Figure 1.11

Particle-in-cell simulation at one frame during the interaction.

▶ raw data folder `chapter1\raw_data_1-11_PIC\`

▶ simulation file `chapter1\raw_data_1-11_PIC\input.txt`

▶ evaluation file `chapter1\Fig1-11_Diss_plot_PIC.m`

▶ figure file      `chapter1\Fig1-11_PIC4.eps`

### Figure 2.1

Basic experimental setup for LWFA experiments.

▶ figure file      `chapter2\Fig2-1_Electron_Acceleration_Setup.eps`

### Figure 2.2

Layout of Light Wave Synthesizer 20.

▶ figure file      `chapter2\Fig2-2_LWS20_layout3.eps`

**Figure 2.3**

Output parameters of LWS-20.

- ▶ raw data folder `chapter2\raw_data_2-3_LWS20\`
- ▶ plot file `chapter2\Fig2-3_LWS20_Parameters.opj`
- ▶ figure file `chapter2\Fig2-3_LWS20_Parameters2.eps`

**Figure 2.4**

Layout of the ATLAS laser system.

- ▶ figure file `chapter2\Fig2-4_ATLAS_layout2.eps`

**Figure 2.5**

Gas jet interferometry.

- ▶ raw data folder `chapter2\raw_data_2-5_Interferometry\`
- ▶ evaluation file `chapter2\eval\Interferometry_Filter_and_Unwrap_9_phase_for_diss.m`
- ▶ figure file `chapter2\Fig2-5_Interferometer_phase.eps`

**Figure 2.6**

Gaussian and trapezoidal fit functions.

- ▶ figure file `chapter2\Fig2-6_Fit_Functions.eps`

**Figure 2.7**

Comparison of fitting routine and Abel inversion.

- ▶ raw data folder `chapter2\raw_data_2-7_Density_comparison\`
- ▶ evaluation file `chapter2\eval\Interferometry_Filter_and_Unwrap_8.m`
- ▶ evaluation file `chapter2\eval\Interferometry_Fit_Combined_9.m`
- ▶ evaluation file `chapter2\eval\Interferometry_Plot_And_Eval_10_dissertation.m`
- ▶ figure file `chapter2\Fig2-7_Four_profiles_with_fit.eps`

**Figure 2.8**

Generation of a shockfront in a supersonic flow.

- ▶ evaluation file See archived data for Schmid et al. [35].
- ▶ figure file `chapter2\Fig2-8_Shockfront.eps`

**Figure 2.9**

Electron energy spectrometer.

- ▶ evaluation file See archived data for Sears et al. [44].
- ▶ figure file chapter2\Fig2-9\_Spectrometer6.eps

**Figure 2.10**

Setup for the calibration of the scintillating screens.

- ▶ evaluation file See archived data for Buck et al. [56].
- ▶ figure file chapter2\Fig2-10\_Calibration\_Setup.eps

**Figure 2.11**

Emission spectrum, quantum efficiency, and modulation transfer function.

- ▶ evaluation file See archived data for Buck et al. [56].
- ▶ figure file chapter2\Fig2-11\_Spectra\_MTF.eps

**Figure 2.12**

Emission spectrum, quantum efficiency, and modulation transfer function.

- ▶ evaluation file See archived data for Buck et al. [56].
- ▶ figure file chapter2\Fig2-12\_Calibration\_Results.eps

**Figure 2.13**

Emission spectrum, quantum efficiency, and modulation transfer function.

- ▶ evaluation file See archived data for Buck et al. [56].
- ▶ figure file chapter2\Fig2-13\_Calibration\_Saturation.eps

**Figure 3.1**

High energy series of self-injected electrons with LWS-20.

- ▶ raw data folder chapter3\raw\_data\_3-1\_LWS20\_HighE\
- ▶ evaluation file chapter3\eval\  
ELAC\_FR0T\_spectrum\_eval\_3\_Diss\_high\_energy\_plot.m
- ▶ figure file chapter3\  
Fig3-1\_ELAC\_LWS20\_Self-Injection\_Series\_HighE2.eps

**Figure 3.2**

Stable series of self-injected electrons with LWS-20.

- ▶ raw data folder chapter3\raw\_data\_3-2\_LWS20\_SI\_LowE\
- ▶ evaluation file chapter3\eval\ELAC\_LWS20\  
\_spectrum\_eval\_4\_Diss\_stable\_self\_injection\_run.m
- ▶ figure file chapter3\  
Fig3-2\_ELAC\_LWS20\_Self-Injection\_Series\_Stable2.eps

**Figure 3.3**

Two stable electron series injected at the density transition with LWS-20.

- ▶ raw data folder `chapter3\raw_data_3-3_LWS20_SF_Two_Runs\`
- ▶ evaluation file `chapter3\eval\ELAC_CC_spectrum_eval_4c_Diss_low_energy.m`
- ▶ evaluation file `chapter3\eval\ELAC_Emitt_spectrum_eval_4b_Diss_high_energy.m`
- ▶ figure file `chapter3\Fig3-3_ELAC_LWS20_Shockfront_Two_Runs.eps`

**Figure 3.4**

Comparison of self-injection and density transition injection with LWS-20.

- ▶ raw data folder `chapter3\raw_data_3-4_LWS20_SF_Comparison\`
- ▶ evaluation file `chapter3\eval\ELAC_LWS20_spectrum_eval_4b_Diss_stable_self_injection_run_find_best_shots.m`
- ▶ figure file `chapter3\Fig3-4_Comparison2.eps`

**Figure 3.5**

Accelerating field and dephasing of the electron bunch.

- ▶ raw data folder `chapter3\raw_data_3-5_LWS20_SF_Dephasing\`
- ▶ evaluation file `chapter3\eval\ELAC_LWS20_spectrum_eval_4.m`
- ▶ plot file `chapter3\Fig3-5_Preparation2_Day 11-Scaling.opj`
- ▶ figure file `chapter3\Fig3-5_ELAC_LWS20_SF_Scaling_Position3.eps`

**Figure 3.6**

Observation of beamloading.

- ▶ raw data folder `chapter3\raw_data_3-6_LWS20_SF_Beamloading\`
- ▶ evaluation file `chapter3\eval\ELAC_FR0T2_spectrum_eval_5b_Diss_Beamloading_nicer.m`
- ▶ figure file `chapter3\Fig3-6_ELAC_LWS20_SF_Beamloading_3.eps`

**Figure 3.7**

Scaling of the electron energy with the electron density.

- ▶ raw data folder `chapter3\raw_data_3-7_LWS20_SF_Density\`
- ▶ evaluation file `chapter3\eval\ELAC_CC_spectrum_eval_4_DISS.m`
- ▶ evaluation file `chapter3\eval\ELAC_CC_spectrum_eval_4_addon_DISS.m`
- ▶ figure file `chapter3\Fig3-7_ELAC_LWS20_SF_Scaling_Density.eps`

**Figure 3.8**

Comparison of self-injection and density transition injection with ATLAS.

- ▶ raw data folder `chapter3\raw_data_3-8_ATLAS_SF_Comparison\`
- ▶ evaluation file `chapter3\ELAC_Shock_ATLAS_spectrum_eval_15_d_comparison_Diss2.m`
- ▶ figure file `chapter3\Fig3-8_ELAC_ATLAS_SF_Comparison2.eps`

**Figure 3.9**

Tunability of LWFA with ATLAS and density transition injection.

- ▶ raw data folder `chapter3\raw_data_3-9_ATLAS_SF_Tunability\`
- ▶ evaluation file `chapter3\eval\ELAC_Shock_ATLAS_spectrum_eval_15_c_produce_tuning_plot.m`
- ▶ figure file `chapter3\Fig3-9_ELAC_ATLAS_SF_Tuning2.eps`

**Figure 3.10**

Energy dependence of beam parameters and accelerating field.

- ▶ raw data folder `chapter3\raw_data_3-9_ATLAS_SF_Tunability\`
- ▶ plot file `chapter3\Fig3-10_Scaling_Divergence.opj`
- ▶ figure file `chapter3\Fig3-10_ELAC_ATLAS_Scaling_Divergence.eps`

**Figure 4.1**

Illustration of laser wakefield acceleration.

- ▶ figure file `chapter4\Fig4-1_Cover_Image.eps.eps`

**Figure 4.2**

Setup for Faraday rotation and shadowgraphy experiments.

- ▶ raw data folder `chapter4\raw_data_4-2_Spectra\`
- ▶ evaluation file `chapter4\eval\ELAC_FROT_spectrum_eval_3_Diss_sample_spectra.m`
- ▶ figure file `chapter4\Fig4-2_FROT_Setup2.eps`

**Figure 4.3**

Simulation of the polarimetry and shadowgraphy signal.

- ▶ raw data folder `chapter4\raw_data_4-3_Raytracing\`
- ▶ evaluation file `chapter4\eval\FROT_PIC_paper_single_shot5d_DISS_incl_pulse_dur.m`
- ▶ evaluation file `chapter4\eval\FROT_PIC_paper_single_shot3_with_spectrum.m`

- ▶ evaluation file `chapter4\eval\FROT`  
`_Plasma_Wave_Diffraction_2D_5_for_DISS_pulse_dur.m`
- ▶ plot file `chapter4\eval\modulation2.opj`
- ▶ figure file `chapter4\Fig4-3_PIC_Raytracing3.eps`

**Figure 4.4**

Raw images of the two cameras and evaluated polarization rotation angle.

- ▶ raw data folder `chapter4\raw_data_4-4_all_FR0T\`
- ▶ evaluation files `chapter4\eval\labview\`
- ▶ figure file `chapter4\Fig4-4_FR0T_Single_Shot.eps`

**Figure 4.5**

Scaled polarization rotation angle vs. charge.

- ▶ raw data folder `chapter4\raw_data_4-4_all_FR0T\`
- ▶ evaluation files `chapter4\eval\evolution\`
- ▶ plot file `chapter4\eval\Fig4-5_Rotation_Angle_Charge.opj`
- ▶ figure file `chapter4\Fig4-5_Rotation_Angle_Charge2.eps`

**Figure 4.6**

Plasma wave observation via shadowgraphy.

- ▶ raw data folder `chapter4\raw_data_4-6_Shadowgraphy\`
- ▶ evaluation file `chapter4\eval\`  
`FROT_plot_paper_single_shot_10b_for_thesis.m`
- ▶ evaluation file `chapter4\eval\FROT_plasma_wave_easycount_3.m`
- ▶ figure file `chapter4\Fig4-6_Shadowgraphy_Plasma_Wave.eps`

**Figure 4.7**

Shadowgram of the shockfront.

- ▶ raw data folder `chapter4\raw_data_4-7_Shadowgram_Shockfront\`
- ▶ evaluation file `chapter4\FROT2_plasma_wave_shockfront_1b.m`
- ▶ figure file `chapter4\Fig4-7_Shadowgraphy_Shockfront2.eps`

**Figure 4.8**

Snapshots of the trapped electrons and the plasma wave.

- ▶ raw data folder `chapter4\raw_data_4-4_all_FR0T\`
- ▶ evaluation file `chapter4\FROT_nice_image_1D_7.m`
- ▶ figure file `chapter4\Fig4-8_Delay_scan.eps`

**Figure 4.9**

Evolution of the electron bunch duration and the plasma wave during the acceleration.

- ▶ raw data folder chapter4\raw\_data\_4-4\_all\_FROT\
- ▶ evaluation files chapter4\eval\evolution\
- ▶ plot file chapter4\eval\Fig4-9.opj
- ▶ figure file chapter4\Fig4-9\_Combined2.eps

**Figure 6.1**

Overview of electron parameters of all stable ATLAS runs.

- ▶ raw data folder chapter6\raw\_data\_6-1\_ATLAS\_Comparison\
- ▶ plot file chapter6\eval\All Run comparison2.opj
- ▶ data file chapter6\Shockfront ATLAS - Run overview.docx
- ▶ figure file chapter6\Fig6-1\_ELAC\_ATLAS\_SF\_Comparison\_Old\_New3.eps

**Figure 6.2**

Evolution of the electron bunch during the acceleration process with controlled injection.

- ▶ raw data folder chapter6\raw\_data\_6-2\_FROT2\
- ▶ evaluation file chapter6\FROT2\_eval\_frot\_script\_8\_run483.m
- ▶ plot file chapter6\eval\FROT2 - FROT visibility.opj
- ▶ figure file chapter6\Fig6-2\_FROT2\_Combined.eps

**Figure A.1**

Cross-polarized wave generation setup.

- ▶ raw data folder appendix\raw\_data\_7\
- ▶ figure file appendix\Fig7-1\_XPW\_Setup2.eps

**Figure A.2**

Contrast enhancement of LWS-20 with XPW.

- ▶ raw data folder appendix\raw\_data\_7\
- ▶ plot file appendix\eval\XPW paper contrast.opj
- ▶ figure file appendix\Fig7-2\_XPW\_Contrast.eps

**Figure A.3**

Spectral broadening by cross-polarized wave generation.

- ▶ raw data folder appendix\raw\_data\_7\
- ▶ plot file appendix\eval\EVAL2.opj
- ▶ figure file appendix\Fig7-3\_XPW\_spectrum.eps



# Curriculum Vitae of Alexander Buck

## Personal

**Date of birth** 13 April, 1983, Stuttgart, Germany  
**Citizenship** German  
**Postal address** Max Planck Institute of Quantum Optics  
Hans-Kopfermann-Str. 1  
85748 Garching  
**Telephone** +49-89-32905-541  
**eMail** alexander-buck (at) web.de

## Education

**01/2008 - present** **Max Planck Institute of Quantum Optics, Garching, Germany**  
**Ludwigs-Maximilians-Universität, München, Germany**  
PhD candidate  
Dissertation topic: "Advanced characterization and control of laser wakefield acceleration"  
Supervisor: Prof. Dr. Ferenc Krausz

**08/2006 - 08/2007** **University of Texas at Austin, USA**  
Graduate student  
Master of Arts in Physics in 08/2007  
GPA: 3.95  
Thesis topic: "The granular temperature based on the fluctuation-dissipation theorem"  
Supervisor: Prof. Dr. Harry L. Swinney

**10/2003 - 07/2006** **Bayerische Julius-Maximilians-Universität, Würzburg, Germany**  
Student of physics  
Intermediate diploma (Vordiplom) in physics in 10/2005

Overall grade: 1.31  
 Studies in experimental and theoretical physics,  
 mathematics, and chemistry  
**until 06/2002** **Stiftsgymnasium, Sindelfingen, Germany**  
 Abitur (General qualification for university admission)  
 Overall grade: 1.3

## Honors and Scholarships

**10/2010** Finalist in the 2010 Emil Wolf Outstanding Student Paper  
 Competition at the Frontiers in Optics 2010, Rochester, NY, USA  
**06/2010** Poster prize at the 37<sup>th</sup> Conference on Plasma Physics of the  
 European Physical Societa in Dublin, Ireland  
**01/2008 - present** Scholar of the International Max-Planck Research School (IMPRS)  
**01/2008 - 05/2009** Full scholarship of the Max Planck Society  
**08/2006 - 05/2007** C. Paul Boner fellowship  
 Paul Boner Graduate Sholarship in Physics  
**06/2002 - present** Scholarship of the career network "e-fellows.net"  
**06/2002** Ferry-Porsche-Prize for outstanding high school grades  
 in Mathematics and Physics  
**06/2002** Award of the German Physical Society (DPG) for an  
 outstanding high school diploma in Physics

## Work experience

**09/2010 - present** **Ultrafast Innovations GmbH, Garching, Germany**  
 Part-time freelancer for the development and construction  
 of diagnostics for ultrashort, high-intensity laser pulses  
**10/2007 - 12/2007** **Fraunhofer Institute for Laser Technology, Aachen, Germany**  
 Graduate Research Assistant  
**08/2002 - 05/2003** **Arbeiterwohlfahrt (AWO), Konstanz, Germany**  
 Civilian service

## Qualifications

<b>Languages</b>	German (mother tongue), English (fluent), French (advanced), Spanish (basic knowledge)
<b>Programming</b>	Matlab, Mathematica, LabView
<b>Applications</b>	Microsoft Office, Adobe Illustrator, Autodesk Inventor, Origin, PovRay

## Honorary Posts

<b>04/2009 - present</b>	Secretary of the Student Chapter "Southern Germany" of the Optical Society of America
<b>11/2008 - 12/2009</b>	Leader of the secretary group of the PhDnet, the network of all PhD students within the Max Planck Society
<b>11/2008 - 11/2009</b>	PhD representative at the Max Planck Institute of Quantum Optics, Garching, Germany
<b>10/2005 - 08/2006</b>	Spokesperson of the America exchange programm 2006/07 of the department of physics at the University of Würzburg, Germany
<b>10/2004</b>	Mentoring for new students in the orientation week at the University of Würzburg, Germany
<b>08/2001 - 07/2002</b>	Athletics coach of 6-10 year old children at the TSV Dagersheim, Böblingen, Germany

## Professional memberships

Optical Society of America (OSA)  
German Physical Society (DPG)

## Spare time interests

<b>Music</b>	Piano, guitar
<b>Sports</b>	Tennis, running



# Acknowledgements

- First of all, I want to thank my doctoral adviser **Prof. Dr. Ferenc Krausz** for giving me the opportunity to work as a PhD student in such an outstanding environment. I also want to thank him for his great encouragement and support which he gave even though the group has grown strongly over the past years.
- Special thanks also go to **Dr. Laszlo Veisz**, my direct supervisor for his incredible effort he put into the supervision of this thesis. Despite all his other tasks, he still spend countless hours with us in the lab and was always there when new problems with the laser arose.
- I want to express my thanks to **Prof. Dr. Toshiki Tajima** for reviewing my thesis and his interest into my work. I am very honored to have one of the founders of this field on my comittee.
- I would like to thank **Dr. Karl Schmid** and **Dr. Christopher M. S. Sears**, who performed most of the experiments presented in this thesis with me. My doctoral work would have certainly not been possible without all their groundwork, their support, and all their great ideas in the lab and during the data evaluation.
- **Prof. Dr. Malte C. Kaluza** pointed our interest towards the optical probing of the magnetic fields in the LWFA process. I would like to thank him and his two PhD students **Maria Nicolai** and **Alexander Sävert** for all their effort they put into this very successful experimental campaign.
- **Johannes Wenz** and I also spend many long hours in the lab to perform the controlled injection experiments with ATLAS. I would like to thank him and also **Prof. Dr. Stefan Karsch**, **Matthias Heigoldt**, and **Konstantin Khrennikov** for their endless effort to keep the ATLAS laser in a good shape.
- I want to thank **Dr. Julia M. Mikhailova** and **Jiancai Xu** for all their support from

the theoretical side. They performed many simulations for us with the ILLUMINATION code by **Dr. Michael Geissler** to understand our experiments.

- Many thanks also go to **Daniel Herrmann, Raphael Tautz, and Dr. Franz Tavella**, for all their work on LWS-20 to generate the high-intensity, few-cycle pulses. I also want to thank them for their support for the cross-polarized wave generation stage.
- I would like to thank **Dr. Ulrich Schramm, Karl Zeil, Dr. Stefan Kraft, and Axel Jochmann** for the opportunity to perform the calibration experiments at the ELBE accelerator in Dresden and their support in the data evaluation and the preparation of the publication.
- **Manfred Fischer, Alois Böswald, Anton Horn, Harald Haas, and Hans-Peter Schönauer** have been a great help for many different parts of the experiments.
- Many thanks go to **Tom Strobl, Michael Rogg**, and their team at the **MPQ-Werkstatt** for dealing with all the urgent and special requests.
- I would especially like to thank my friend **Daniel Kiefer**, who followed me (or I followed him) through all our career steps from the very first day in Würzburg over CNLD at UT Austin to the Krausz-group at MPQ. Many thanks also to all the other **students at the MPQ and in the IMPRS** who made the years at MPQ such a wonderful time.
- Many thanks also to **Brigitte Rütlein** for carefully proofreading this thesis.
- I want to thank my fiancée **Anna Rütlein, my parents, and my sister** for all your love and your support. I could not have done this work without you.